VSEBINA – CONTENTS

A MATHEMATICAL MODEL FOR THE STATIONARY PROCESS OF ROLLING OF TUBES ON A CONTINUOUS MILL

MATEMATIČNI MODEL PROCESA KONTINUIRNEGA VALJANJA CEVI

Yu. G. Gulyayev[1], Ye. I. Shyfrin[2], Ilija Mamuzić[3]

[1]National Metallurgical Academie of Ukraine, Dnipropetrovsk, Ukraine
[2]Tube MetallurgicCompany, Russia
[3]University of Zagreb, Faculty of Metallurgy Sisak, Croatia
mamuzic@simet.hr

A mathematical model has been developed for the calculation of process parameters in continuous lengthwise plugless tube rolling. Examples of concrete calculations of rolling parameters, their comparison with experimental data and the results obtained with the application of other calculation procedures are given.

Key words: tubes, plugless rolling, mathematical model

Razvit je bil matematični model za izračun parametrov procesa neprekinjenega valjanja cevi brez notranjega trna. Dani so konkretni primeri izračunov parametrov valjanja, rezultati pa so primerjani z eksperimentalnimi podatki in z izračuni po drugih postopkih.

Ključne besede: cevi, valjanje brez trna, matematični model

1 INTRODUCTION

The prospects of enhancement of the production efficiency at numerous tube rolling units are closely linked with the possibility of a reliable prediction of the forming parameters at the final stage of plastic deformation in the plugless tube reducing or sizing processes. In this connection, the problem of development of a universal mathematical model applicable in studying the process of lengthwise plugless rolling in the tube rolling mills equipped with the roll drives of different types is of a high interest.

2 STATE OF THE ISSUE AND THE AIM OF INVESTIGATION

The analysis of the relevant references shows that the problem of determination of kinematical, deformational and power-and-force parameters of the continuous plugless lengthwise tube rolling process was solved up to now by *consecutive* analysis of forming in each individual stand. Solutions based on integration of the deformational parameters in all N stands of the continuous mill into a common system of equations are proposed, also [1,2]. In the development of mathematical models of the continuous rolling process, e.g. in [1,2] two assumptions were made.

Firstly, the mean angle of the neutral section θ_{ni} (**Figure 1**) is defined for the condition of coincidence of the roll and the mother tube speeds within the section of the deformation zone *exit* in the i-th stand, though it would be logical to choose some section between the entry and exit of the deformation zone.

Secondly, for the determination of the effective roll diameter D_{ki}, the approximate formula is used: $D_{ki} = D_{ui} - D_i \cos\theta_{ni}$ (where D_{ui}, D_i – are the ideal roll diameter and the mean tube diameter after rolling in the i-th stand respectively) that introduces an error because in reality $D_{ki} = D_{ui} - 2r_{\theta i}(\theta_{ni}) \cos\theta_{ni}$ (where D_{ui} is the ideal roll diameter; $r_{\theta i}(\theta_{ni})$ is the pass radius at $\theta = \theta_{ni}$, see **Figure 2**).
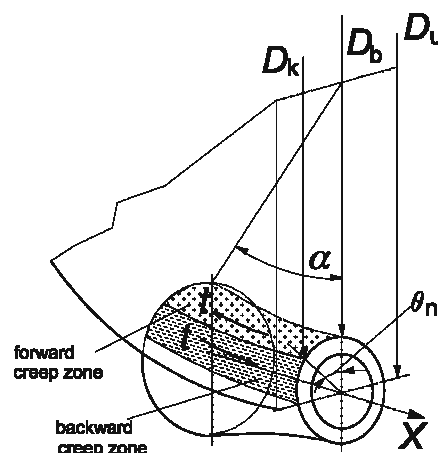
Figure 1: Scheme for the determination of the value of the effective diameter D_k
Slika 1: Shema za določitev efektivnega premera D_k

In accord with the model consisting of $2N$ equations proposed[1], the effective roll diameter D_{ki} cannot be greater than the ideal roll diameter D_{ui} and smaller than the roll diameter at the swell D_{bi}. This distorts the real picture of the rolling process kinematics, namely, when the rolls slip on the mother tube surface two conditions are met: $D_{ki} < D_{bi}$ or $D_{ki} > D_{ui}$. The model proposed [2] is free from this shortcoming but it is a system of $3N$ equations that when being solved at $N > 16$ is connected with considerable difficulties because of the great number of unknowns to be determined.

This work is aimed at the verification and simplification of the mathematical models proposed [1,2] and to the assessment of the verification results on the basis of comparison of calculated and experimental data and it is, for this reason, of scientific and practical interest.

3 PROBLEM STATEMENT

The following values have to be calculated:
– angular roll rotation velocity n_{Bi} in each i-th mill stand (for the mill with individual roll drives);
– angular velocities of rotation of the main (N_Γ) and auxiliary (N_B) motors (for the mill with differential-group roll drives);
– ideal roll diameters D_{ui} (for the mill with group roll drives).

These values ensure that tubes of required size ($D_t \cdot S_t$, mm) are rolled from the mother tube of given size (($D_0 \times S_0$) mm) at a specified rolling speed V_0/(m/s) in the first stand of the multiple-stand mill.

Initial data for the calculation are as follows:
– the total diameter and wall reduction (or just diameter reduction), i.e. initial mother tube dimensions $D_0 \times S_0$ (or just D_0) and final tube dimensions $D_t \times S_t$;
– the distribution of partial mother tube diameter reductions m_i (%) among the mill stands of total number of N;
– the value of external friction f_i;
– the mother tube rolling speed V_0/(m/s) in the first mill stand (the problem can also be stated for V_0 as the value to be determined);
– the gear ratios $\eta_{\Gamma i}$, η_{Bi} from the motors to the rolls in the lines of the main and auxiliary drives (for the mills with differential-group roll drives);
– the absence of backward pull in the first mill stand ($Z_{31} = 0$) and of front pull in the last mill stand ($Z_{nN} = 0$);
– the number of rolls N_b forming passes in the mill stands.

4 PHYSICAL MODEL OF THE PROCESS

No mother tube forming occurs in interstand spaces and the wall thickness S_j at the exit from the stand of ordinal number $j = i - 1$ is equal to the wall thickness S_{0i}

at the entry to the stand of ordinal number i. The deformation resistance K_{fj} of the mother tube material at the exit from the stand of ordinal number j is equal to the deformation resistance K_{f0i} of the mother tube material at the entry to the stand of ordinal number i. It follows that the coefficient of front plastic pull Z_{nj} for the stand of ordinal number j is equal to coefficient of backward plastic push Z_{3i} for the stand of ordinal number i. The area F_{ki} of the contact surface of the mother tube with one roll in the stand of ordinal number i is equal to the area of a rectangle with sides

$$L_i = \sqrt{\frac{\beta_i \cdot D_j \cdot \varepsilon_i \cdot (D_{ui} - D_i)}{2 \sin \beta_i}} \quad (1)$$

with

$$B_i = \beta_i \cdot D_j \quad (2)$$

where D_j and D_i are the mean mother tube diameters at the entry to and at the exit from the deformation zone in the stand of ordinal number i;

$$\varepsilon_i / \% = \frac{m_i}{100}; \quad \beta_i = \frac{\pi}{N_{bi}}$$

The area F_i^+ of the zone of forward creep at the surface of contact between one roll and the mother tube in the deformation zone of the stand of ordinal number i is defined as the surface of a rectangle with sides

$$L_i^+ = L_i \quad (3)$$

and

$$L_i^+ = \theta_{ni} D_j \quad (4)$$

where θ_{ni} is the neutral section angle characterizing the position of the neutral line differentiating the zone of forward creep and the zone of backward creep on the surface of contact between the mother tube and the roll in the deformation zone (**Figure 1**).

In a real process, the magnitude of angle θ_{ni} is a function of the angle α characterizing the position of a concrete diametrical section of the deformation zone relative to the diametrical section of the mother tube exit from the reduction zone. In accord with the assumption[4], the magnitude of angle θ_{ni} is assumed to be equal to some quantity averaged over the contact surface length. It will be regarded that θ_{ni} is the value of the neutral angle in the "neutral" diametrical section of the deformation zone where the extension is equal to the mean extension in the i-th stand. The axial velocity V_{Mn} of metal and axial component of the roll surface velocity V_{Bn} in the "neutral" diametrical section are given with

$$V_{Mni} = V_0 \, \mu_{\Sigma i}^{cp} \quad (5)$$

$$V_{Bni} = \frac{\pi n_{Bi} A_{ti}^{cp} D_{\theta i}}{\xi} \quad (6)$$

where $\mu_{\Sigma i}^{cp} = \frac{2 S_0 (D_0 - S_0)}{S_j (D_j - S_j) + S_i (D_i - S_i)}$ is the total elongation from the mill entry to the "neutral" diametrical section of the i-th stand;
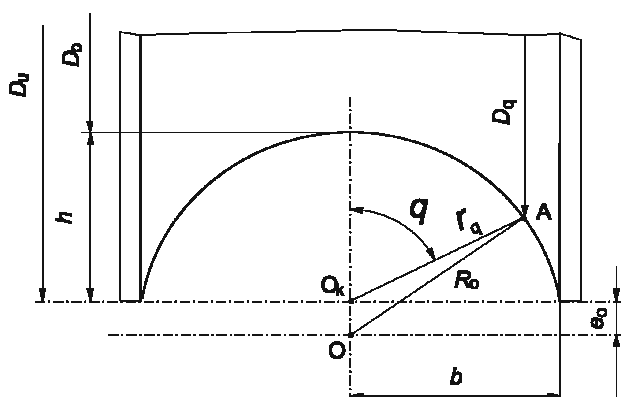
Figure 2: Scheme for the determination of the value of the variable across the pass perimeter of the roll diameter D_θ
Slika 2: Shema za določitev spremembe premera valjev D_θ na obodu vtika

A_{ti}^{cp} is the mean value of the guiding cosine of the contact friction stresses [1];

$D_{\theta i} = D_{ui} - 2r_{\theta i} \cos\theta$ is the varying of the roll pass diameter across the pass perimeter (**Figure 2**);

$$r_{\theta i} = \overline{O_k}\,\overline{A} = R_{oi}\left[\sqrt{1-\left(\frac{e_{oi}}{R_{oi}}\right)^2\left(1-\cos^2\theta\right)} - \frac{e_{oi}\cos\theta}{r_{oi}}\right] \text{ is}$$

the varying across the pass perimeter value of the pass diameter;

$$R_{oi} = \overline{OA} = \frac{h_i(\lambda_{oi}^2 + 1 - 2\lambda_{ki}\sin\psi)}{2(1-\lambda_{ki}\sin\psi)} \text{ is the pass generatrix}$$

radius;

$$e_{oi} = \overline{O_k}\,\overline{A} = \frac{h_i(\lambda_{oi}^2 - 1)}{2(1-\lambda_{ki}\sin\psi)} \text{ is the pass generatrix eccen-}$$

tricity;

$\lambda_{ki} = \dfrac{b_i}{h_i}$ is the pass ovality;

$\psi = \dfrac{(N_b - 2)}{2N_b}$ is the pass shape index;

b_i, h_i are the pass width and the pass height correspondingly;

$\xi = 6\cdot10^4$ is coefficient of quantity dimension reduction $(s\cdot mm\cdot\dfrac{r}{min}\cdot m)$

The angle θ_{ni} is defined as root of the transcendental equation

$$V_{Mni} - V_{Bni} = 0 \qquad (7)$$

Taking in account that in a physical sense $0 \le \theta_{ni} \le \beta_i$, the condition for the determination of the neutral angle assumes the following form (in symbols of Math-CAD programming language)

$$\theta_{ni} = \begin{vmatrix} \arccos Q_i \text{ if } \cos\beta_i \le Q_i \le 1 \\ 0 \text{ if } 1 < Q_i \\ \beta_i \text{ if } \cos\beta_i > Q_i \end{vmatrix} \qquad (8)$$

The quantity Q_i in (8) is defined as the root of equation

$$\frac{2S_0V_0(D_0-S_0)}{S_j(D_j-S_j)+S_i(D_i-S_i)} - \frac{\pi n_{Bi}A_{ti}^{cp}}{\xi} \cdot$$

$$\cdot\left\{D_{ui} - 2Q_iR_{oi}\left[\sqrt{1-\left(\frac{e_{oi}}{R_{oi}}\right)^2\left(1-Q_i^2\right)} - \frac{e_{oi}Q_i}{R_{oi}}\right]\right\} = 0 \qquad (9)$$

Note that as distinct from the conditions used[1,2], the condition (8) reflects the relation of the neutral angle θ_{ni} value with the roll design parameters (R_{0i}, e_{0i}, λ_{ki}, b_i, h_i).

Taking into consideration relationships (5) and (6), the effective roll diameter D_{ki} can be defined by the following equation:

$$D_{ki} = \frac{2S_0V_0(D_0-S_0)\xi}{\pi\left[S_j(D_j-S_j)+S_i(D_i-S_i)\right]n_{Bi}A_{ti}^{cp}} \qquad (10)$$

For $D_{bi} < D_{ki} < D_{ui}$, on the contact surface of each roll appears a forward creep zone with the area equal of $F_i^+ = \theta_{ni}D_jL_i$ in accord with (3), (4) and the backward creep zone with the area equal to $F_i^- = (\beta_i - \theta_{ni})D_jL_i$. For $D_{bi} > D_{ki}$, the backward creep zone extends over the entire contact surface area and the "forward roll slippage" takes place on the metal surface. If $D_{ui} < D_{ki}$, the forward creep zone extends over the entire contact surface area and "backward roll slippage" takes place on the metal surface.

The magnitude of neutral angle θ_{ni} must meet the condition of force equilibrium of the metal volume in the geometrical deformation zone of the i-th stand [1] that can be expressed as:

$$\theta_{ni} = \beta_i \cdot \begin{vmatrix} X_i \text{ if } 0 \le X_i \le 1 \\ 0 \text{ if } 0 > X_i \\ 1 \text{ if } 1 < X_i \end{vmatrix} \qquad (11)$$

where

$$X_i = \frac{F_i^+}{F_{ki}} = \frac{1}{2}\cdot\left\{1 - \frac{A_{pi}^{cp}}{f_iA_{ti}^{cp}} + \frac{Z_{ni}S_i(D_i-S_i)-Z_{nj}S_j(D_j-S_j)}{f_iA_{ti}^{cp}\left(2L_i+\sqrt{S_jD_j}\right)n_{ti}S_i\frac{D_j}{D_i}\left[1-(Z_{cp})\right]}\right\}$$

is the coefficient of forward creep in the i-th mill stand calculated for the equilibrium of forces in the volume of the metal in the geometrical deformation zone of the i-th stand;

A_{ti}^{cp} is the mean, over the contact surface, value of the guiding cosine for normal contact stresses;

f_i is coefficient of external friction;

$n_{ti} = 1 + 0{,}36 f_i$ is coefficient accounting for the effect of the contact friction stresses upon normal contact stresses[3];

Z_π is coefficient of forward plastic pull;

$(Z_{cp})_i = \dfrac{Z_{ni}}{3} + \dfrac{2Z_{nj}}{3}$ is the mean value of the plastic pull coefficient in the i-th stand.

Table 1: Parameters of rolling a (57 × 11.6) mm tube from a (117 × 14.8) mm mother tube
Tabela 1: Parametri valjanja cevi (57 × 11.6) mm iz cevi (117 × 14.8) mm

i	D_i/mm	m_i/%	λ_{ki}	S_i/mm			Z_{ni}		θ_{ni}/°		P_i/kN		M_i/(kN·m)	
				E	A	B	A	B	A	B	A	B	A	B
1	115.25	1.50	1.037	14.77	14.86	14.85	0.327	0.361	53.7	56.8	93	92	-14.5	-16.6
2	112.59	2.30	1.024	14.82	14.82	14.81	0.568	0.606	51.3	53.2	74	69	-10.0	-10.6
3	109.67	2.60	1.032	15.55	14.68	14.64	0.721	0.756	46.9	48.2	49	44	-5.3	-5.2
4	106.49	2.90	1.028	14.35	14.47	14.40	0.729	0.766	19.9	19.1	37	32	3.0	2.7
5	102.97	3.30	1.038	14.07	14.22	14.13	0.730	0.761	17.7	14.0	38	32	3.8	3.9
6	99.47	3.40	1.034	13.75	13.97	13.86	0.729	0.755	17.00	14.4	37	33	3.8	3.9
7	96.09	3.40	1.036	13.50	13.73	13.60	0.724	0.742	16.6	13.5	37	33	3.8	4.2
8	92.82	3.40	1.035	13.28	13.49	13.35	0.715	0.743	16.3	17.2	37	33	3.9	3.4
9	89.57	3.50	1.037	13.00	13.26	13.10	0.705	0.721	16.7	14.1	37	34	4.0	4.2
10	86.44	3.50	1.036	12.70	13.03	12.87	0.693	0.711	17.2	15.4	38	35	3.9	4.0
11	83.41	3.50	1.037	12.49	12.82	12.65	0.679	0.693	17.5	16.1	38	36	3.9	4.0
12	80.49	3.50	1.036	12.41	12.62	12.44	0.665	0.676	18.2	17.3	39	37	3.8	3.9
13	77.68	3.50	1.036	12.31	12.42	12.25	0.650	0.659	18.8	18.2	40	38	3.7	3.7
14	74.96	3.50	1.036	12.18	12.24	12.06	0.635	0.642	19.4	18.9	41	39	3.7	3.7
15	72.33	3.50	1.036	11.95	12.07	11.89	0.618	0.623	19.9	19.4	42	41	3.6	3.6
16	69.80	3.50	1.036	11.78	11.91	11.74	0.595	0.597	19.7	19.2	43	42	3.8	3.8
17	67.36	3.50	1.036	11.69	11.77	11.59	0.568	0.564	20.1	19.6	45	44	3.8	3.9
18	65.00	3.50	1.036	11.58	11.64	11.47	0.532	0.518	20.1	19.2	47	47	4.0	4.4
19	62.73	3.50	1.036	11.53	11.53	11.39	0.459	0.414	18.2	16.1	52	54	5.3	6.3
20	60.53	3.50	1.036	11.40	11.49	11.41	0.267	0.078	12.6	6.5	63	72	9.2	13.8
21	59.02	2.50	1.020	11.50	11.53	11.44	0.036	-0.140	14.3	17.4	71	87	9.4	9.3
22	57.96	1.80	1.018	11.58	11.58	11.58	0.001	-0.105	25.7	29.0	74	85	3.0	1.3
23	57.60	0.61	1.000	11.60	16.00	11.60	0	0	28.4	34.3	51	54	1.0	-1.6

NOTES:

A = calculation by the procedure proposed in [1]
B = calculation by the procedure proposed in this work
E = experimental data

5 MATHEMATICAL MODEL

Equate right parts of equations (8) and (11) and use the equation of relation between the change of the mean wall thickness and force conditions of the mother tube deformation in each i-th mill stand [4,5] to obtain the mathematical model of the continuous mother tube rolling process in N stands of the mill as a system of $2N$ equations:

$$\theta_{ni} = \begin{vmatrix} \arccos Q_i & \text{if } \cos\beta_i \leq Q_i \leq 1 \\ 0 & \text{if } 1 < Q_i \\ \beta_i & \text{if } \cos\beta_i > Q_i \end{vmatrix} =$$

$$= \beta_i \cdot \begin{vmatrix} X_i & \text{if } 0 \leq X_i \leq 1 \\ 0 & \text{if } 0 > X_i \\ 1 & \text{if } 1 < X_i \end{vmatrix} \qquad (12)$$

$$S_i - S_j \left\{ 1 + \varphi_i \cdot \frac{2(Z_{cp})_i (T_i - 1) + (1 - 2T_i)}{(Z_{cp})_i (1 - T_i) - (2 - T_i)} * \right.$$
$$\left. + \frac{1}{2} \left[\varphi_i \cdot \frac{2(Z_{cp})_i (T_i - 1) + (1 - 2T_i)}{(Z_{cp})_i (1 - T_i) - (2 - T_i)} \right]^2 \right\} \qquad (13)$$

where

$$\varphi_i = \ln \frac{D_i - S_i}{D_j - S_j}; \quad T_i = \left(\frac{S_j}{D_j} + \frac{S_i}{D_i} \right)^K;$$

$$(Z_{cp})_i = \frac{1}{2}(Z_{nj} + Z_{ni});$$

$K = 1.57$ for $N_b = 2$; $K = 1.20$ for $N_b = 3$; $i = 1, 2, \ldots , N–1, N$

Distinct from the known solution[2], the mathematical model includes $2N$ and not $3N$ equations that simplifies the search of solution and makes it possible to analyze the rolling process in stretch-reducing mills with $N \leq 25$ stands.

Depending on the type of the mill drive, the problem of determination of the rolling parameters with the use of the system of equations (12)-(13) can be formulated in different ways. For the mills with *individual* drives, it is necessary to determine $2N$ values of n_{Bi} (where $i = 1, 2, \ldots , N$) and S_i (where $i = 0, 1, 2, \ldots , N–1$) for the specified values of S_t, V_0 and Z_{ni} (where $i = 1, 2, \ldots , N–1$). For the mills with *differential-group* drives, it is necessary to find $2(N–1)$ values of the quantities S_i and Z_{ni} (where $i = 1, 2, \ldots , N–1$) and the values of N_Γ and N_B for the specified values of S_0, S_t, V_0. For the mills with *individual* drives, it is necessary to determine $N–1$ value

of the quantities D_{ui} (where $i = 2, 3, \ldots , N$), N values of the quantities S_i ($i = 0, 1, 2, \ldots , N$–1) and the angular roll velocity n_B that is constant for all stands at the specified values of D_{u1}, V_0 and Z_{ni} (where $i = 1, 2, \ldots , N$–1).

Solve the system of equations (12)-(13) using (8) or (11) to find values of neutral angles q_{ni} and determine the values of the effective diameters in correspondence with expression (10).

6 RESULTS OF MODEL CALCULATIOINS

The model has been successfully used in the calculation of tube rolling parameters for mills with the roll drives of individual, group and differential-group types.

As an example, let us consider the results of the calculation of the nature of change in the mean wall thickness S_i, rolling pressure P_i, rolling moments acting in the stand M_i and the values of Z_{ni}, q_{ni} in rolling a $D_t \cdot S_t$ = (57 × 11.6) mm tube from a $D_0 \cdot S_0$ = (117 x 14.8) mm mother tube in 23 stands of the tube rolling unit "30-102" reducing mill with differential-group roll drives ($N_B = 3$, $V_0 = 0.7$ m/s with the mother tube material: Grade 45 steel). In this case, the mathematical model (12)-(13) is a system of 46 equations with 46 unknowns: 22 values of S_i and Z_{ni} each and the values of N_G as well as N_B. The rolling parameters, results of calculation by the procedure given[1], by the proposed model and experimental data are given in **Table 1**. For the calculation of P_i and M_i values, the procedure[3] was used.

The processing of data in **Table 1** shows that when the procedure[1] was used, the standard deviation

$$\Delta = \sqrt{\frac{\sum_{i=1}^{N-1}(S_i^C - S_i^A)^2}{N-1}}$$

of calculated values of the wall thickness S_i^C from the actual values of this parameter S_i^A was D = 0.150 mm. When the present mathematical model was used, the value of D was of 0.085 mm and for 1.76 times smaller. Hence, the rolling parameter calculation accuracy is improved when the proposed procedure is used.

7 CONCLUSION

The mathematical model of the lengthwise continuous plugless tube rolling process has been developed and successfully tested. It improves the accuracy of calculation of the process parameters in comparison with the earlier developed procedure.

ACKNOWLEDGEMENT

8 REFERENCES

[1] Gulyayev Yu. G., Shyfrin Ye. I., Kvitka N. Yu. The mathematical model of the continuous plugless lengthwise tube rolling process in the tube rolling mills with individual roll drives. Teoriya i Practika Metallurgii (**2006**) 3, 66–74

[2] Gulyayev Yu. G., Shyfrin Ye. I., Kvitka N. Yu. The mathematical model of the continuous plugless lengthwise tube rolling. Teoriya i Praktika Metallugrii (**2006**) 6, 63–70

[3] The procedure of determination of a maximum roll pressure in the continuous plugless tube rolling process / G. I. Gulyayev, Yu. G. Gulyayev, Ye. I. Shyfrin, N. Yu. Kvitka, C. V. Darragh. – Material International Conference on New Developments in Long and Forged Products. – Winter Park (Colorado, USA), (2006), 127–132

[4] The technology of continuous plugless tube rolling: Edited by G. I. Gulyayev / G. I. Gulyayev, P. N. Ivshin, I. N. Yerokhin et al. – Moscow, Metallurgiya Publishers, 1975 – 264

[5] Shevchenko A. A., Yurgelenas V. A. Continuous plugless tube rolling under conditions of limiting values of the pull force. Trudy UkrNTO ChM. Dnepropetrovsk: UkrNTO ChM, 13 (**1958**), 77–86

THE TEMPERATURE DEPENDENCE OF THE PARAMETERS OF NON-LINEAR STRESS-STRAIN RELATIONS FOR CARBON-EPOXY COMPOSITES

TEMPERATURNA ODVISNOST PARAMETROV NELINEARNE ODVISNOSTI NAPETOST-DEFORMACIJA ZA KOMPOZITE OGLJIKOVO VLAKNO-EPOKSI

Tomáš Kroupa, Robert Zemčík, Jan Klepáček

University of West Bohemia in Pilsen, Department of Mechanics, Univerzitní 22, 306 14, Plzeň, Czech Republic
kroupa@kme.zcu.cz

This work focuses on the identification of the parameters of stress-strain relations for a unidirectional, continuous-fiber carbon-epoxy composite under tensile loading at various temperatures. Simple tensile tests of thin strips with various fiber orientations were performed. The identification of the parameters for the chosen non-linear stress-strain relations is obtained at each temperature for which the experiment is performed and the strength is determined. The failure analysis for the determination of the first failure with the use of Puck's action-plane concept is performed, and the tensile and shear strength are investigated. The identification process with the use of a combination of the mathematical optimization method and a finite-element analysis is described with the necessary details. The temperature dependence of the parameters is also investigated.

Key words: composite, non-linear, carbon, epoxy, tensile, FEA, temperature

Cilj dela je bil identifikacija parametrov odvisnosti napetost-deformacija za enosmerne neprekinjene kompozite ogljikovo vlakno-epoksi pri natezni obremenitvi in pri različni temperaturi. Izvršeni so bili natezni preizkusi tankih trakov z različno orientacijo vlaken.
Za vsako temperaturo, pri kateri je bil preizkus izvršen, so bili identificirani parametri nelinearne odvisnosti napetost-deformacija, določene pa so bile tudi trdnosti. Analiza preloma s ciljem, da se določi začetek preloma, je bila izvršena z uporabo Puckovega koncepta o ploskvi delovanja in raziskani sta bili natezna in strižna trdnost. Opisan je proces matematične identifikacije in analize po metodi končnih elementov s potrebnimi detajli. Raziskana je bila tudi temperaturna odvisnost parametrov.

Ključne besede: kompozit, nelinearnost, ogljik, epoksi, natezen, FEA, temperatura

1 INTRODUCTION

The aim was to investigate the temperature dependence of the parameters of non-linear stress-strain relations for a unidirectional carbon-epoxy composite with the use of a finite-element (FE) analysis. The elasticity parameters and strengths were found from the comparison of the FE analysis and experimental results for simple tension tests of thin carbon-epoxy strips with dimensions 150 mm × 14.5 mm × 1.08 mm. Specimens with three fiber directions were used. The fiber directions formed angles of 0°, 45° and 90° with the direction of the loading force. The tensile tests were performed at 25 °C, 50 °C, 75 °C and 100 °C.

Two types of non-linear stress-strain relations are presented. Their capabilities for prediction of the behavior of the composite material loaded with simple tension at various temperatures were investigated. The strengths of the material were investigated with the use of Puck's failure criterion [5].

2 NON-LINEAR STRESS-STRAIN RELATIONS

Several types of stress-strain relations exist. A linear stress-strain relation is the simplest way to describe the behavior of a composite material [2]. Unfortunately, it cannot describe the non-linear slope of the curves obtained from the tensile tests.

The next type is the non-linear stress-strain relation proposed in [1], which takes into account a non-linear relationship between the shear stress and the strain only, and is generalized in [3]. This relation can be written in a material axes coordination system L (longitudinal – fiber direction), T (transverse direction) for the state of plane stress in the form

$$
\begin{bmatrix} \varepsilon_L \\ \varepsilon_T \\ \gamma_{LT} \end{bmatrix} = \begin{bmatrix} S_{11} & S_{12} & 0 \\ S_{21} & S_{22} & 0 \\ 0 & 0 & S_{66} \end{bmatrix} \begin{bmatrix} \sigma_L \\ \sigma_T \\ \tau_{LT} \end{bmatrix} + \begin{bmatrix} S_{111}\sigma_L & 0 & 0 \\ 0 & S_{222}\sigma_T & 0 \\ 0 & 0 & S_{66666}\sigma_{LT}^2 \end{bmatrix} \begin{bmatrix} \sigma_L \\ \sigma_T \\ \tau_{LT} \end{bmatrix} \quad (1)
$$

where

$$
S_{11} = \frac{1}{E_L} \quad (2)
$$

$$
S_{22} = \frac{1}{E_T} \quad (3)
$$

$$
S_{12} = -\frac{\nu_{LT}}{E_L} \quad (4)
$$

$$S_{21} = -\frac{\nu_{TL}}{E_T} \qquad (5)$$

$$S_{66} = \frac{1}{G_{LT}} \qquad (6)$$

and

$$\nu_{TL} = \nu_{LT}\frac{E_T}{E_L} \qquad (7)$$

The strains are expressed as polynomial functions of the stresses and the relation contains [7] independent parameters that can be sorted as linear parameters (Young's moduli) E_L, E_T, G_{LT}, Poisson's ratio ν_{LT} and the non-linear parameters S_{111}, S_{222} and S_{6666}. The orders of the polynomials are predetermined and suitable for the tests performed at normal temperatures. The whole relation (R1) has to be inverted for proper use in the FE software. The Newton iteration method is used in the work to find the roots of the equation

$$\mathbf{f}(\sigma_L, \sigma_T, \tau_{LT}) = \mathbf{S}\boldsymbol{\sigma} - \boldsymbol{\varepsilon} = \mathbf{0} \qquad (8)$$

where $\mathbf{S}$ is the stress-strain matrix, $\boldsymbol{\sigma}$ is the stress vector and $\boldsymbol{\varepsilon}$ is the strain vector.

The stress-strain relation, which takes into consideration the non-linear behavior of the composite material and where the stresses are explicit functions of strains, can be expressed in the form

$$\begin{bmatrix} \sigma_L \\ \sigma_T \\ \tau_{LT} \end{bmatrix} = \begin{bmatrix} \frac{E_L}{1-\nu_{LT}\nu_{TL}} & \frac{\nu_{LT}E_L}{1-\nu_{LT}\nu_{TL}} & 0 \\ \frac{\nu_{LT}E_L}{1-\nu_{LT}\nu_{TL}} & \frac{E_T}{1-\nu_{LT}\nu_{TL}} & 0 \\ 0 & 0 & G_{LT} \end{bmatrix}\begin{bmatrix} \varepsilon_L \\ \varepsilon_T \\ \gamma_{LT} \end{bmatrix} \qquad (9)$$

where Ramberg-Osgood-based equations provide expressions for the tangent lamina stiffnesses

$$E_L = \frac{E_L^0}{\left[1 - \left(\frac{\varepsilon_L}{\varepsilon_L^0}\right)^{n_L}\right]^{1+\frac{1}{n_L}}} \qquad (10)$$

$$E_T = \frac{E_T^0}{\left[1 + \left(\frac{E_T^0 \varepsilon_T}{\sigma_T^0}\right)^{n_T}\right]^{1+\frac{1}{n_T}}} \qquad (11)$$

$$G_{LT} = \frac{G_{LT}^0}{\left[1 - \left(\frac{G_{LT}^0 \gamma_{LT}}{\tau_{LT}^0}\right)^{n_{LT}}\right]^{1+\frac{1}{n_{LT}}}} \qquad (12)$$

and the relation between the Poisson's ratios is considered as

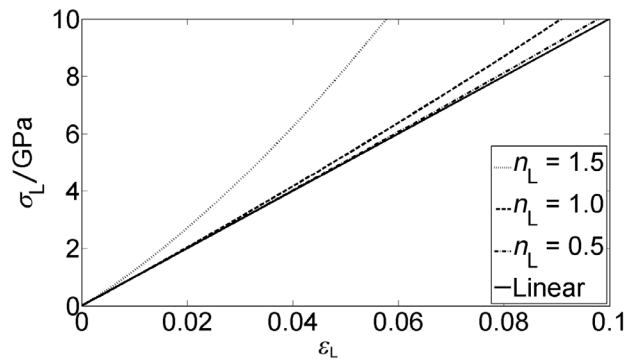$$\nu_{TL} = \nu_{LT}\frac{E_T^0}{E_L^0} \qquad (13)$$

Figure 1: The influence of the shape parameter n_L
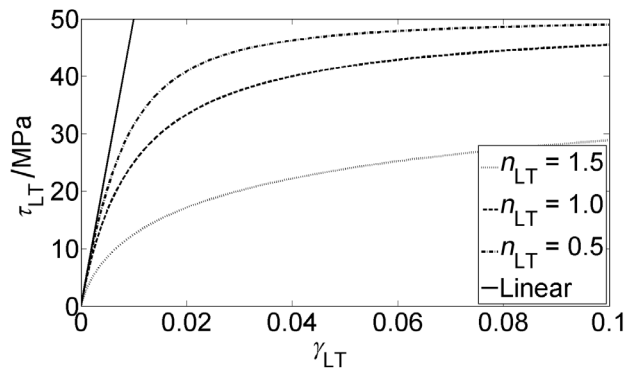**Slika 1:** Vpliv parametrov oblike n_L

Figure 2: The influence of the shape parameter n_{LT}
Slika 2: Vpliv parametrov oblike n_{LT}

The relation (9) includes 10 independent parameters. These parameters are the initial moduli E_L^0, E_T^0, G_{LT}^0, the asymptotic stress and strain levels σ_T^0, τ_{LT}^0 and ε_L^0, the shape parameters n_L, n_T, n_{LT} and the Poisson's ratio ν_{LT}. **Figure 1** shows the influence of the shape parameter n_L for a material with $E_L^0 = 100$ GPa and $\varepsilon_L^0 = 1$.

Figure 2 shows the influence of the shape parameter n_{LT} for the material with $G_{LT}^0 = 5$ GPa and $\tau_{LT}^0 = 50$ MPa.

3 IDENTIFICATION OF THE ELASTICITY PARAMETERS

The identification of the elasticity parameters is the first step in the identification process. The method used for the identification of the elasticity parameters, which combines the material axis and the off-axis tensile tests, the FE analysis and the mathematical optimization method will be described in the following paragraph.

Non-linear stress-strain relations have to be implemented into the FE software first. The number of elements in the FE models for the calculation of the force-displacement diagrams has to be reduced as much as possible. The reduction of the number of elements is necessary for the reduction of the time consumption during the optimization cycles. The next step is to propose the residual function that represents the difference between the numerical and the experimental

70

results at the given optimization step, and which is minimized. The function is proposed as

$$r = \sum_{\theta} \frac{\sum_{p} \left[F_{\exp}(\theta, p) - F_{\mathrm{num}}(\theta, p) \right]^2}{\max_{p} \left[F_{\exp}(\theta, p) \right]} \quad (14)$$

where θ is the fiber angle, $r(\theta)$ is the residual of the force-displacement diagram for the fiber angle θ, which had values 0°, 15°, 30°, 45°, 60°, 75° and 90°; p is the displacement where the residual is calculated; $F_{\mathrm{num}}(\theta, p)$ is the calculated force corresponding to the displacement p of the strip with the fiber angle θ; $F_{\exp}(\theta, p)$ is the experimentally measured force corresponding to the displacement p of the strip with the fiber angle θ and $\max_{p} \left[F_{\exp}(\theta, p) \right]$ is the maximum force measured as a response of the strip with a fiber angle θ, used as a normalization coefficient.

It should be noted that the Poisson's ratio ν_{LT} has to be identified with a special, separate test and, therefore, it will not be investigated in this paper, and its value is taken as $\nu_{\mathrm{LT}} = 0.28$. The tests, probably a biaxial test able to precisely describe the potential strain dependence of the Poisson's ν_{LT} ratio, and a further analysis of the influence of the temperature on the Poisson's ratio ν_{LT} will be performed in the near future.

The flow chart of the whole automated process of the identification of the elasticity parameters is shown in **Figure 3**.

4 IDENTIFICATION OF THE STRENGTHS

Once the elasticity parameters are identified, the identification of the strengths can be performed. The failure criterion used in the strengths identification process is Puck's action-plane concept. For more about
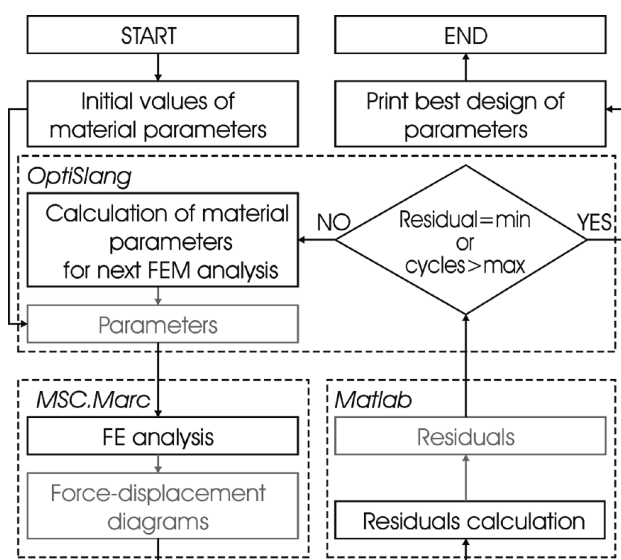
the criterion, see [4-6]. Once the tensile test is performed, only the tensile X^{T}, Y^{T} and the shear S^{L} strengths can be identified. The identification of the strengths is performed with the use of a minimized function, which is proposed as the sum of the errors between the average of the measured ultimate forces and the calculated ultimate force for each fiber angle

$$r = \sum_{\theta} \left[F_{\exp}^{u}(\theta) - F_{\mathrm{num}}^{u}(\theta) \right] \quad (15)$$

where θ is the fiber angle, $F_{\exp}^{u}(\theta)$ is the average of the measured ultimate forces for the given fiber angle θ and $F_{\mathrm{num}}^{u}(\theta)$ is the calculated ultimate force for the given fiber angle θ. The flow chart of the identification process of the strengths is shown in **Figure 4**.
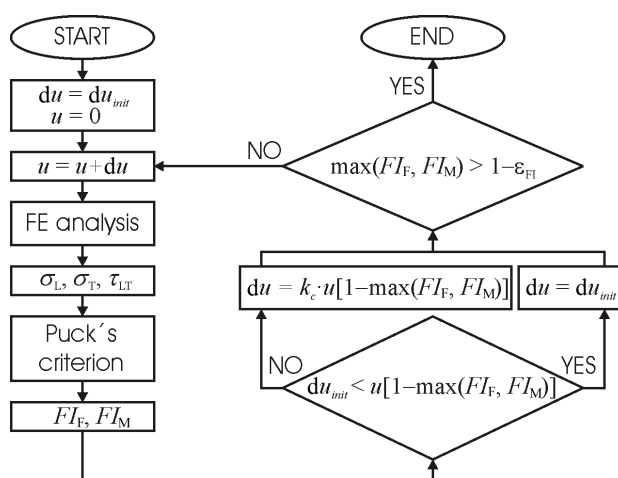
Figure 4: Identification process of the strengths
Slika 4: Proces identifikacije trdnosti

Let us briefly describe the flow chart in **Figure 4**. At the start of the identification process the initial displacement increment du_{init} is prescribed. The FE analysis is the next step. Subsequently, the failure analysis is performed and the failure indices (*FIs*) are calculated. These indices represent the level of the load with respect to the strength of the material. If the *FI* reaches one, the material is damaged. Once the *FIs* are calculated, the decision process that results in the displacement increment that is applied in the next step is performed. The constant k_{c} is used to improve the convergence speed. Once the matrix-failure index FI_{M} or the fiber-failure index FI_{F} reaches 1 (with the toleration $\varepsilon_{\mathrm{FI}}$) the identification process ends.

5 RESULTS

The identified elasticity parameters using the relationship (1) are shown in **Table 1**.

The decreasing tendency of the linear parameters and the increasing tendency of the non-linear part of the parameters with increasing temperature are evident. The exceptions are the shear modulus, which increases with the temperature 100 °C, and the Young's modulus for the fiber direction E_{L}, which remains constant.

Figure 3: Identification process of the elasticity parameters
Slika 3: Proces identifikacije parametrov elastičnosti

Table 1: Elasticity parameters used in (1)
Tabela 1: Parametri elastičnosti uporabljeni v (1)

| Parameter	25 °C	50 °C	75 °C	100 °C
E_L/GPa	111.58	111.69	111.47	111.59
E_T/GPa	8.48	7.30	6.50	4.77
G_{LT}/GPa	3.98	4.10	3.83	8.69
$(S_{111} \cdot 10^{-22})$/Pa^{-2}	-4.66	-4.67	-4.65	-4.49
$(S_{222} \cdot 10^{-19})$/Pa^{-2}	3.46	3.78	5.79	68.47
$(S_{666} \cdot 10^{-26})$/Pa^{-3}	12.75	21.97	58.93	442.27

Table 2 shows the identified parameters that were obtained by using relation (9).

Table 2: Elasticity parameters used in (9)
Tabela 2: Parametri elastičnosti uporabljeni v (9)

Parameter	25 °C	50 °C	75 °C	100 °C
E_L^0/GPa	106.26	107.71	106.19	107.51
E_T^0/GPa	8.25	7.15	6.38	4.35
G_{LT}^0/GPa	3.44	3.27	3.00	2.34
ε_L^0	1.44	0.72	1.49	0.78
σ_T^0/MPa	176.52	147.00	129.52	33.64
τ_{LT}^0/MPa	56.66	38.80	31.48	17.28
n_L	0.56	0.65	0.56	0.64
n_T	1.38	1.61	1.35	1.33
n_{LT}	1.44	1.83	1.53	1.89

The initial Young's modulus in the fiber direction is constant, while the rest of the initial moduli show a decreasing tendency. The asymptotic strain level does not show any dependence on the temperature. The asymptotic stress levels decrease with the increasing temperature. The values of the shape parameters are oscillating. **Figure 5** shows the temperature dependence of the residual (14). The increase of the residuals of the relation (1) with the increase of the temperature is obvious and the better capability of relation (9) is evident.
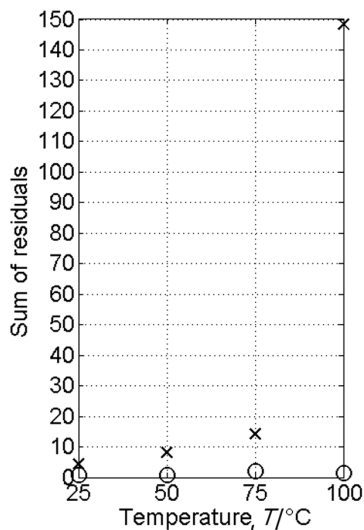
Figure 5: Sum of the residuals calculated with the use of (14) (× – (1), o – (9))
Slika 5: Vsota rezidualov, izračunana s uporabo (14) (× – (1), o – (9))

Table 3: Strength identified with the use of (1)
Tabela 3: Trdnosti določene z uporabo (1)

Strength	25 °C	50 °C	75 °C	100 °C
X^T/MPa	1937.2	1937.0	1937.1	1937.0
Y^T/MPa	36.7	38.2	32.8	16.9
S^L/MPa	58.4	49.3	39.2	73.6

Table 4: Strengths identified with the use of (9)
Tabela 4: Trdnosti izračunane z uporabo (9)

Strength	25 °C	50 °C	75 °C	100 °C
X^T/MPa	1937.0	1937.0	1937.1	1937.0
Y^T/MPa	36.4	38.2	32.8	16.9
S^L/MPa	61.0	49.3	39.2	73.6

The temperature independence of the strength X^T is visible from **Tables 3 and 4**. Also, the decreasing tendency of the strength Y^T and S^T is evident, except for the high value of the shear strength for 100 °C. The differences between the sums of the errors between the ultimate forces are negligible.

6 CONCLUSION

The capabilities of two types of non-linear stress-strain relations were investigated. The better suitability of the stress-strain relation based on the Ramberg-Osgood equations was proven. The influence of the viscoelasticity was neglected in the work.

The Puck's failure criterion was used for the failure analysis and the prediction of the strengths. It provides acceptable results for temperatures up to 75 °C.

Acknowledgements

7 REFERENCES

[1] H. T. Hahn, W. S. Tsai, Nonlinear elastic behavior of unidirectional composite laminae, Journal of Composite Materials, 7 (**1973**), 102–118

[2] J. M. Berthelot, Composite materials, Springer, New York 2004, p. 639

[3] F. Hassani, M. Shokrieh, L. Lessard, A fully non-linear 3-D constitutive relationship for the stress analysis of a pin loaded composite laminate, Composites Science and Technology, vol. 62 (**2002**) 3, 429–439

[4] T. Kroupa, V. Laš, Off-axis behavior of unidirectional FRP composite, Mater. Technol. 42 (**2007**) 3, 125–129

[5] A. Puck, H. Schürmann, Failure analysis of FRP laminates by means of physically based phenomenological models. Composites Science and Technology, vol. 58 (**1998**) 7, 1045–1067

[6] V. Laš, R. Zemčík, Progressive Damage of Unidirectional Composite Panels, Journal of Composite Materials 42 (**2008**), 25–44

NUMERICAL OPTIMIZATION OF THE METHOD OF COOLING OF A MASSIVE CASTING OF DUCTILE CAST-IRON

NUMERIČNA OPTIMIZACIJA POSTOPKA HLAJENJA PRI MASIVNEM ULIVANJU DUKTILNE ŽELEZOVE LITINE

Frantisek Kavicka[1], Bohumil Sekanina[1], Josef Stetina[1], Karel Stransky[1], Vasilij Gontarev[2], Jana Dobrovska[3]

[1]Brno University of Technology, Technicka 2, 616 69 Brno, Czech Republic
[2]University of Ljubljana, Aškerčeva 12, 1000 Ljubljana, Slovenia
[3]Technical University of Ostrava, Tr.17. listopadu, Ostrava, Czech Republic
kavicka@fme.vutbr.cz

An original application of ANSYS simulating the forming of the temperature field of a massive casting from ductile cast-iron during the application various methods of its cooling using steel chills. The numerical model managed to optimize more than one method of cooling but, in addition to that, provided serious results for the successive model of structural and chemical heterogeneity, and so it also contributes to influencing the as solidified microstructure. The file containing the acquired results from both models, as well as from their organic unification, brings new and simultaneously, remarkable findings of causal relationships between the structural and chemical heterogeneity and the local solidification time in any point of the casting. Therefore the determined relations enable the prediction of the local density of the spheroids of graphite in dependence on the local solidification time.

The calculated temperature field of a two-ton (500 × 500 × 1000) mm casting of ductile cast-iron with various methods of cooling has successfully been compared with temperatures obtained experimentally. This has created a tool for the optimization of the microstructure with an even distribution of the spheroids of graphite in such a way so as to minimize the occurrence of degenerated shapes of graphite, which happens to be one of the conditions for achieving good mechanical properties of castings of ductile cast-iron.

Key-words: ductile cast-iron, massive casting, cooling, temperature field, numerical model

Uporaba originalnega programa ANSYS omogoča simulacijo tvorbe temperaturnega polja v masivnem litoželeznem ulitku pri različnih metodah hlajenja z jeklenimi hladilnimi telesi. Z numeričnim modelom se lahko optimira več metod hlajenja, dodatno pa je mogoč izračun pomembnih rezultatov za modeliranje strukturne in kemijske heterogenosti, kar tudi prispeva k vplivu na lito mikrostrukturo. Dobljeni rezultati obeh modelov omogočajo pomembne ugotovitve o odnosih med strukturno in kemijsko heterogenostjo ter lokalnim časom strjevanja v poljubni točki ulitka in napoved lokalne gostote krogličastega grafita v odvisnosti od lokalnega časa strjevanja.

Izračunano temperaturno polje dvotonskega ulitka duktilne železove litine z izmerami (500 × 500 × 1000) mm je bilo v skladu z eksperimentalnimi rezultati pri različnih metodah hlajenja. Na podlagi teh ugotovitev je bilo izdelano orodje za optimizacijo mikrostrukture z enakomerno porazdelitvijo krogličastega grafita, s čimer se zmanjša pojav degeneriranih oblik grafita in se ustvarijo pogoji za dosego dobrih mehanskih lastnosti ulitkov duktilne železove litine.

Ključne besede: temperaturno polje, strjevanje, ohlajanje, numerična optimizacija, strukturna in kemijska heterogenost

1 INTRODUCTION

Solidification and cooling of a classically (i.e. gravitationally) cast casting and the simultaneous heating of the mould is, from the viewpoint of thermokinetics, a case of three-dimensional (3D) transient heat and mass transfer in a system consisting of the casting, mould and ambient. If the mass transfer is neglected and – from the three basic types of heat transfer – conduction is considered as the decisive, then the problem can be reduced to the solving of the Fourier equation. Here, the used 3D model of the temperature field of the system is based on the numerical finite-element method. The simulation of the release of the latent heats of phase or microstructural changes is carried out by introducing the thermodynamic enthalpy function. It enables the evaluation of the temperature field within the actual casting, chills and mould at any point in time within the process of solidification and cooling using contour lines (i.e. so-called iso-lines and iso-zones) or temperature-time curves for any nodal point of the system. It is possible to use all sophisticated sub-programs of ANSYS, such as automatic mesh generation, pre-processing and post-processing.

Having one's own numerical model available makes it possible to integrate one's own idea of the optimal course of solidification and cooling of the object under investigation in accordance with the latest findings and experiences of a specific operation. This is the main part of the role of the technological worker, irreplaceable by any computer technology whatsoever. Computer technology, despite its perfection, is only a tool enabling real-time prediction of his/her technical thinking and decisions.

The quality of a massive casting of cast iron with spheroidal graphite is determined by all the parameters and factors that affect the metallographic process and also others. This means the factors from sorting, melting in, modification and inoculation, casting, solidification and cooling inside the mold and heat treatment.

The heterogeneous pouring field is formed in such a way that the process of casting always takes a longer period of time. The different parts of the melt have trajectories of differing lengths within the mold and lose different amounts of heat. Therefore, the pouring times must be short enough in order to reduce the heterogeneity of the temperature field as much as possible. Otherwise there is the danger, especially with massive castings—even with modularly evened out pouring—of a temporally different course of eutectic solidification with a varying density of spheroids of graphite in its individual parts. The results are unequal mechanical properties along the section, especially a ductility decrease.

The cooling rate of during solidification and cooling in the mold is a significant quantity influencing the forming of the microstructure. It works not only on the morphology of the graphite but also on the segregation of elements in austenite and its transformation. The increasing rate of cooling increases the number of spheroids and improves the nodular character of the spheroids of graphite. It shortens the distances between the eutectic grains (i.e. cells) reducing the segregation on their boundaries. Simultaneously, it decreases the heterogeneity of the pouring temperature field, it minimizes the heat convection of liquid ductile cast-iron, attempting to prevent the forming of chunky graphite inside large cross-sections. The rate of cooling is not an isolated process. Furthermore, the oxygen balance and eutectic temperature influence the density of the spheroids with mutual interaction.

This paper deals with the simulation of solidification and cooling of a massive casting, with various ways of accelerated cooling using steel chills in order to reduce the heterogeneity of the pouring temperature field and to increase the rate of cooling of the casting. The results of the simulation are compared with experimentally measured temperatures. It seems that numerically controlled cooling enables the optimization of the technology of pouring of massive ductile cast-iron castings with spheroidal graphite.

2 NUMERICAL MODEL OF THE TEMPERATURE FIELD

The numerical model of the temperature field must observe two main goals: directed solidification as the basic condition for the healthiness of a casting and the optimization of the technology of pouring while optimizing the utility properties of the product. The main goal achieved—in terms of the economics—is the saving of liquid metal, molding materials, the saving of energy and the already mentioned optimization of pouring and also the improvement of the properties of the cast product.

The solidification and cooling of a classically cast (i.e. gravitationally poured) casting and the simultaneous heating of the mold is, from the viewpoint of thermokinetcs, a case of 3D transient heat and mass transfer.

In systems comprising the casting, the mold and ambient, all three kinds of heat transfer take place. Since these problems cannot be solved analytically—even with the second-order partial differential Fourier equation (1) (where mass transfer is neglected and conduction is considered as the most important of the three kinds of heat transfer)—it is necessary to engage numerical methods. Equation (1) describes the transient temperature field in a mold. Its properties k, c and ρ are considered to be constant.

$$\frac{\partial T}{\partial \tau} = \frac{k}{\rho \cdot c}\left(\frac{\partial^2 T}{\partial x^2} + \frac{\partial^2 T}{\partial y^2} + \frac{\partial^2 T}{\partial z^2}\right) \qquad (1)$$

The Fourier equation for a casting must be adapted so as to describe the temperature field of a casting in all its three phases: in the melt, in the mushy zone and in the solid phase. Here it is necessary to introduce the specific volume enthalpy $h_v = c\rho T$, which is dependent on temperature. The thermodynamic enthalpy function includes the latent heat of phase or structural changes. The equation then takes on the form

$$\frac{\partial h_v}{\partial \tau} = \frac{\partial}{\partial x}\left(k\frac{\partial T}{\partial x}\right) + \frac{\partial}{\partial y}\left(k\frac{\partial T}{\partial y}\right) + \frac{\partial}{\partial z}\left(k\frac{\partial T}{\partial z}\right) \qquad (2)$$

The specific heat capacity c, density ρ and heat conductivity k are also functions of temperature. The temperature of the general nodal point of the casting is obtained from the enthalpy-temperature dependence, which must be known for the relevant ductile cast-iron (**Figure 1**). The software pack ANSYS had been chosen
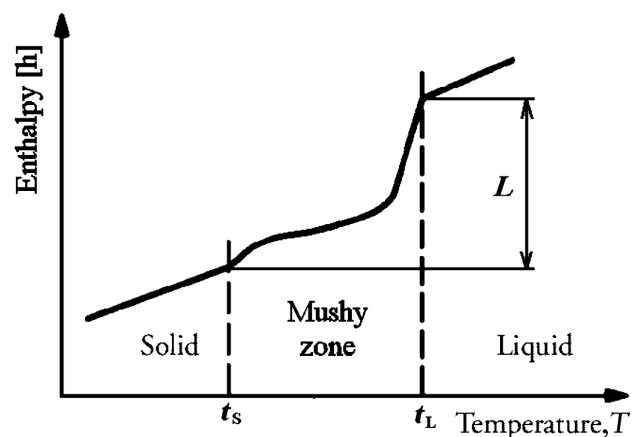

Figure 1: Enthalpy as a function of temperature
Slika 1: Odvisnost entalpije od temperature

for this investigation because it enables the application of the most convenient method of numerical simulation of the release of latent heat of phase and structural changes using the thermodynamic enthalpy function.

The program also considers the non-linearity of the task, i.e.:

- The dependence of the thermophysical properties (of all materials entering the system) on the temperature, and
- The dependence of the heat-transfer coefficients (on all boundaries of the system) on the temperature of the surface of the casting and mold.

ANSYS has an integrated mesh generator (i.e. pre-processing) as well as graphical output (i.e. post-processing) of the results and the user can change the pouring parameters, the dimensions of the casting-mold system and the dimensions of the elementary mesh volume before the actual calculation. The density of the mesh makes it possible to approximate the linear distribution of temperatures between individual points of the 3D mesh, and even within time intervals.

The accuracy of the numerical solution depends not only on the spatial and temporal discretization, but also on the precision with which the thermophysical properties of all materials entering the system are determined, and also on how precisely the boundary conditions are derived.

3 THE PROBLEM

The application of the 3D numerical model on a transient temperature field requires systematic experimentation, including the relevant measurement of the operational parameters directly in the foundry. The results of the measurement, which is focused on measuring temperatures, serve not only to verify the exactness of the model, but also to maintain continuity of the procedure: real process (risering, melting, pouring, solidification, etc.) → input data → numerical analysis → optimization → correction of real process (risering, melting, pouring, solidification, etc.).

A real (500 × 1000 × 500) mm ductile cast-iron block had been used for the numerical calculation and the experiment (**Figures 2 and 3**).

Temperature measurement (using thermocouples) and its successive confrontation with the calculation proved that it is possible to apply the numerical model on basic calculations of solidification and cooling of the casting. It is also possible to determine the temperature gradients, the rate of solidification and the local solidification times (i.e. the time for which the given point of the casting finds itself between the liquidus and solidus temperatures). The local solidification time θ (according to the analogy from steels) significantly influences the forming of the as solidified structure of the given material.

Figure 2: A picture showing the forming of casting no. 1 with chills on one side
Slika 2: Formiranje ulitka št.1 s hlajenjem na eni strani

Figure 4: The mesh inside the chills and casting no. 1
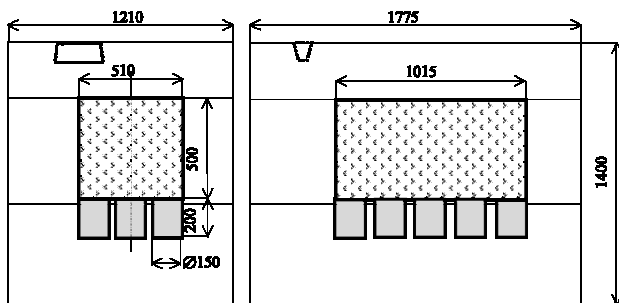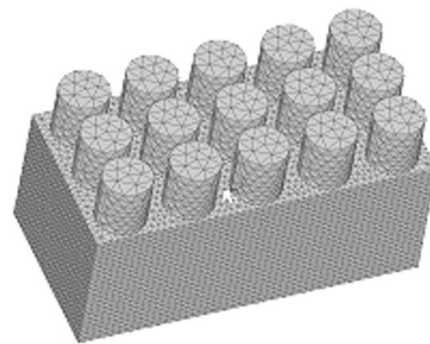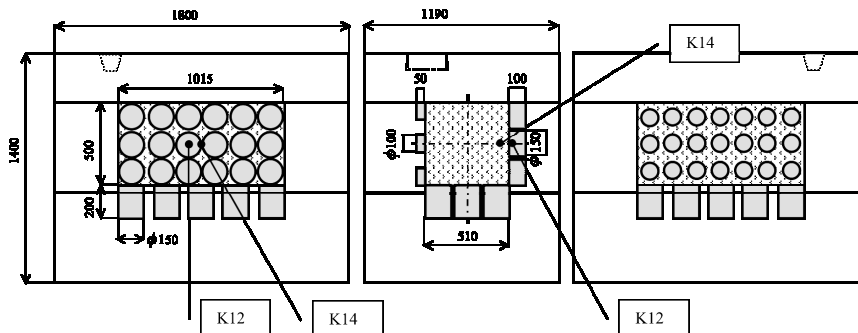**Slika 4:** Žična mrežica znotraj hladil in ulitka št. 1

Figure 3: A picture showing the forming of casting no. 2 with chills on three sides
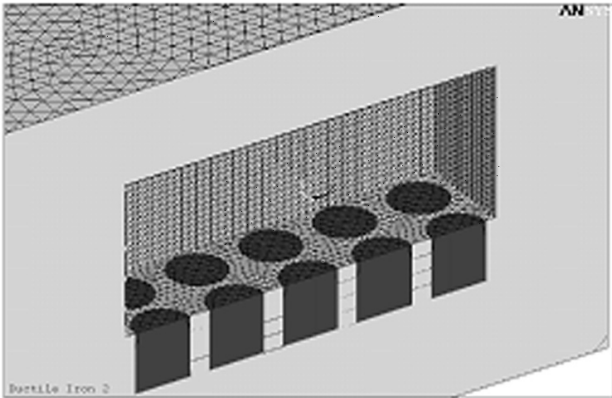**Slika 3:** Formanje ulitka št. 2 s hlajenjem na treh straneh

Figure 5: A detailed view of the mesh inside the chills and mold for casting no. 1
Slika 5: Podroben pogled na žične mrežice znotraj hladil in forme za ulitek št. 1

The investigated experimental castings weigh approximately 2 t. They were cast into sand molds with various arrangements of steel chills of cylindrical shape. The dimensions of the castings, the mold, the chills and their arrangements are illustrated in **Figures 2 and 3**.

Figures 4 and 5 show an example of the mesh generated by ANSYS.

4 TEMPERATURE MEASUREMENT

The temperature was measured using K- and B-type thermocouples and special thermocouple probes of type PtRh6 – PtRh30. The recording was carried out by the data-acquisition device GRANT 1250. The measuring ends of the thermocouples were placed in holes of 2 mm in diameter. The initial temperature of the mold and chills was approximately 20 °C, the mold was filled through the top inlet gate with a melt at 1300 °C. The courses of the temperatures were measured on casting no. 1 for 19 h 11 min and 19 h 20 min on casting no. 2 after casting.
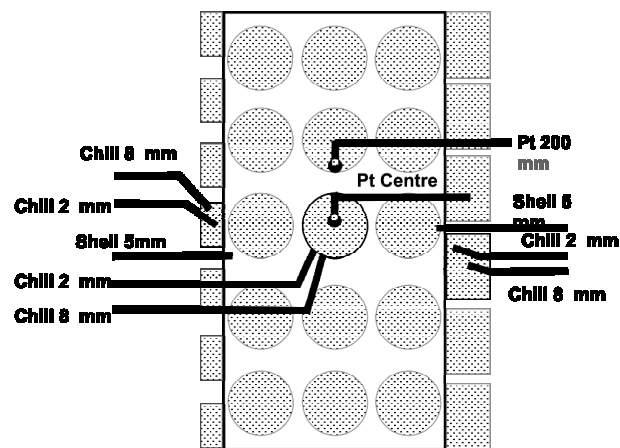
Figure 6: The measured positions for casting no. 2
Slika 6: Lega hladil pri ulitku št. 2

Figure 7: The installations of the thermocouples while molding casting no. 2
Slika 7: Namestitev termočlenov med formanjem ulitka št. 2

The positions of the probes and a view of the actual installation in mold no. 2 are illustrated in **Figures 6 and 7**.

5 CALCULATION AND EXPERIMENTAL RESULTS

The points in casting no. 2 and the chill were selected for comparison (**Figures 3 and 6** respectively). The computation and experimental curves are in **Figures 8 and 9**.

It is obvious, that in the compared points of the mold and chills, the results from the numerical model correspond to those measured, which applies to most other places where both the mold and chills were measured. In the centers of the casting it was not possible to carry out the comparison due to a failure in the thermocouple probes.

The iso-zones, calculated in castings 1 and 2 and in the chills in various parts after casting, are illustrated in

Figure 8: The measured and calculated temperature history in casting no. 2, 5 mm beneath its surface
Slika 8: Merjene in izračunane temperature 5 mm pod površino ulitka št. 2

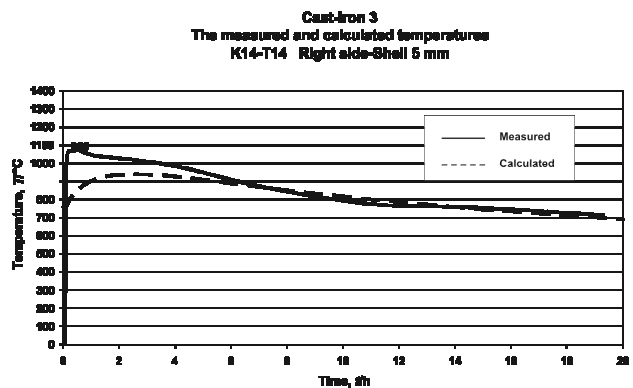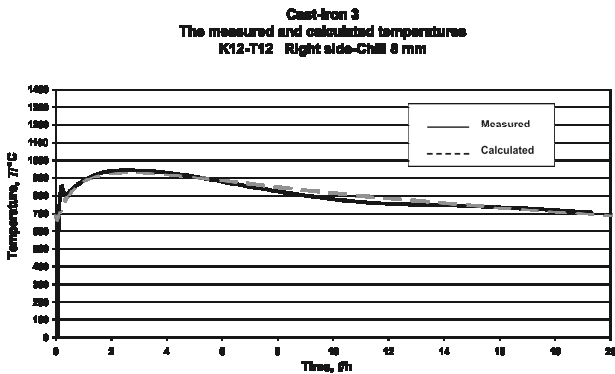**Figure 9:** The measured and calculated temperature history in the chill for casting no. 2

Slika 9: Merjene in izračunane temperature v hladilih ulitka št. 2

Figure 11: The calculated iso-zones in casting no. 2 and in its chills a) $\tau = 1$ h, b) $\tau = 4,5$ h

Slika 11: Izračunane izo-temperaturne cone v ulitku št. 2 s hladili a) $\tau = 1$ h, b) $\tau = 4,5$ h

Figures 10 and 11. The comparison of the iso-zones, including the mushy zone in castings 1 and 2 shows that this time is, relatively, not very much influenced by the increase in the number of chills or by the increase in the number of walls on which the chills are mounted.

The total solidification time of casting no. 1 is 5:08:10 hours and 4:33:35 hours of casting no. 2. Even the various arrangements of chills did not significantly influence the difference in the total solidification time.

6 CONCLUSION

The numerical models of the temperature field of the solidifying castings of different authors have observed two main goals: directed solidification as the basic condition for the healthiness of a casting and the optimization of the technology of pouring, while, optimizing the utility properties of the product. Achieving these goals is conditioned by the ability to analyze and to successively control the influence of the deciding factors that either characterize the solidification process or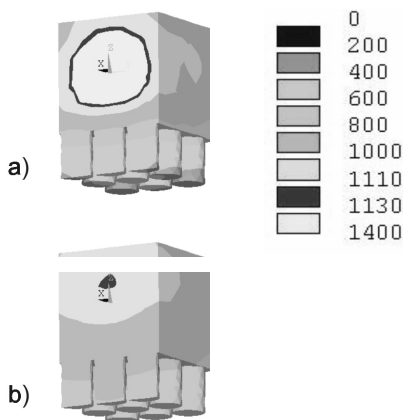 accompany it. It is advantageous to focus the analysis especially on a breakdown of the causes behind the formation of the non-homogeneities within the casting, considering the latent and structural changes, on the thermokinetic formation of the contractions and cavities, on the prediction of their forming, thus, managing to optimize the shape and size of the risers, the method of insulation, the treatment of the level, etc. The main economic goal observed is the saving of liquid material, molding and insulation materials, the saving of energy and the already mentioned optimization of pouring and the properties of the cast product.

This paper has been discussing an original application of ANSYS for the investigation into a temperature field of a massive casting of ductile cast-iron with spheroidal graphite, which makes it possible to evaluate the local solidification times and the local rates of solidification and cooling. Using these parameters, together with the model of microstructural and chemical heterogeneity, it is possible to design the technology of pouring a casting of massive cast-iron with spheroidal graphite (i.e. for example a system of chills) in such a way so as to optimize the quality of the casting even from the viewpoint of its pouring structure.

Figure 10: The calculated iso-zones in casting no. 1 and in its chills a) $\tau = 1$ h, b) $\tau = 5$ h

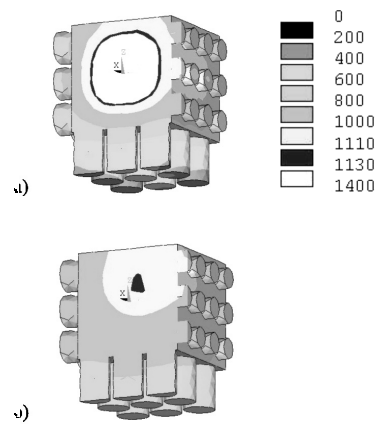**Slika 10:** Izračunane izotemperaturne cone v ulitku št. 1 s hladili a) $\tau = 1$ h, b) $\tau = 5$ h

NOMENCLATURE

c	specific heat capacity	J kg^{-1} K^{-1}
h_v	specific volume enthalpy $h_v = h\rho$	J m^{-3}
k	heat conductivity	W m^{-1} K^{-1}
τ	time	s
x, y, z	axes in given directions	
T	temperature	K
ρ	density	kg m^{-3}

7 REFERENCES

[1] Popela P., Stochastic programming models and methods for technical applications. Folia Fac. Sci.Nat. Univ. Masarykianae Brunensis, Mathematica, 11 (**2002**), 181–206

[2] Svantner M., Honner M., The model of cooling of a casting, Research report of the Research Centre of New Technologies, West Bohemian University in Plzen, 2001

[3] Kovarik J., Vavroch O., Determining thermophysical properties of mould mixtures, Research report VZVÚ 07687 Skoda Research Ltd., Plzen 1993

[4] Kavička F., Stetina J.: A numerical model of heat transfer in a system a plate casting-mold-suroundings for optimization. Proceedings of the Conference of the ASME, Seattle, USA, July 2000, 161–168

[5] Kavicka F., Stetina J.. Anumerical model of heat transfer in a system plate-mold-surroundings. Proceedings of the 6th International Conference on Advanced Computational Methods in Heat Transfer, Spain, Madrid, June 2000, 95–104

[6] Kavicka F. et al.: Optimisation of properties and foundry technology of heavy weight ductile cast-iron castings. Final report of GACR project No.106/01/1164, Brno, 2003

ELECTRICAL CONDUCTIVITY OF SINTERED LSM CERAMICS

ELEKTRIČNA PREVODNOST SINTRANE LSM-KERAMIKE

Marjan Marinšek

University of Ljubljana, Faculty of Chemistry and Chemical Technology, Aškerčeva 5, Ljubljana, Slovenia
marjan.marinsen@fkkt.uni-lj.si

The carbonate co-precipitation route was applied for batch $La_{0.85}Sr_{0.15}MnO_3$ (LSM) preparation as an alternative synthesis method to the solid-state reaction. Because co-precipitation is a wet-chemistry solution process, the maximum LSM homogeneity was achieved. The microstructural characteristics, such as the porosity and grain size of the prepared LSM elements, were controlled by subjecting the green bodies to various sintering conditions. The LSM sintered bodies with relative sintered densities as high as 95 % were prepared at sintering temperatures not higher than 1100 °C. The microstructure of the prepared LSM was characterized by digital online image analysis and the microstructural parameters were determined for the ceramic phase as well as for the porosity. The electrical characteristics of the sintered LSM elements were, for the first time in the literature, described with respect to a model for the sine-wave approximation of the conductivity change for porous materials. The observed results of the relative conductivity σ/σ_0 vs. the relative density ρ/ρ_0 dependence were essentially consistent with the sine-wave approximation. As an absolute value, the highest $\sigma = 65$ S/cm at 800 °C was measured for a sample with $\rho/\rho_0 = 99.58$ %.

Key words: LSM co-precipitation, microstructure, electrical conductivity, sine-wave approximation of conductivity

$La_{0,85}Sr_{0,15}MnO_3$ (LSM) je bil pripravljen po metodi karbonatne koprecipitacije kot alternativa metodi reakcije v trdnem. Z uporabo koprecipitacijske metode kot ene izmed tehnik mokre kemije nam je uspelo pripraviti zelo homogene LSM-prahove. Mikrostrukturne lastnosti končnih, pripravljenih LSM-elementov, kot sta poroznost in velikost zrn, smo spreminjali s sintranjem LSM-surovcev pri različnih pogojih. Uspelo nam je pripraviti sintrane LSM-elemente z relativno sintrano gostoto ≈95 % pri temperaturtah sintranja, ki niso bile višje kot 1100 °C. Bolj podrobna karakterizacija mikrostrukture sintranih elementov je bila opravljena z analizo digitalnih slik. Električne lastnosti sintranih LSM-elementov smo pojasnili s teoretičnim modelom vrtenine za opis električne prevodnosti porozne keramike, kar je tudi prvi tovrsten opis LSM-keramike. Rezultati določitve relativne prevodnosti σ/σ_0 LSM-keramike kot funkcije njene relativne gostote ρ/ρ_0 relativno dobro sledijo predlaganemu teoretičnemu modelu. Najvišjo absolutno izmerjeno vrednost električne prevodnosti $\sigma = 65$ S/cm pri 800 °C je imel vzorec z relativno gostoto $\rho/\rho_0 = 99,58$ %.

Ključne besede: LSM-koprecipitacija, mikrostruktura, električna prevodnost, "sine-vawe" model prevodnosti

1 INTRODUCTION

Lanthanum strontium manganite ($La_{1-x}Sr_xMnO_3$, LSM) has been extensively used as a cathode material for solid-oxide fuel cells (SOFCs). It offers a high electronic conductivity, a high catalytic activity for oxygen reduction as well as chemical and thermal compatibility with the yttria-stabilized zirconia (YSZ) electrolyte at the operating temperature[1,2]. In the present generation of SOFCs, the nominal composition of $La_{1-x}Sr_xMnO_3$ (x < 0.2) is normally used[3,4]. The use of LSM-based cathode materials depends not only on their chemical, structural and thermodynamic characteristics, but also on their final microstructure, grain size, pore size and pore-size distribution[5–7].

Various preparation techniques have been reported for LSM synthesis. In general, perovskite manganites are synthesized at high temperatures using a standard ceramic technique. However, when utilizing a solid-state reaction for LSM preparation, the homogeneity and final microstructure of the material are more difficult to control, due to the fact that the conventional ceramic synthesis process is based on the diffusion of components in the solid state at high temperatures. In this respect,

several preparation techniques based on solution chemistry methods, such as the citrate-gel process[8-12], the sol-gel process[13-15], combustion syntheses[16,17] and the co-precipitation technique[18,19] have also been tested for the preparation of highly homogenous and fine LSM powders.

The characterization of LSM and some other perovskite powders such as SOFC cathodes or oxygen membranes prepared by different chemical routes was made by Sfeir et al.[20], while a comprehensive study of the effect of the synthesis route on the catalytic activity of LSM was performed by Bell et al.[21]. The results of these studies implied that the carbonate co-precipitation synthesis route is especially interesting since it delivers a finer powder with a more homogeneous composition and surface structure and is, thus, more suited to mixed-conductor applications in SOFC systems. The groundwork of the co-precipitation method for the LSM preparation was done by Tanaka et al., where Na_2CO_3 was used as the precipitating agent[22]. However, one of the serious drawbacks of the method is the incorporation of Na^+ ions into the precipitate due to the use of Na_2CO_3. Another co-precipitation-based LSM preparation was developed

by Ghosh et al.,[19] using ammonium carbonate as the precipitating agent.

LSM is a perovskite oxide ABO_3 where the La^{3+} ions at the A-sites are partially substituted by Sr^{2+} ions. $LaMnO_3$ is a p-type semiconductor due to the small polaron hopping of holes[23] between the Mn^{3+} and Mn^{4+} ions. The doping of Sr into $LaMnO_3$ increases the electrical conductivity considerably because of the increased number of holes[24]. However, in order to serve as a cathode material in an operating fuel cell, besides the appropriate electro-catalytic properties, the LSM also has to exhibit suitable microstructure characteristics, including ≈30 % open porosity. Changing the porosity, going from a dense to a more porous structure, will again alter some of the electrical characteristics of the material, since the apparent conductivity of sintered materials is sensitive to their relative density. To describe the relationship between the conductivity of the porous material and its relative density, a novel mathematical approach was proposed[25]. In this new method of interpretation, where as a first approximation, porous material is represented by a uniaxial string of spheres along the direction of the potential gradient and then remodeled into a rotating body, the conductivity of highly porous ceramic materials can be expressed with a model of a rotating sine-wave function. By changing the ratio of the contribution of two sine-waves, one representing the shape of each grain and the other the shape of the bottleneck between the particles, the change of the electrical conductivity σ vs. the change of the material's relative density ρ/ρ_0 can be represented.

In the present work, the carbonate co-precipitation route for batch LSM preparation was applied. Being a solution process, the maximum product homogeneity with minimum secondary-phase addition can be achieved. The aim of the study is a description of the electrical conductivity behavior of the prepared LSM bodies with respect to the material's microstructure characteristics. For the fist time, the specific electrical conductivity of porous LSM is explained with the model of a rotating sine-wave function.

2 EXPERIMENTAL PROCEDURE

In order to prepare stock solutions of 0.5-M lanthanum nitrate and strontium nitrate, lanthanum oxide (La_2O_3) and strontium carbonate ($SrCO_3$) were separately, carefully dissolved in concentrated nitric acid, while manganous nitrate ($Mn(NO_3)_2 \cdot 4H_2O$) was dissolved in distilled water. For the $La_{0.85}Sr_{0.15}MnO_3$ preparation, predetermined amounts of each solution were then mixed. The mixed solution was added drop-wise to a precipitating bath containing an aqueous solution of ammonium carbonate in which the amount of ammonium carbonate was in 50 % excess for the complete precipitation of the mixed La-Mn-Sr-precursor. The pH of the precipitating bath was kept constant at 8.0 by

small additions of aqueous ammonia. The temperature of the reaction mixture in the precipitating bath was adjusted to 65 °C and kept constant. The precipitation reaction took place under a CO_2 atmosphere to prevent any undesired oxidation of the manganese to MnO_2. The reaction time for the complete co-precipitation process was approximately 3 h.

Typical quantities of the initial precursors consumed in one cycle of the bath precipitation were 100 g of $(NH_4)_2CO_3$ dissolved in 2.5 L of H_2O, 854 mL of 0.5-M Mn-precursor solution, 363 mL of 0.5-M La-precursor solution, and 128 mL of 0.5-M Sr-precursor solution. Such a reaction mixture yielded approximately 100 g of the final, calcined LSM powder.

The filtered precipitate was washed several times with a 0.125-M aqueous ammonium-carbonate solution and then dried first at room temperature in a CO_2 atmosphere for several hours and afterwards for six hours at 110 °C in air. Prior to calcination in a muffle furnace at 1000 °C for one hour, the dried powder was ground in an agate mortar. Calcined LSM powders were then wet milled in a ball mill in isopropanol. To achieve a higher morphological homogeneity the wet-milled powders were further subjected to atritor milling.

Thus prepared, the LSM powders were pressed into tablets (Φ = 6 mm, $h \sim 4$ mm, P = 200 MPa) and sintered at various temperatures from 1000 °C to 1330 °C for one hour.

The samples were characterized with the X-ray powder-diffraction technique using a D4 ENDEAVOR diffractometer. The shrinkage during the sintering was measured with a LEITZ WETZLAR heating microscope. After sintering and polishing the samples were thermally etched and analyzed by SEM (Zeiss FE SUPRA 35 VP). The quantitative analysis of the microstructures was performed using a Zeiss KS300 3.0 image analyzer. In order to get accurate data on the electrical resistivity of the prepared and sintered pellets as a function of temperature, the four-point electrical resistivity method was used.

3 RESULTS AND DISCUSSION

The precipitated and calcined powders were submitted for an XRD examination (**Figure 1**). For XRD study purposes the calcination of the precursor carbonate-hydroxide powder was carried out in the temperature range 1000–1400 °C. According to **Figure 1**, calcination at 1000 °C is quite sufficient for a complete perovskite LSM phase formation. Another apparent characteristic from the XRD results is that only traces of the residual secondary phases La_2O_3 or $La(OH)_3$ are still present after the calcination ($La(OH)_3$ resulting from the reaction of the La_2O_3 with moisture). Additionally, no Mn-oxide secondary phases were detected with the XRD analysis. During the calcination at higher temperatures (1100–1400 °C) the secondary phases are completely
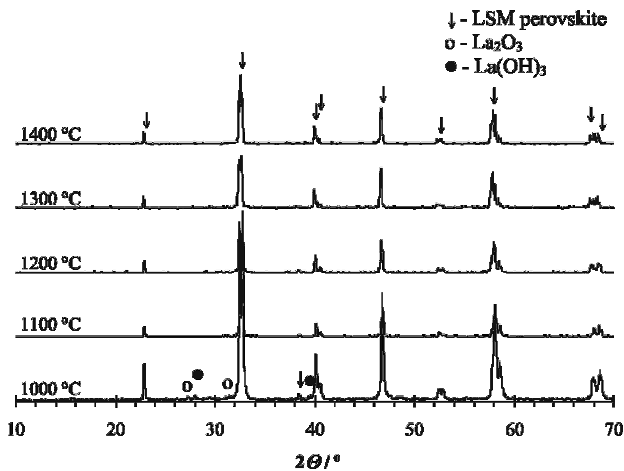
Figure 1: XRD patterns of the synthesized powders calcined at different temperatures
Slika 1: Praškovni posnetki sintetiziranih vzorcev, kalciniranih pri različnih temperaturah

Figure 3: Shrinkage curves of LSM tablets after powder wet milling or after additional atritor milling
Slika 3: Krivulje sintranja LSM-surovca po mokrem mletju prahu oziroma po dodatnem atritorskem mletju prahu
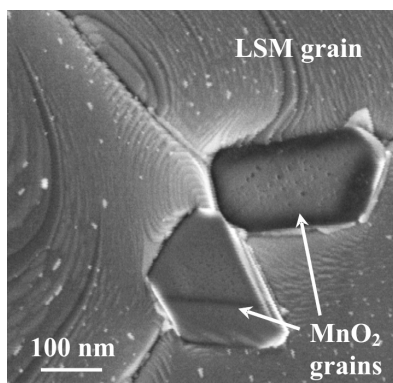
dissolved in the perovskite structure. The relatively small amount of secondary phases in the sample calcined up to 1000 °C makes the co-precipitation method favorable when compared to synthesis processes that are based on the diffusion of components in the solid state. Namely, if the solid-state reaction is employed for the LSM preparation, the amount of secondary phases is normally greater.
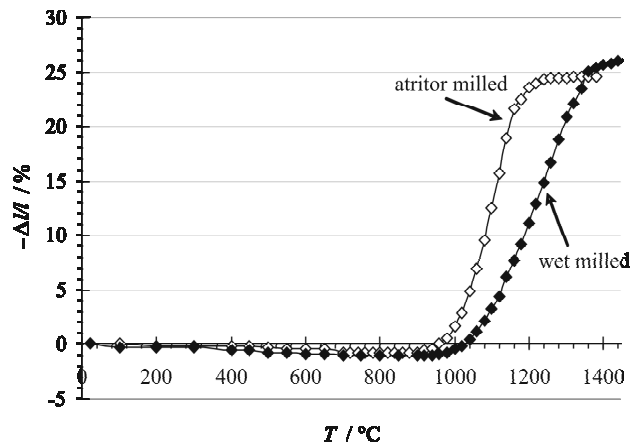
At this point, it is necessary to mention that secondary phases may nevertheless appear in the LSM structure, even in the case when the calcination temperature exceeds 1100 °C. Specifically, a precise SEM analysis revealed that calcination or sintering of the prepared LSM at temperatures above 1100 °C caused the reprecipitation of MnO_2 at the LSM grain-boundary region (**Figure 2**). The amount of reprecipitated MnO_2 at 1100 °C is relatively low (the volume fraction below 1 % of the material) but is increased to 3.9 % when the material is thermally treated at 1330 °C for 1 h.

One of the principal characteristics LSM has to exhibit is sintering at relatively low temperatures (less than 1200 °C). This is very important from the applica-

tion point of view. If the material is used as a cathode in SOFC systems and co-sintered with other cell layers, then sintering at temperatures above 1200 °C may cause some highly undesirable reactions with neighboring materials[26,27]. For this reason, the morphological homogeneity of LSM powders is essential for achieving material densification at relatively low temperatures. During LSM sinterability tests, the best results were achieved when a combination of milling methods was used (grinding in an agate mortar, wet milling in a ball mill and atritor milling). After wet milling in a ball mill in isopropanol, the average particle size $d_{av.}$ was determined to be 2.45 μm (standard deviation σ 1.98 μm). After 3 hours of additional atritor milling $d_{av.}$ was lowered to 0.57 μm (σ 0.52 μm). Such a combination of homogenization operations substantially lowered the sintering temperature of the LSM tablets (**Figure 3**).

After successfully reducing the sintering temperature, a series of tablets in the green state was prepared and sintered at various temperatures in order to alter the densities of the sintered elements. Prior to establishing the LSM's electrical characteristics with respect to its microstructure, a complete, quantitative microstructure analysis was performed on sintered and polished elements (**Table 1**, **Figure 4**). According to the results summarized in Table 1, rather dense elements with relative densities of more than 92 % can be prepared at sintering temperatures T_s as low as 1090 °C. This is of prime importance when multilayered structures of SOFCs are prepared; it is very important that the material is capable of densification at relatively low temperatures, resulting in good particle-to-particle connections, especially in cases where a high electrical conductivity is required.

In contrast to the sintered density, the porosity of the sintered elements decreased with an increased sintering temperature. The elements' porosity was determined from the material density as the geometrical porosity ε (ε

Figure 2: Microstructure of LSM sample thermally treated at 1330 °C for 1 hour
Slika 2: Mikrostruktura LSM-vzorca, obdelanega pri 1330 °C 1 h

Table 1: Microstructural parameters of the sintered LSM bodies
Tabela 1: Mikrostrukturne značilnosti sintranih LSM-tabletk

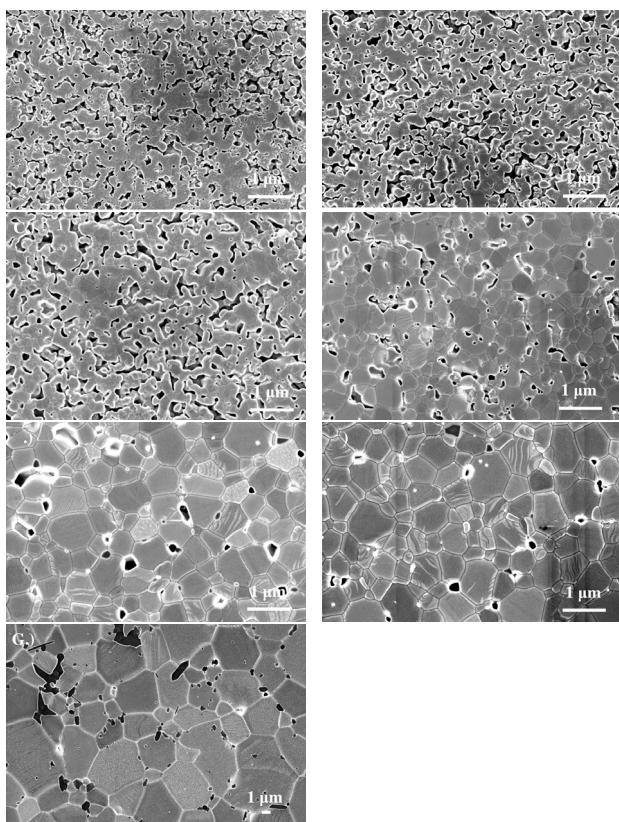| sample	A	B	C	D	E	F	G
sintering temperature T_s / °C	1000	1015	1024	1060	1090	1100	1330
relative sintered density ρ_s / %	57.3	65.8	70.1	83.0	92.7	94.1	98.2
porosity (geometrical) ε / %	42.7	34.2	29.9	17.0	7.3	5.9	1.8
porosity (microstructural) ε' / %	43.2	28.6	25.4	15.9	6.0	4.4	0.9
mean particle diameter $\bar{d} \cdot 10^2$ / μm	5.7	8.9	20.0	28.0	29.0	34.0 (16.0)	506.0 (33.0)
standard deviation $\zeta \cdot 10^2$ / μm	4.9	5.9	7.9	12.6	18.8	25.4	163.2
shape factor Ψ	0.53	0.69	0.73	0.79	0.94	0.93 (0.63)	0.90 (0.51)
intercept length in x $d_x \cdot 10^2$ / μm	8.7	11.1	24.0	31.0	38.0	40.0 (16.0)	520.0 (39.0)
intercept length in y $d_y \cdot 10^2$ / μm	8.2	8.2	22.0	33.0	30.0	43.0 (15.0)	749.0 (24.0)
No. of analyzed particles	782	855	848	419	136	110	90
vol. fraction of MnO_2 phase / %	/	/	/	/	/	1.16	3.94

$= 1 - \rho/\rho_0$) and from the quantitative microstructure analysis ε'. Both values, ε and ε', are in relatively good agreement. The sintering temperature also substantially influences the size of the LSM particles. The mean particle size in each case was determined as a diameter of the area analogue circle $\bar{d}$ as well as the intercept length in the x or y directions d_x and d_y. With increasing sintering temperatures, all the values $\bar{d}$, d_x and d_y increased and the LSM particles become increasingly

Figure 4: Microstructure of LSM elements sintered at various temperatures
Slika 4: Mikrostruktura LSM-tabletk, sintranih pri različnih temperaturah

spherical (shape factor Ψ). As mentioned previously, temperatures above 1100 °C may cause re-precipitation of the secondary phase MnO_2. The values $\bar{d}$, d_x, d_y and Ψ describing the formed MnO_2 particles are summarized in **Table 1** in brackets.

Since the LSM in SOFC applications is prepared as a relatively thin porous layer, it is necessary to establish the relationship between the material's microstructure and its electrical characteristics. The appropriate electrical conductivity of the material prepared as a dense element is one of the principal requirements. However, considering only the electrical conductivity data of the dense element without relating this data to the real material microstructure is insufficient. The electrical conductivity of the porous material is described not only by its specific electrical conductivity σ_0 but also by the element's relative density and the degree of connection between the particles along the potential gradient. In this respect, the sine-wave approximation considers a highly porous ceramic element as the repeating pattern of a uniaxial string of spheres. In this simplified approach to describing the microstructure, the volume of the rotating string is controlled by the contribution of two sine-waves. The progress of the sintering is described by changing the ratio of the contribution of the two sine-waves to the string volume (changing the parameter c as described by Mizusaki et al[23]). Finally, the change of the relative specific electrical conductivity σ/σ_0 vs. the change in the material's relative density ρ/ρ_0 can be presented.

Results describing the apparent conductivity of the sintered materials vs. the temperature with respect to their relative density or porosity are shown in **Figure 5**. The apparent conductivity increases with temperature, indicating the semi-conductive nature of the LSM ceramics. Since the LSM's density was controlled through a sintering process (higher densities were obtained if T_s was higher) it was to be expected that the specific conductivities σ should also reach higher values with progress in the particle-to-particle contact. As an

absolute value, the highest σ = 65 S/cm at 800 °C was measured for a sample with ρ/ρ_0 = 99.58 %.

The relationship relative conductivity (σ/σ_0) vs. relative density (ρ/ρ_0) or porosity (ε) is demonstrated in **Figure 6**. For the σ_0 value, the highest measured σ value was adopted (σ_0 = 65 S/cm), while ρ_0 was the theoretical density of $La_{0.85}Sr_{0.15}MnO_3$ (ρ_0 = 6.595 g/cm³). The observed results of the relative conductivity σ/σ_0 vs. relative density ρ/ρ_0 dependence are essentially consistent with the sine-wave approximation of the conductivity change for porous materials. The scattering of the observed results around the theoretically predicted curves may be attributed to the inaccuracy of the conductivity measurements or some microstructure defects in the measured bodies. Because of the simplification of the sine-wave modeling regarding the material's microstructure, it is impossible to discuss precisely the relationship between the theoretical predictions and the experimental results. That is to say, contrary to the assumption used in the mathematical model, the grain size and shapes are not homogeneous and the packing of the grains is disordered. To incorporate the inhomogeneity and disorder, such as micro-cracks, the low-scale material inhomogeneity, the inhomogeneous grain size and shape or the local packing disorder into the sine-wave model, a more advanced approach to a mathematical description of the microstructure will be needed.

However, a comparison of the results presented in **Figure 6** revealed that the LSM's relative conductivity convergences on 0 at the relative density 0.45–0.55, a value close to the relative density of as-pressed powders (green density). Such a relationship is not surprising; ceramics are generally prepared from green parts that consist of isolated particles of material. In as-pressed powders, the particles are isolated, except for the
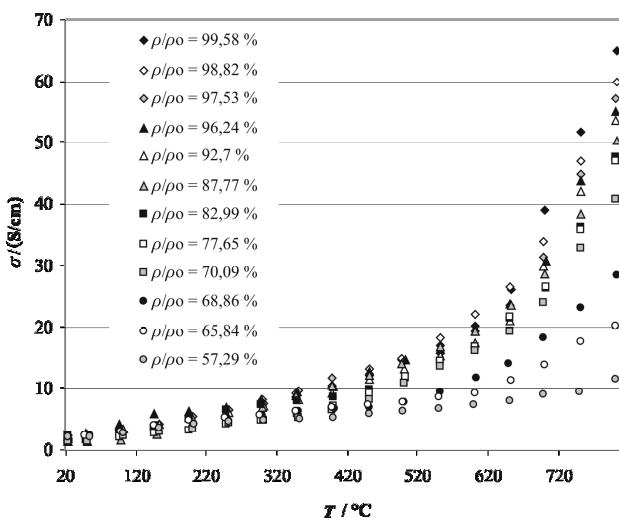
Figure 6: Calculated relationships between the relative conductivity σ/σ_0 and the relative density ρ/ρ_0 or porosity ε for different parameters c; (solid, 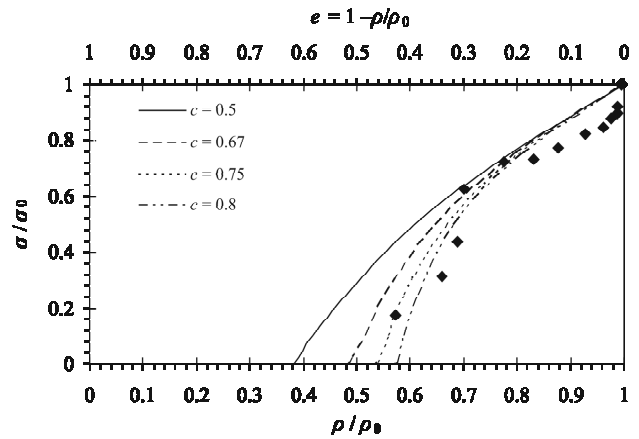dashed and dotted lines as described by Mizusaki et al[25]) and the observed trend of the measured data (◆ LSM tablets). The relative shape parameter c determines the contribution of the two sine-waves in describing the shape of the cross-section of the particle during sintering.

Slika 6: Odnos med relativno prevodnostjo σ/σ_0 in relativno gostoto ρ/ρ_0 oziroma poroznostjo ε LSM-tablet z ozirom na mikrostrukturni parameter c (polna in črtkane črte). Parameter c določa prispevek obeh sinusnih funkcij, ki opisujeta obliko delca med sintranjem.

point-contacts between them, i.e., it is not the material but the void space that is continuous. The electrical conduction in green wares is strongly hindered by the limited contact between the particles, although the apparent density is normally in the range 40–60 %. With increasing sintering temperatures, the relative sintered densities increase, ensuring a better contact between the particles, which is demonstrated through higher relative conductivities.

4 CONCLUSIONS

LSM was prepared using the carbonate co-precipitation route. The relatively small amount of secondary phases in the synthesized and subsequently calcined sample up to 1000 °C makes the co-precipitation method favorable when compared to synthesis processes that are based on the diffusion of components in the solid state. During LSM sinterability tests, the best results were achieved when a combination of milling methods was used (grinding in an agate mortar, wet milling in a ball mill and atritor milling). Such combinations of homogenization operations may substantially lower the sintering temperature of the LSM tablets. Rather dense elements, with relative densities greater than 92 %, can be prepared at sintering temperatures T_s as low as 1090 °C. The electrical conductivity behavior of the prepared LSM bodies was determined with respect to the material's microstructure characteristics. The apparent conductivity of the prepared LSM bodies increased with temperature, indicating their semi-conductive nature. The relationship between the relative conductivity (σ/σ_0) vs. the relative density (ρ/ρ_0) or the porosity (ε) was essentially con-

Figure 5: Specific conductivity vs. temperature for a series of LSM elements cermets with various relative densities
Slika 5: Specifična prevodnost LSM-keramike različne relativne gostote kot funkcija temperature

sistent with the sine-wave approximation of conductivity change for porous materials.

5 LITERATURE

[1] M. Kakihana, Sol-gel preparation of high temperature superconducting oxides, *J. Sol-Gel Sci. Technol.*, 6 (**1996**), 7–55

[2] N. Q. Minh, Ceramic Fuel Cells, *J. Am. Ceram. Soc.*, 76 (**1993**), 563–588

[3] B. C. H. Steele, Material science and engineering: the enabling technology for the commercialization of fuel cell systems, *J. Mater. Sci.*, 36 (**2001**), 1053–1068

[4] M. L. Perry, T. F. Fuller, A historical perspective of fuel cell technology in the 20th centuary, *J. Electrochem. Soc.*, 149 (**2002**), S59–S67

[5] R. Mahesh, R. Mahendiran, A. K. Raychaudhuri, C. N. R. Rao, Effect of particle size on the giant magnetoresistance of $La_{0.7}Ca_{0.3}MnO_3$, *Appl. Phys. Lett.*, 68 (**1996**), 2291–2293

[6] Y. Huang, Z. Xu, C. Yan, Z. Wang, T. Zhu, C. Liao, Soft chemical synthesis and transport properties of $La_{0.7}Sr_{0.3}MnO_3$ granular perovskites, *Solid State Commun.*, 114 (**2000**), 43–47

[7] N. Zhang, W. Ding, W. Zhong, D. Xing, Y. Du, Tunnel-type giant magnetoresistance in the granular perovskite $La_{0.85}Sr_{0.15}MnO_3$, *Phys. Rev.*, B56 (**1997**), 8138–8142

[8] A. Chakraborty, P. S. Devi, S. Roy, H. S. Maiti, Low-temperature synthesis of ultrafine $La_{0.84}Sr_{0.16}MnO_3$ powder by an autoignition process, *J. Mater Res.* 9 (**1994**), 986–991

[9] P. A. Lessing, Mixed-cation oxide powders via polymeric precursors, *Ceram. Bull.* 68 (**1989**), 1002–1007

[10] H.U. Anderson, Review of p-type doped perovskite materials for SOFC and other applications, *Solid State Ionics* 52 (**1992**), 33–41

[11] K. Prabhakaran, J. Joseph, N. M. Gokhale, S. C. Sharma, R. Lal, Sucrose Combustion Synthesis of $La_xSr_{1-x}MnO_3$ ($x \le 0.2$) powders, *Ceramics International*, 31 (**2005**), 327–331

[12] Y. Huang, Z. Xu, C. Yan, Z. Wang, T. Zhu, C. Liao, Soft chemical synthesis and transport properties of $La_{0.7}Sr_{0.3}MnO_3$ granular perovskites, *Solid State Commun.*, 114 (**2000**), 43-47

[13] S. Bilger, E. Syskakis, A. Naoumidis, H. Nickel, Sol-Gel Synthesis of Strontium-Doped Lanthanum Manganite, *J. Am. Ceram. Soc.* 75 (**1992**), 964–970

[14] Y. Shimizu, T. Murata, Sol-gel synthesis of perovskite-type lanthanum manganite thin films and fine powders using metal acetylacetonate and poly(vinyl alcohol), *J. Am. Ceram. Soc.* 80 (**1997**), 2702–2704

[15] M. Gaudon, C. Laberty-Robert, F. Ansart, P. Stevens, A. Rousset, Preparation and characterization of $La_{1-x}Sr_xMnO_{3+\delta}$ ($0 \le x \le 0.6$) powder by sol-gel processing, *Solid State Sciences*, 4 (**2002**), 125–133

[16] P. Kuttan; J. Jorly; G. N. Madhusudan, S.S. Chandra, L. Ramji, Synthesis of nanocrystalline lanthanum strontium manganite powder by the urea-formaldehyde polymer gel combustion route, http://www.ingentaconnect.com/content/bsc/jace;jsessionid=54t7kd2 r5airk.alexandra" \o "Journal of the American Ceramic Society", 89 (**2006**) 7, 2335–2337

[17] M.B. Kakade, S. Ramanathan, G.K. Dey, D. Das, Processing and Characterisation of Porous Lanthanum Strontium Manganite -Role of Porosity on Electrical Conductivity and Morphology, Advances in applied ceramics, 107 (**2008**) 2, 89–95

[18] A. M. Duprat, P. Alphonse, C. Sarda, A. Rousset, B. Gillot, Non-stoichiometry-activity relationship in perovskite-like manganites, *Mater. Chem. Phys.* 37 (**1994**), 76–81

[19] A. Ghosh, A. K. Sahu, A. K. Gulnar, A. K. Suri, Synthesis and Characterization of Lanthanum Strontium Manganite, *Scripta Materialia*, 52 (**2005**), 1305–1309

[20] J. Sfeir, S. Vaucher, P. Holtappels, U. Vogt, H.-J. Schindler, J. Van herle, E. Suvorova, P. Buffat, D. Perret, N. Xanthopoulos, O. Bucheli, Characterization of perovskite powders for cathode and oxygen membranes made by different synthesis routes, *Journal of the European Ceramic Society*, 25 (**2005**), 1991–1995

[21] R. J. Bell, G. J. Millar, J. Drennan, Influence of synthesis route on the catalytic properties of $La_{1-x}Sr_xMnO_3$, *Solid State Ionics*, 131 (**2000**), 211–220

[22] J. Tanaka, K. Takahashi, Y. Yajima, M. Tsukioka, Lattice constants of monoclinic $(La_{0.8}Ca_{0.2})MnO_3$, *Chemistry Letters*, (**1982**), 1847–1850

[23] A. Chakraborty, P. Choudhury, H. S. Maiti, Electrical conductivity in Sr-substituted lanthanum manganite cathode material prepared by autoignition technique, Proc. 4th Int. Symp. On SOFC, (Ed. M. Dokiya, O. Yamamoto, H. Tagawa, S.C. Singhal), (**1995**), 612–618

[24] N. Q. Minh, T. Takahashi, Science and technology of ceramic fuel cells, Elsevier, The Netherlands, 1995

[25] J. Mizusaki, S. Tsuchiya, K. Waragi, H. Tagawa, Y. Arai, Y. Kuwayama, Simple mathematical model for the electrical conductivity of higly porous ceramics, *J. Am. Ceram. Soc.*, 79 (**1996**) 1, 109–113

[26] L. Kilizendermann, D. Das, D. Bahadur, R. Weiss, H. Nikel, K. Hilpert, Chemical interaction between La-Sr-Mn-Fe-O based perovskites and Yttria stabilized Zirconia, *J. Am. Ceram. Soc.*, 80 (**1997**) 4, 909–914

[27] C. Clausen, C. Bagger, J. B. Bilde-Sorensen, A. Horsewell, Microstructural and microchemical characterization of the interface between $La_{0.85}Sr_{0.15}MnO_3$ and Y_2O_3-stablized ZrO_2, *Solid State Ionics*, 70/71 (**1994**), 59–64

MODELLING THE CHARACTERISTICS OF AN INVERTED MAGNETRON USING NEURAL NETWORKS

MODELIRANJE KARAKTERISTIKE INVERTNEGA MAGNETRONA Z NEVRONSKIMI SISTEMI

Igor Belič

Institute of Metals and Technology, Lepi pot 11, 1000 Ljubljana, Slovenia
igor.belic@imt.si

The inverted magnetron or cold cathode gauge (CCG) is a device used as a vacuum gauge. It is a very robust device, with mostly very positive properties. The problem with its use lies in its nonlinear, temporary, variable characteristic and the fact that the theory of its operation is not thoroughly understood. Neural networks are, therefore, an ideal solution for building a nonlinear characteristics model, based on a set of measured points. Such a model is valid for some certain period of time. When the characteristic of the CCG is altered significantly (due to aging and contamination), the process of recalibration needs to be done, where again neural networks provide a very easy-to-use and robust tool.

In the article the simulation of the CCG characteristics is presented. It is meant to provide sufficiently large sets of data to enable a study of the modelling properties of the used neural networks. The CCG characteristic was split into several segments, each of which was modelled by a separate neural network. The results of the study are presented. The study ended in a practically usable methodology for employing neural networks to calibrate (or recalibrate) the CCGs.

Keywords: inverted magnetron, CCG, modelling, approximation, neural networks, calibration

Invertni magnetron ali merilnik s hladno katodo (CCG) je naprava, ki se uporablja kot grobi merilnik tlaka v vakuumskih sistemih. To so robustne naprave s celo vrsto dobrih lastnosti. Problem praktične uporabe je, da je karakteristika CCG zelo nelinearna, časovno spremenljiva in da teorija delovanja ni povsem znana. Zato so nevronski sistemi idealno orodje za gradnjo nelinearnega modela, ki je zgrajen na množici izmerjenih točk. Tak model je uporaben v nekem časovnem obdobju. Ko se karakteristika CCG preveč spremeni (zaradi staranja in kontaminacije naprave), je treba narediti rekalibracijo. Tudi pri rekalibraciji so nevronski sistemi uporabljeni kot orodje, ki je robustno in enostavno za uporabo.

V prispevku je opisana simulacija karakteristike CCG. Namenjena je generiranju zadostnega števila točk, ki so omogočile študijo lastnosti modeliranja z nevronskimi sistemi. Celotna karakteristika CCG je bila razdeljena na nekaj segmentov, pri čemer je bil vsak segment posebej modeliran s svojim nevronskim sistemom. Predstavljeni so rezultati študije. Rezultat študije je praktično uporabna metodologija modeliranja karakteristike CCG z nevronskimi sistemi, ki jih uporabimo za kalibracijo (rekalibracijo) merilnika.

Ključne besede: invertni magnetron, CCG, modeliranje, aproksimacija, nevronski sistemi, kalibracija

1 INTRODUCTION

The inverted magnetron or cold cathode gauge (CCG) is normally used as a coarse pressure gauge in the range from $1 \cdot 10^{-12}$ to $1 \cdot 10^{-2}$ mbar. During our work the range from $1 \cdot 10^{-9}$ to $1 \cdot 10^{-5}$ mbar was used. (In the field of vacuum phisics the mbar is commonly used. The SI unit is Pa. 1 bar = 10^5 N/m^2 = 10^5 Pa; 1 mbar = 1 hPa)

On the principles of CCG operation, our research group has already published several articles [1,2,3,4,5]. In the scope of this article only a very brief overview of the CCG's operating principles is given.

In the inverted magnetron the electrons are trapped in perpendicular magnetic and electric fields [5]. The electrons are moving on cycloid trajectories around the anode, which is placed inside the discharge cell. The kinetic energy of electrons is high enough to ionize the atoms and molecules of the vacuum chamber's atmosphere inside the magnetron cell. After the collision of the electron with an atom/molecule, the kinetic energy of the electron decreases, therefore it is drawn into a cycloid trajectory closer to the anode. After a series of collisions, the electron reaches the anode and therefore contributes to the anode current. Due to the higher mass/charge ratio, the ions take wider cycloid trajectories than electrons and they hit the cathode. By doing so, new electrons emerge from the cathode surface and they add to the electron cloud within the magnetron cell [6,7]. Some ions are trapped on the cathode surface and therefore they no longer contribute to the chamber's atmosphere. This causes an unwanted pumping effect of the CCG gauge. The gauge itself lowers the pressure inside the vacuum chamber.

Inverted magnetrons are very robust devices. They use very little power for their operation, they have a very high sensitivity, they operate without a hot cathode and they are relatively cheap [8]. Usually, they act as relative pressure gauges used for large vacuum systems, such as accelerators, as well as in vacuum systems where the additional RF pollution caused by the gauge (for example, the hot filament cathode) cannot be tolerated [9,10,11,12].
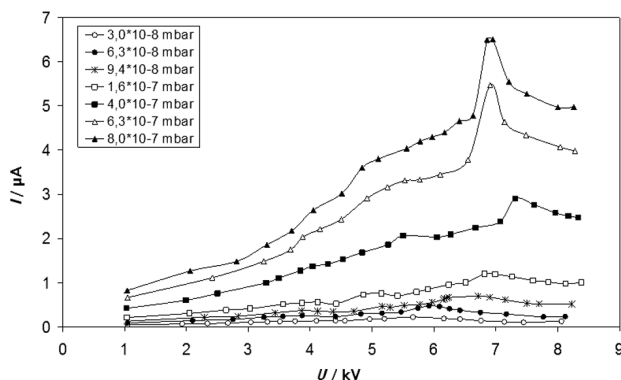
The cold cathode gauges compared to the hot cathode gauges also show a very low level of thermic outgassing, they do not emit the unwanted x-rays, nor do they cause

electron stimulated desorption. The electron cloud is provided solely by the self-sustaining mechanism of the vacuum chamber atmosphere's atoms/molecules ionisation.

Although there are always enough electrons in the rotating field of the CCG the anode current rises with the pressure. The property that makes the use of the inverted magnetron problematic is its non-linear characteristic between the registered ion current and the actual pressure in the vacuum chamber. At very low pressures the device does not start easily and it can take some time to form the spatial charge in the CCG cell. Devices without the starter that provides the initial electron cloud might not start in UHV (ultra-high-vacuum) conditions.

In addition to the many advantages of CCGs, these instruments are restricted in their use by a decreasing measuring accuracy over the operating time [13,14] as the internal electrodes become contaminated. Thus, to guarantee a consistently high measuring accuracy, this gauge type needs to be calibrated regularly after a fixed operating time period. The calibration process can be improved by the use of neural network modelling.

The process of modelling the characteristics of the inverted magnetron (CCG – cold cathode gauge) using the neural networks is presented. The characteristics were obtained on a calibration ultra-high-vacuum system which consists of the test chamber, the extractor gauge, the spinning rotor gauge, and the gas manifold with the precision valve. The magnetron ion current was measured simultaneously with the high-voltage measurements between the cathode and the anode, all at different pressures, that vary form 10^{-9} do 10^{-5} mbar. The working voltage (cathode-anode) was varied in the range from 1.2kV to 9kV. For all measurements, the magnetic field density remained at 1.3T. A very positive attribute of the CCG is its extremely low thermal outgassing values, and it can be used for measurements of low-pressure values suitable for ultra-high-vacuum systems.

An unwanted property of the inverted magnetron is its highly nonlinear dependence between the ion current and the pressure in the vacuum system (**Figure 1**). In some areas the CCG characteristic can also show discontinuities.

The mechanisms of operation of such a complicated device as an inverted magnetron are not understood in detail. Consequently, classical mathematical modelling is not appropriate to cover the analytical needs for devices that serve as measurement equipment.

For the inverted magnetron in the role of a vacuum-system pressure gauge the dependence between the ion current, the operating voltage and the pressure in the vacuum system must be known. In addition, in the process of magnetron calibration, its characteristics must be measured. Usually, the number of measured points is, from the practical point of view, limited. The role of the neural network is to model the characteristic in the whole usable space between the measured points. The complete set of measured points is used as the training set for the multi-layer neural network with the classical error-backpropagation training scheme. The formed model must be able to reconstruct the input–output relationship, where the input consists of the ion current and the working voltage, while the vacuum system pressure represents the output value. The built model makes it possible to use the inverted magnetron as a pressure gauge.

In the CCG's lifetime, its characteristic changes, and therefore it needs to be recalibrated several times. The use of a neural network to model the CCG's characteristic is proposed.

Nonlinear CCG characteristic (I/p) is normally approximated-modelled piecewise using **Equation (1)**.

$$I = k\,p^n \qquad (1)$$

with the sensitivity

$$I/p = k\,p^{(n-1)} \qquad (2)$$

where I represents the ion current, n and k are the constants that are different for the observed part of the CCG characteristic. In the literature [15] the values of n are listed from 1.05 to 2. The constant k depends on the magnetic flux density, the geometry of the discharge chamber and the gases present in the chamber. The constant n depends primarily on the magnetic flux density, the operating voltage and, again, on the geometry of the device [7].

The theory of magnetron operation is not known in such a detail as to enable the theoretical mathematical model to cover the device's operation for measurement purposes [16]. The relationship between the ion current and the pressure above the so-called "magnetron knee" is usually obtained in the logarithm tables of measured values [17,18]. The tables are formed in a time-consuming calibration process. Furthermore, the use of such tables makes operating the magnetron clumsy. The values between those covered in the table are usually calculated

Figure 1: The nonlinear characteristic *I/U* of the magnetron (Measurements were conducted by dr. Alenka Vesel and dr. Miran Mozetič, both from the Josef Stefan Institute, Ljubljana, Slovenia.)
Slika 1: Nelinearna karakteristika *I/U* magnetrona (Meritve sta izvedla dr. Alenka Vesel in dr. Miran Mozetič, oba IJS, Ljubljana, Slovenija)

by linear interpolation, which introduces additional errors into the measurements.

The introduction of neural networks reduces the number of measured points needed for the calibration process. Since the neural network builds the nonlinear CCG characteristic, the linear interpolation is no longer needed and, consequently, any error produced by the linear interpolation is avoided.

The important properties of the inverted magnetron can be summarized in several points:

- The principle of the magnetron's operation is not known in such a detail as to enable a concise mathematical model;
- The CCG characteristic is nonlinear and in some places even discontinued;
- Usually, a very coarse piecewise mathematical model is applied;
- The operation of the CCG as a pressure gauge is stable and repeatable, although due to contamination and aging process it needs recalibrations.
- It is usually used as a coarse relative pressure gauge.

1.1 A testing ground for the neural network modelling

In the process of modelling it is of vital importance to have a reasonably large amount of data to first build the model and second to validate its operation. It is rare to have a situation where there is a large amount of data readily to hand. Therefore, it is very good practice to form some kind of generator that is able to provide the amount of data needed to asses all the necessary aspects of the formed model. The simulated data is intended only to enable a thorough analysis of the modelling process alone, before it can be used on "live" data (**Figure 2**). By no means is the simulation intended to clarify the physical phenomena that take place in the CCG.

The simulation of the inverted magnetron characteristic uses the basic **Equation (1)**, which combines the pressure in the vacuum chamber and the ion current of the inverted magnetron. **Equation (1)** also includes two parameters that depend on the magnetic flux density, the
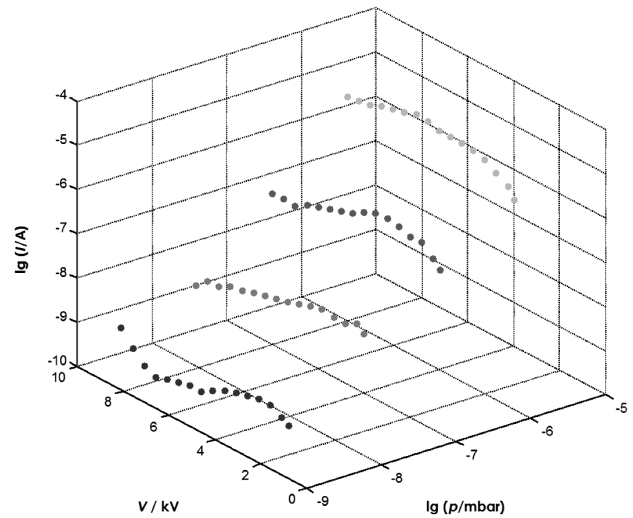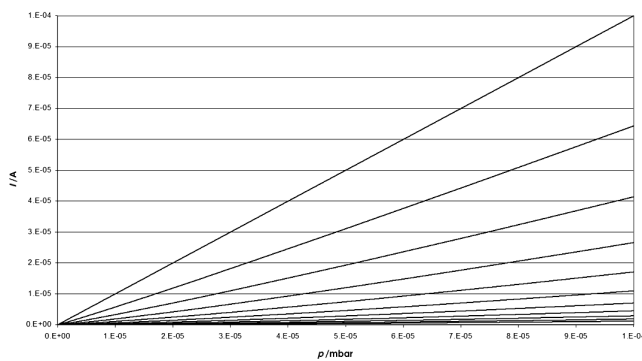
Figure 2: The measured characteristic of the inverted magnetron (log values for *p* and *I*) (Measurements were obtained by dr. Bojan Erjavec, IMT, Ljubljana, Slovenia.). Please note that the operating range of the device spans several decades, which complicates the modelling process.
Slika 2: Izmerjena karakteristika invertnega magnetrona (logaritemske vrednosti) (Meritve je izvedel dr. Bojan Erjavec, IMT). Zaradi merilnega področja, ki obsega področje več dekad, je logaritmiranje nujno, sicer grafičen prikaz ne bi bil smiseln.

operating voltage, the geometry, and the materials used to fabricate the device.

Figure 2 depicts the measured characteristic (***U-p-I***) measured at four different pressure values, with different operating voltages between 2.5 kV and 7.5 kV. Therefore, for each operating voltage we have four different ion-current values for different chamber pressures.

At first we have to assess the values for parameters ***k*** and ***n***. From four different characteristic points, the least-squares method was used to calculate ***k*** and ***n*** at all voltages. The upper part of **Table 1** contains the assessed values that use the measured values of the CCG. These values represent the initial assessment of where the simulated values should be. In the simulated characteristic, a slightly narrower range was used (**Table 1** –
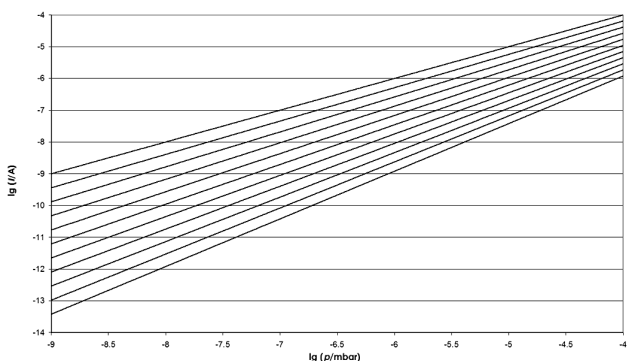
Figure 3: Simulation of the ideal characteristic of the inverted magnetron. Different curves are due to the different operating voltage *U*, with the appropriate parameters *k* and *n*. The right-hand figure is the log 10 of the figure on the left-hand side.
Slika 3: Simulirana idealna karakteristika invertnega magnetrona. Parameter pri različnih krivuljah je delovna napetost *U* s pripadajočima *k* in *n*. Desna slika je desetiški logaritem leve slike.

lower part). The values used to create the simulation are printed in the same table.

Tabela 1: Measured and simulated values for the parameters k and n
Tabela 1: Izračunane in simulirane vrednosti za parametra k in n

MEASURED VALUES		
Operating voltage U/kV	k	n
2.5	O.9130	1.0026
3	1.3866	0.9973
3.5	1.8302	1.0371
4	2.2576	1.0657
4.5	2.7023	1.1448
5	3.0021	1.1127
5.5	3.2945	1.0753
6	3.5140	1.0412
6.5	3.9903	1.0319
7	4.3364	1.0218
7.5	4.9055	1.0398
SIMULATED VALUES		
Operating voltage U/kV	k	n
1	1.0000	1.0000
1.3	1.0500	1.0200
1.6	1.1000	1.0400
1.9	1.1500	1.0600
2.2	1.2000	1.0800
2.5	1.2500	1.1000
2.8	1.3000	1.1200
3.1	1.3500	1.1400
3.4	1.4000	1.1600
3.7	1.4500	1.1800
4	1.5000	1.2000

For the selected values of k and n (lower part of **Table 1**), the ideal characteristic U-p-I is generated. This follows the logarithm (base 10) of the pressure p and the ion current I, while keeping the operating voltage constant (**Figure 3**).

It is not our goal to simulate the ideal characteristic, in fact we need the characteristic that includes the

departures from such idealizations. The ideal characteristic is therefore modified in a few steps. All the modifications are made on data in log space. The first modification changes the value of the ion current versus pressure (**Figure 4**). The modification follows **Equation (3)**.

$$\lg (I_2) = \lg (I_1) + \sin (\pi(\lg(p) + 7)/4) \tag{3}$$

Here, I_1 represents the ion current prior to the modification, while the current I_2 represents the value after it.

The second modification bends the CCG characteristic with the regard to the operating voltage – **Equation (4)**.

$$\lg (I_3) = \lg (I_2) + \sin (\pi(U - 1)/3) \tag{4}$$

The current I_2 is the value prior to, and I_3 is after, the second modification (**Figure 5**).

The third modification introduces random fluctuations to the so-far modified characteristic. The modification follows equation (5).

$$\lg (I_4) = \lg (I_3) + m\ Rand() \tag{5}$$

As in previous modifications, the current I_3 holds the value prior to, and the I_4 after, the modification. The generator of random numbers is denoted by *Rand().* It generates pseudo random numbers with values from –1 to +1, while the parameter *m* sets the magnitude of the influence of the randomization process. The result of the third modification is shown in **Figure 6**.

The three modifications form the simulated CCG characteristic, which is presented in 3D in **Figure 7**.

The data of the simulated CCG characteristic is gathered in **Table 2**.

The same data can also be presented in the parameterized graph shown in **Figure 8**. The similarity between the characteristic from **Figure 1** and **Figure 8** is obvious.

The similarity between the actual CCG characteristic and its simulated counterpart is close enough to enable a study of the modelling properties of the neural network.
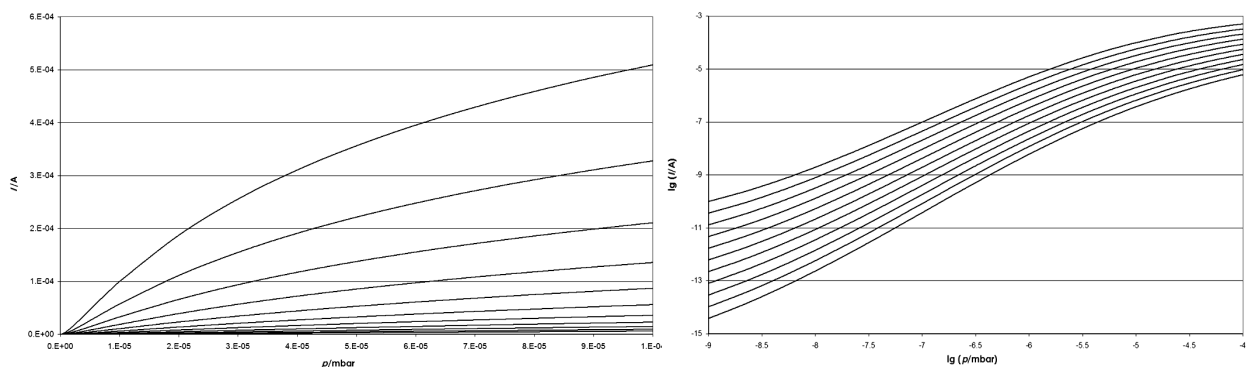
Figure 4: The first modification of the ideal CCG characteristic – it bends the characteristic with regard to the pressure. Different curves have a different operating voltage U, and the parameters k and n. The right-hand figure is the log 10 of the figure on the left-hand side.
Slika 4: Prva korekcija idealne karakteristike – ukrivljenost glede na tlak. Parameter pri različnih krivuljah je delovna napetost U s pripadajočima k in n. Desna slika je desetiški logaritem leve slike.
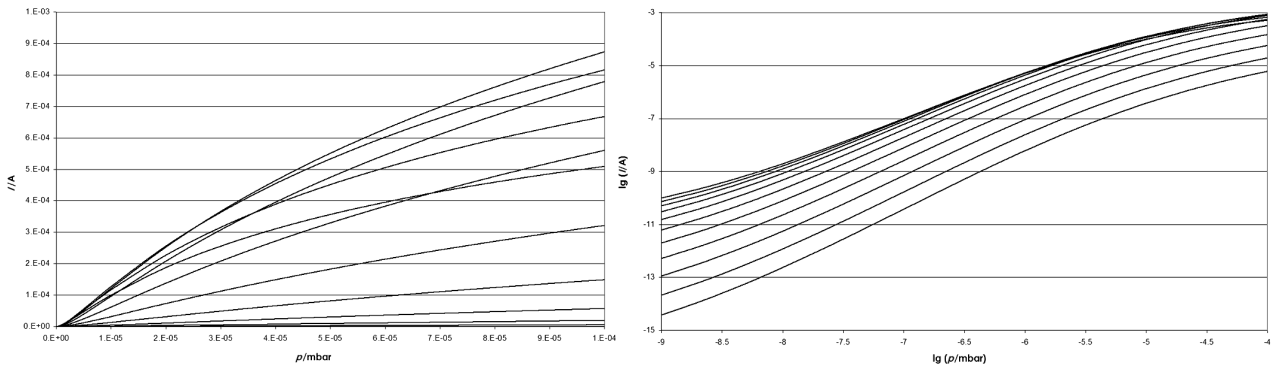
Figure 5 : The second modification – the characteristic is bent with regard to the operating voltage. Different curves have a different operating voltage *U*, and the parameters k and n. The right-hand figure is the log 10 of the figure on the left-hand side.
Slika 5: Druga korekcija karakteristike – ukrivljenost glede na napetost. Parameter pri različnih krivuljah je delovna napetost U s pripadajočima *k* in *n*. Desna slika je desetiški logaritem leve slike.
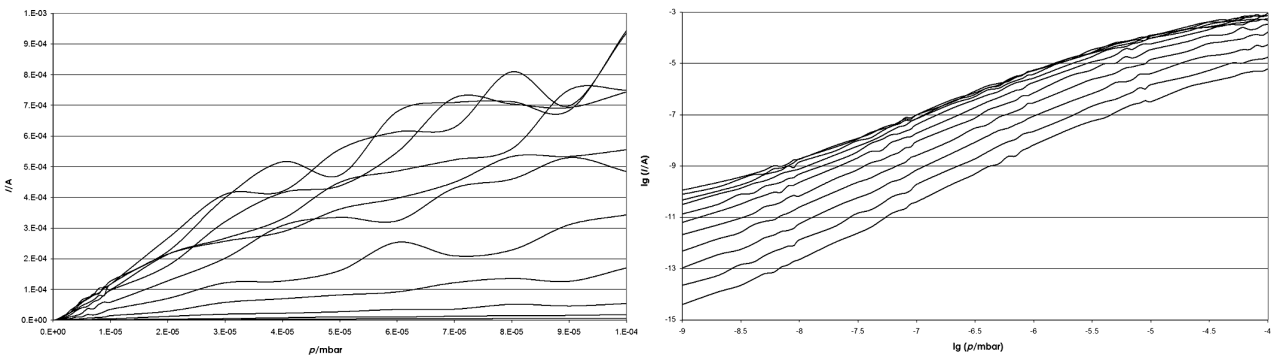
Figure 6 : The third modification – the randomization process. Different curves have a different operating voltage *U*, and the parameters *k* and *n*. The right-hand figure is the log 10 of the figure on the left-hand side.
Slika 6: Tretja korekcija karakteristike – naključna sprememba. Parameter pri različnih krivuljah je delovna napetost *U* s pripadajočima *k* in *n*. Desna slika je desetiški logaritem leve slike.

1.2 The neural-network modelling of the CCG characteristic

The calibration process for the inverted magnetron is a time-consuming task. The neural-network modelling of the characteristic must provide a reduction of the required number of calibration points and it should model the characteristic in the whole usable space. The central problem of modelling the CCG is the fact that its operation spans a large range, which is true for the current (10^{-11} A to 10^{-4} A) as well as for the pressure (10^{-9} to 10^{-6} mbar).
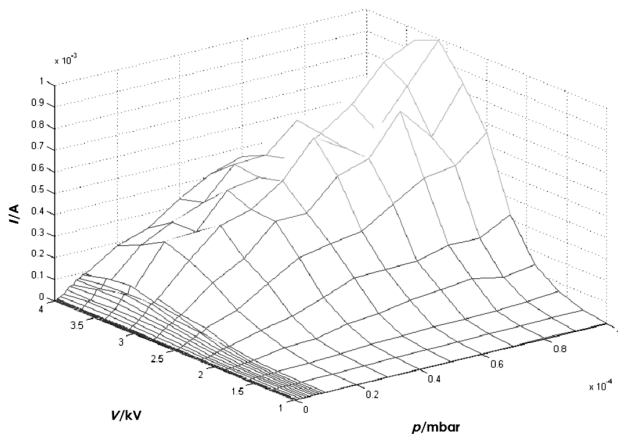
Figure 7: An example of the simulated characteristic of the magnetron
Slika 7: Primer simulirane karakteristike magnetrona
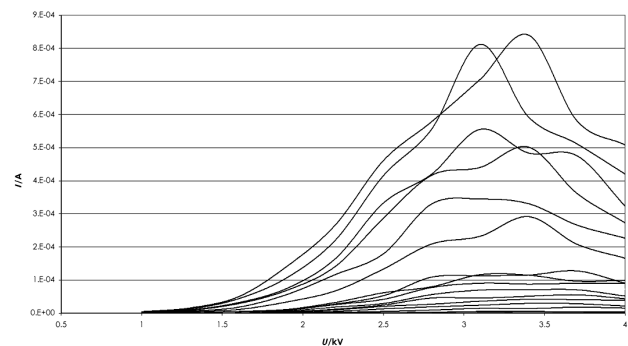
Figure 8: The parameterized view of the simulated characteristic of the CCG. The pressure *p* is the parameter for the presented curves. The higher curve is obtained at higher pressure.
Slika 8: Primer parametriziranega prikaza simulirane karakteristike invertnega magnetrona. Parameter je tlak v vakuumski komori – višja krivulja je dobljena pri višjem tlaku.

Table 2: The simulated CCG characteristic. The ion current of the inverted magnetron I/A in relation to the pressure p/mbar, and the operating voltage U/kV. The CCG characteristic is divided into 10 segments for further processing. The central part of the table represents the ion current I/A. The segments overlapping areas are shaded in gray.
Tabela 2: Simulirana karakteristika; katodni tok invertnega magnetrona I/A v odvisnosti od tlaka p/mbar in delovne napetosti U/kV. Celotna karakteristika je zaradi potreb v nadaljevanju razdeljena na 10 segmentov. Vse vrednosti v osrednjem delu tabele so katodni tok I/A. Sivo obarvana polja vsebujejo podatke, kjer se segmenti glede na vrednost tlaka p prekrivajo.

| U/kV	4	3.7	3.4	3.1	2.8	2.5	2.2	1.9	1.6	1.3	1
p/mbar						I/A					
1.00E-09	1.00E-10	7.37E-11	5.07E-11	3.05E-11	1.53E-11	6.19E-12	2.00E-12	5.20E-13	1.13E-13	2.14E-14	3.79E-15
2.00E-09	2.13E-10	1.63E-10	1.16E-10	7.22E-11	3.75E-11	1.57E-11	5.24E-12	1.41E-12	3.17E-13	6.24E-14	1.14E-14
3.00E-09	3.52E-10	2.74E-10	1.99E-10	1.27E-10	6.71E-11	2.87E-11	9.77E-12	2.69E-12	6.16E-13	1.24E-13	2.31E-14
4.00E-09	5.15E-10	4.07E-10	3.00E-10	1.93E-10	1.04E-10	4.51E-11	1.56E-11	4.35E-12	1.01E-12	2.06E-13	3.91E-14
5.00E-09	7.01E-10	5.60E-10	4.17E-10	2.72E-10	1.48E-10	6.49E-11	2.27E-11	6.40E-12	1.51E-12	3.10E-13	5.95E-14
6.00E-09	9.10E-10	7.34E-10	5.52E-10	3.63E-10	1.99E-10	8.81E-11	3.11E-11	8.86E-12	2.10E-12	4.37E-13	8.46E-14
7.00E-09	1.14E-09	9.27E-10	7.03E-10	4.66E-10	2.58E-10	1.15E-10	4.09E-11	1.17E-11	2.80E-12	5.87E-13	1.15E-13
8.00E-09	1.39E-09	1.14E-09	8.70E-10	5.81E-10	3.23E-10	1.45E-10	5.19E-11	1.50E-11	3.61E-12	7.61E-13	1.50E-13
9.00E-09	1.67E-09	1.37E-09	1.05E-09	7.07E-10	3.96E-10	1.79E-10	6.44E-11	1.87E-11	4.53E-12	9.60E-13	1.90E-13
1.00E-08	1.96E-09	1.62E-09	1.25E-09	8.46E-10	4.76E-10	2.16E-10	7.82E-11	2.28E-11	5.56E-12	1.19E-12	2.36E-13
2.00E-08	6.01E-09	5.15E-09	4.11E-09	2.88E-09	1.67E-09	7.87E-10	2.95E-10	8.92E-11	2.25E-11	4.96E-12	1.02E-12
3.00E-08	1.20E-08	1.05E-08	8.52E-09	6.08E-09	3.61E-09	1.73E-09	6.63E-10	2.05E-10	5.26E-11	1.18E-11	2.49E-12
4.00E-08	1.97E-08	1.75E-08	1.44E-08	1.05E-08	6.30E-09	3.07E-09	1.19E-09	3.73E-10	9.72E-11	2.22E-11	4.73E-12
5.00E-08	2.92E-08	2.61E-08	2.19E-08	1.60E-08	9.75E-09	4.80E-09	1.88E-09	5.96E-10	1.57E-10	3.63E-11	7.82E-12
6.00E-08	4.03E-08	3.64E-08	3.07E-08	2.27E-08	1.40E-08	6.93E-09	2.74E-09	8.77E-10	2.34E-10	5.44E-11	1.18E-11
7.00E-08	5.29E-08	4.83E-08	4.10E-08	3.05E-08	1.89E-08	9.47E-09	3.78E-09	1.22E-09	3.27E-10	7.67E-11	1.68E-11
8.00E-08	6.72E-08	6.16E-08	5.27E-08	3.95E-08	2.47E-08	1.24E-08	4.99E-09	1.62E-09	4.37E-10	1.03E-10	2.28E-11
9.00E-08	8.29E-08	7.65E-08	6.58E-08	4.96E-08	3.12E-08	1.58E-08	6.38E-09	2.08E-09	5.65E-10	1.34E-10	2.98E-11
1.00E-07	1.00E-07	9.28E-08	8.03E-08	6.09E-08	3.84E-08	1.96E-08	7.95E-09	2.61E-09	7.12E-10	1.70E-10	3.79E-11
2.00E-07	3.43E-07	3.30E-07	2.95E-07	2.32E-07	1.51E-07	7.98E-08	3.36E-08	1.14E-08	3.22E-09	7.97E-10	1.84E-10
3.00E-07	6.97E-07	6.83E-07	6.25E-07	5.00E-07	3.33E-07	1.79E-07	7.70E-08	2.67E-08	7.70E-09	1.94E-09	4.58E-10
4.00E-07	1.14E-06	1.14E-06	1.05E-06	8.55E-07	5.79E-07	3.16E-07	1.38E-07	4.83E-08	1.41E-08	3.63E-09	8.66E-10
5.00E-07	1.66E-06	1.67E-06	1.57E-06	1.29E-06	8.81E-07	4.86E-07	2.14E-07	7.61E-08	2.25E-08	5.84E-09	1.41E-09
6.00E-07	2.25E-06	2.28E-06	2.16E-06	1.79E-06	1.24E-06	6.88E-07	3.06E-07	1.10E-07	3.28E-08	8.57E-09	2.09E-09
7.00E-07	2.89E-06	2.96E-06	2.82E-06	2.36E-06	1.64E-06	9.20E-07	4.12E-07	1.49E-07	4.48E-08	1.18E-08	2.90E-09
8.00E-07	3.58E-06	3.69E-06	3.54E-06	2.98E-06	2.09E-06	1.18E-06	5.32E-07	1.93E-07	5.86E-08	1.55E-08	3.85E-09
9.00E-07	4.32E-06	4.48E-06	4.32E-06	3.66E-06	2.58E-06	1.46E-06	6.64E-07	2.43E-07	7.40E-08	1.98E-08	4.92E-09
1.00E-06	5.09E-06	5.31E-06	5.15E-06	4.38E-06	3.10E-06	1.77E-06	8.08E-07	2.97E-07	9.11E-08	2.44E-08	6.11E-09
2.00E-06	1.43E-05	1.54E-05	1.55E-05	1.36E-05	9.97E-06	5.90E-06	2.78E-06	1.06E-06	3.36E-07	9.34E-08	2.42E-08
3.00E-06	2.48E-05	2.73E-05	2.80E-05	2.51E-05	1.88E-05	1.13E-05	5.46E-06	2.12E-06	6.87E-07	1.95E-07	5.15E-08
4.00E-06	3.58E-05	3.99E-05	4.16E-05	3.79E-05	2.87E-05	1.76E-05	8.60E-06	3.39E-06	1.11E-06	3.20E-07	8.59E-08
5.00E-06	4.69E-05	5.29E-05	5.57E-05	5.13E-05	3.94E-05	2.44E-05	1.21E-05	4.81E-06	1.60E-06	4.64E-07	1.26E-07
6.00E-06	5.79E-05	6.60E-05	7.01E-05	6.52E-05	5.05E-05	3.15E-05	1.57E-05	6.33E-06	2.12E-06	6.22E-07	1.70E-07
7.00E-06	6.88E-05	7.90E-05	8.45E-05	7.92E-05	6.18E-05	3.89E-05	1.96E-05	7.93E-06	2.68E-06	7.92E-07	2.18E-07
8.00E-06	7.95E-05	9.18E-05	9.89E-05	9.33E-05	7.33E-05	4.65E-05	2.35E-05	9.60E-06	3.26E-06	9.72E-07	2.70E-07
9.00E-06	8.99E-05	1.04E-04	1.13E-04	1.07E-04	8.49E-05	5.41E-05	2.76E-05	1.13E-05	3.87E-06	1.16E-06	3.24E-07
1.00E-05	1.00E-04	1.17E-04	1.27E-04	1.21E-04	9.65E-05	6.19E-05	3.16E-05	1.31E-05	4.49E-06	1.35E-06	3.79E-07
2.00E-05	1.88E-04	2.27E-04	2.56E-04	2.53E-04	2.08E-04	1.38E-04	7.31E-05	3.12E-05	1.11E-05	3.46E-06	1.01E-06
3.00E-05	2.56E-04	3.16E-04	3.63E-04	3.66E-04	3.07E-04	2.08E-04	1.12E-04	4.91E-05	1.78E-05	5.67E-06	1.68E-06
4.00E-05	3.11E-04	3.89E-04	4.54E-04	4.64E-04	3.96E-04	2.72E-04	1.49E-04	6.59E-05	2.43E-05	7.84E-06	2.36E-06
5.00E-05	3.56E-04	4.51E-04	5.33E-04	5.51E-04	4.75E-04	3.30E-04	1.83E-04	8.18E-05	3.05E-05	9.94E-06	3.02E-06
6.00E-05	3.95E-04	5.05E-04	6.02E-04	6.28E-04	5.46E-04	3.83E-04	2.14E-04	9.67E-05	3.64E-05	1.20E-05	3.68E-06
7.00E-05	4.29E-04	5.53E-04	6.64E-04	6.98E-04	6.11E-04	4.32E-04	2.44E-04	1.11E-04	4.20E-05	1.39E-05	4.31E-06
8.00E-05	4.59E-04	5.95E-04	7.20E-04	7.62E-04	6.71E-04	4.78E-04	2.71E-04	1.24E-04	4.74E-05	1.58E-05	4.93E-06
9.00E-05	4.86E-04	6.33E-04	7.70E-04	8.20E-04	7.27E-04	5.20E-04	2.97E-04	1.37E-04	5.25E-05	1.76E-05	5.53E-06
1.00E-04	5.09E-04	6.68E-04	8.16E-04	8.74E-04	7.79E-04	5.60E-04	3.22E-04	1.49E-04	5.75E-05	1.94E-05	6.11E-06

The neural-network approximation requires that both the input and the output values are mapped in the range from 0 to 1 (or in some versions from –1 to +1). The main problem of mapping is that the small values are modelled with a very low precision. The problem is addressed in detail in [19]. Basically, we have two strategies to deal with the problem, one is to transform the data in the log space, and the other is to split the characteristic into the appropriate number of segments [5,20].

The solution to the problem of modelling the large data range with the neural networks can not be found in the literature. In such cases it is the usual approach to use the log transformation of the whole data space and then execute the modelling in log space. Nowadays, computers are very fast, they provide very large memory capacities, and so there is no difficulty in addressing the problem from another perspective. Instead of performing the log transformation, the data space can be segmented
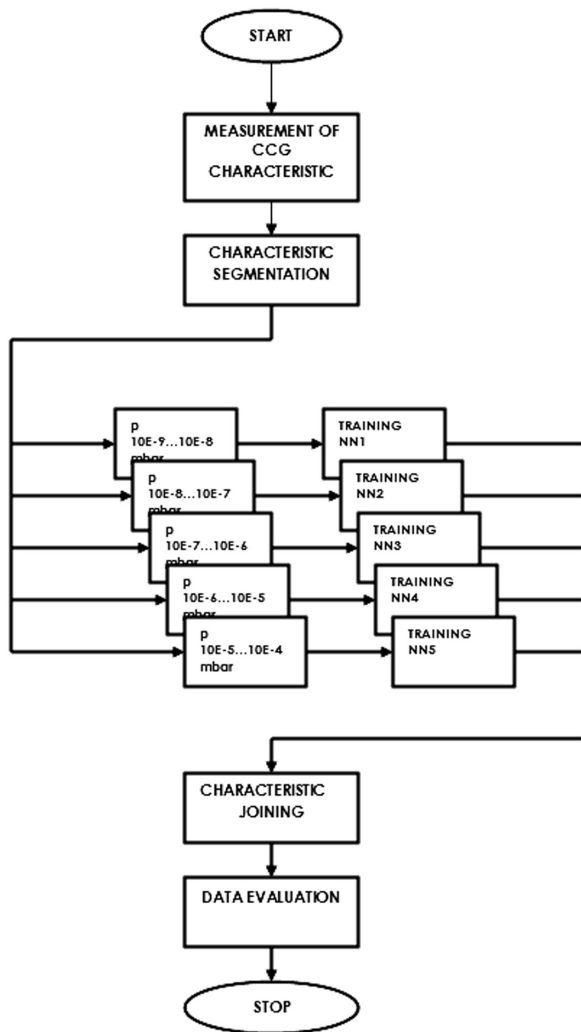
Figure 9: The segmentation strategy – the complete data space is segmented into several sub-spaces. Each segment is then modelled separately

Slika 9: Strategija segmentacije – delitve področja na več podpodročij. Vsak segment je modeliran posebej

into the convenient sub-spaces and the modelling process should be executed for each segment separately (**Figure 9**). Thus, separate models are created for each separate segment. It is of vital importance that the data is segmented in such a way that the segments are not too wide, and that we have enough data for each separate segment to do the modelling.

The segmentation theory shows the following important details:

- Both the input and output spaces are divided into several sub-spaces called segments. Each segment has its own multiplication constant to map the area close to the 0, 1 interval.
- The neural-network training tolerance is valid for each segment only.
- When all the models are formed, the process of merging them again into the single characteristic has

to be accomplished. The modelling error is again valid for each segment separately.

The actual output value of the model y_a is calculated from the output value y of the neural network using the equation

$$y_a = k_i y \tag{6}$$

where k_i denotes the multiplication constant of the i-th segment, y_a is the scaled value of the value y produced by the neural-network model. The error produced by the model of the i-th segment can be calculated as it stands in **Equation (7)**.

$$\Delta y_a = \sum_{i=1}^{n} \frac{\partial F}{\partial y_i} \Delta y_i \Rightarrow \Delta y_a = k_i \Delta y \; ; \; k_i \ll 1 \tag{7}$$

where the function F represents the modelled function and the meaning of the other symbols is the same as in **Equation (6)**.

We have found that reasonably good modelling results can be acheived if at least five data points are available for each segment (it is true for our CCG example). The division of the modelled space depends on various parameters. The most important parameters are the shape of the modelled function and the admissible relative error that the model should fulfil. **Table 2** shows the segmentation of the CCG characteristic into 10 segments. The segments should overlap in order to allow the merging of the segments when the separate segments are modelled. The overlapping region is shown with the gray background (**Table 2**). Neural networks (due to the pre-set training criteria) perform well at higher values, so when two segments are to be merged, one segment has locally high values, while the other is to be joined with the locally low values. During the merging process it is more likely that the data from the segment that is to be merged with the locally high values
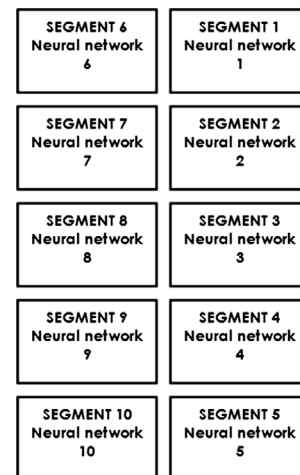
Figure 10: The CCG characteristic has been split into 10 segments. Each segment is modelled on its own – a separate neural network.

Slika 10: Celotna karakteristika invertnega magnetrona je razdeljena na 10 segmentov, vsak segment modelira svoj nevronski sistem.

are more accurately modelled, and some kind of weighting (linear, nonlinear, etc.) should be used.

2 EXPERIMENTAL

Table 2 holds the data of the CCG characteristic, which has been divided into 10 segments. **Figure 10** graphically represents the segmenting process.

The segments were formed in such a way as to ensure that for each segment the ion current I covers as little area as possible. The main idea is that each segment should cover such data space to ensure that the model will produce results with acceptable errors.

Table 3: The data space covered by the separate segments
Tabela 3: Segmenti karakteristike invertnega magnetrona in področja, ki jih posamezni segmenti obsegajo

Segment	p/mbar	I/A
1	1.00E-09 to 6.00E-09	3.79E-15 to 8.86E-12
2	6.00E-09 to 5.00E-08	8.46E-14 to 5.96E-10
3	5.00E-08 to 4.00E-07	7.82E-12 to 4.83E-08
4	4.00E-07 to 4.00E-06	8.66E-10 to 3.39E-06
5	4.00E-06 to 1.00E-04	8.59E-08 to 1.49E-04
6	1.00E-09 to 6.00E-09	5.20E-13 to 9.10E-10
7	6.00E-09 to 5.00E-08	8.86E-12 to 2.92E-08
8	5.00E-08 to 4.00E-07	5.96E-10 to 1.14E-06
9	4.00E-07 to 4.00E-06	4.83E-08 to 4.16E-05
10	4.00E-06 to 1.00E-04	3.39E-06 to 8.74E-04

Table 3 shows the chosen segments and the area coverage for the pressure p as well as for the CCG ion current I. A brief inspection of the segments reveals that some segments still cover an area that spans well over

two decades. It is a necessary trade off since the introduction of even more segments would require more data points, which does not represent the problem in the simulated environment, but for the real CCG calibration it can pose a problem. For testing purposes a 5% training tolerance was selected.

2.1 The testing environment

In the experimental work we studied the modelling capabilities of neural networks, while at the same time we were seeking the neural-network architecture that would show the best modelling properties for the given problem. The approximation theory for use with the neural networks was corrected and published [20]. In the same publication, the concept of the neural-network training stability was introduced. The training stability deals with the variability of various possible neural-network models and sets the boundary where all possible models (obtained with different configurations) give their results.

The testing of various neural-network architectures was organised in an orderly fashion (**Table 4**), where the set of numbers represents the number of artificial neural cells in the appropriate layer. For clarification please refer to [20]. For example, the notation 2 10 20 1 means that the input layer consists of 2 neurons, the first hidden layer of 10 neurons, the second hidden layer of 20 neurons, and finally the output layer contains 1 neuron. Since the experiment took quite some time to complete, it was necessary to develop a system that controls the experiments and in the case of power failure resumes with work where it has been interrupted. The log file was

Table 4: The organisation of the different neural-network configurations included in the experiment
Tabela 4: Seznam preizkušenih konfiguracij nevronskih sistemov

	CONFIGURATION		CONFIGURATION		CONFIGURATION		CONFIGURATION
1	2 5 5 1	21	2 5 10 5 1	41	2 10 15 5 1	61	2 15 20 5 1
2	2 5 10 1	22	2 5 10 10 1	42	2 10 15 10 1	62	2 15 20 10 1
3	2 5 15 1	23	2 5 10 15 1	43	2 10 15 15 1	63	2 15 20 15 1
4	2 5 20 1	24	2 5 10 20 1	44	2 10 15 20 1	64	2 15 20 20 1
5	2 10 5 1	25	2 5 15 5 1	45	2 10 20 5 1	65	2 20 5 5 1
6	2 10 10 1	26	2 5 15 10 1	46	2 10 20 10 1	66	2 20 5 10 1
7	2 10 15 1	27	2 5 15 15 1	47	2 10 20 15 1	67	2 20 5 15 1
8	2 10 20 1	28	2 5 15 20 1	48	2 10 20 20 1	68	2 20 5 20 1
9	2 15 5 1	29	2 5 20 5 1	49	2 15 5 5 1	69	2 20 10 5 1
10	2 15 10 1	30	2 5 20 10 1	50	2 15 5 10 1	70	2 20 10 10 1
11	2 15 15 1	31	2 5 20 15 1	51	2 15 5 15 1	71	2 20 10 15 1
12	2 15 20 1	32	2 5 20 20 1	52	2 15 5 20 1	72	2 20 10 20 1
13	2 20 5 1	33	2 10 5 5 1	53	2 15 10 5 1	73	2 20 15 5 1
14	2 20 10 1	34	2 10 5 10 1	54	2 15 10 10 1	74	2 20 15 10 1
15	2 20 15 1	35	2 10 5 15 1	55	2 15 10 15 1	75	2 20 15 15 1
16	2 20 20 1	36	2 10 5 20 1	56	2 15 10 20 1	76	2 20 15 20 1
17	2 5 5 5 1	37	2 10 10 5 1	57	2 15 15 5 1	77	2 20 20 5 1
18	2 5 5 10 1	38	2 10 10 10 1	58	2 15 15 10 1	78	2 20 20 10 1
19	2 5 5 15 1	39	2 10 10 15 1	59	2 15 15 15 1	79	2 20 20 15 1
20	2 5 5 20 1	40	2 10 10 20 1	60	2 15 15 20 1	80	2 20 20 20 1
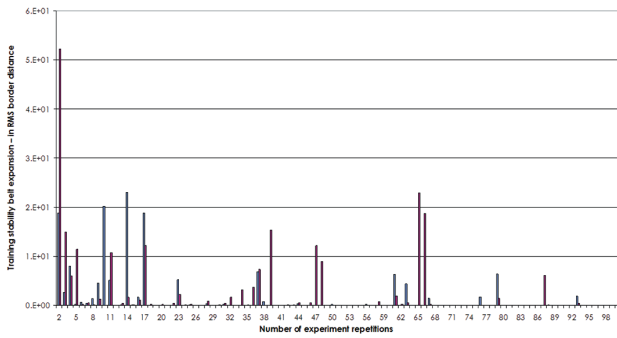
Figure 11: The formation of the training stability belt – the configuration 2 10 10 10 1, segment 3
Slika 11: Formiranje pasu stabilnosti učenja – primer konfiguracije 2 10 10 10 1, segment 3
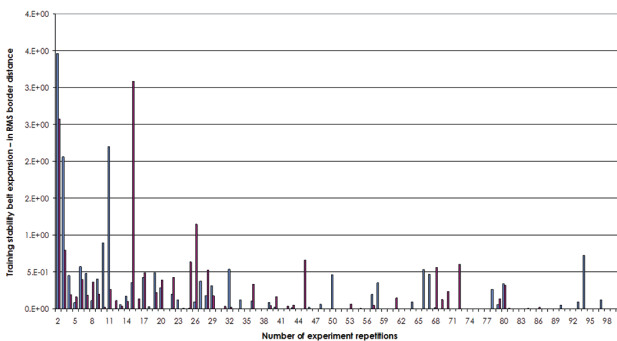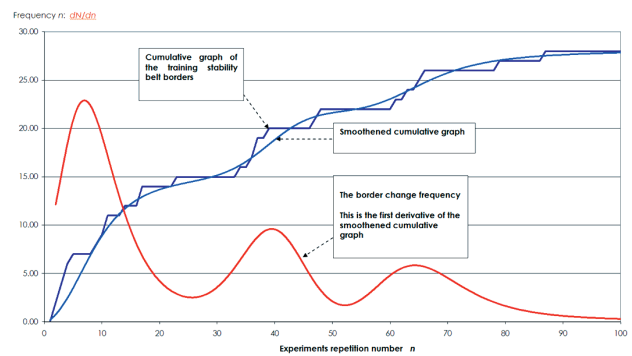

Figure 12: The formation of the training stability belt – the configuration 2 10 20 15 1, segment 6
Slika 12: Formiranje pasu stabilnosti učenja – primer konfiguracije 2 10 20 15 1, segment 6

Figure 13: The formation dynamics of the neural network training stability belt – configuration 2 10 10 10 1, segment 3. From the graph we can conclude that after the 90th repetition of the experiment, the training stability belt does not change significantly.
Slika 13: Dinamika spreminjanja pasu stabilnosti učenja – konfiguracija 2 10 10 10 1, segment 3 Iz grafa lahko ocenimo, da se po 90. ponovitvi učenja pas stabilnosti učenja ne spreminja več bistveno.

Figure 14: The formation dynamics of the neural network training stability belt – configuration 2 10 20 15 1, segment 6. Again, we can conclude that after the 90th repetition of the experiment, the training stability belt does not change significantly.
Slika 14: Dinamika spreminjanja pasu stabilnosti učenja – konfiguracija 2 10 20 15 1, segment 6. Tudi iz tega grafa lahko ocenimo, da se po 90. ponovitvi učenja pas stabilnosti učenja ne spreminja več bistveno.

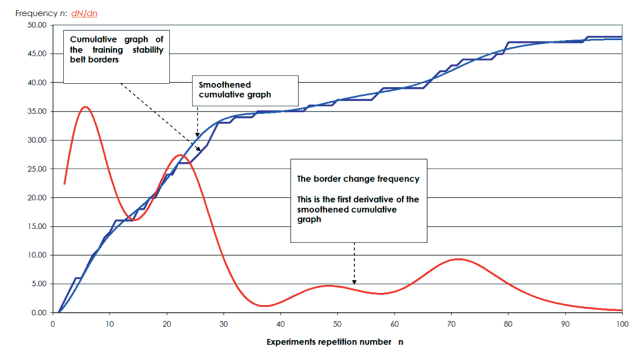created where all the events relating to the experiment were stored.

The directory/file structure was organised to store the experimental data. Each directory holds the data on one neural-network configuration (80 directories). In each directory there are 10 files: one for each segment. For each segment and for each neural-network configuration the different neural cell connection weights were randomly generated and the network was trained. To obtain the training stability belt, 100 different weight sets were probed, meaning that 100 randomly different (in the sense of connection weights) neural networks were generated and trained. The gathered data from 100 separate experiments is stored in a file. The complete experiment is therefore saved in 800 files.

All the generated neural networks were trained with equal parameters that control the behaviour of the neural-network training process. These parameters are as follows: the learning rate (0.7), the momentum (0.5), and the training tolerance (0.1). The training process is stopped when the training tolerance is reached for all the training points. Another limitation was active due to the possibility that the training process does not reach the preset training tolerance. In such cases the training is

stopped, another set of weights is generated and the training is repeated.

2.2 The formation of training stability belt

Before the experiment commences, it is necessary to assess the number of necessary repetitions of the training processes that will give the information on the width of the training stability belt. Two configurations were used for the assessment: 2 10 10 10 1 – 3rd segment (**Figure 11**) and 2 10 20 15 1 – 6th segment (**Figure 12**). The dynamics of the training stability belt was assessed, and it was found that for the configuration 2 10 10 10 1 (**Figure 13**) after the 90th repetition the training stability belt remains stable. For the configuration 2 10 20 15 1 (**Figure 14**) the case is almost the same. Therefore, the number of training repetitions needed to form the training stability belt was set to 100.
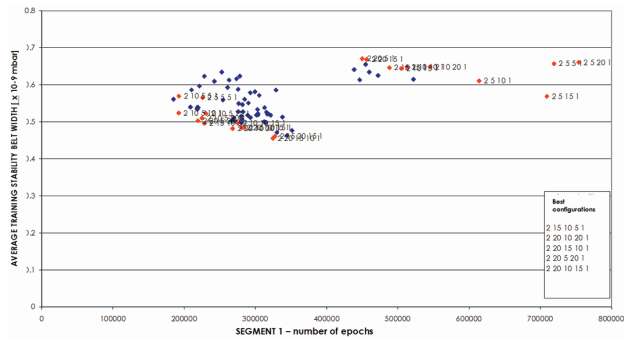
Figure 15: Segment 1. $p_{max}/p_{min} = 6.00$; $I_{max}/I_{min} = 2337.73$; p – 1.00E-09 to 6.00E-09 mbar; I – 3.79E-15 to 8.86E-12 A
Slika 15: Segment 1. $p_{max}/p_{min} = 6.00$; $I_{max}/I_{min} = 2337.73$; p – 1.00E-09 do 6.00E-09 mbar; I – 3.79E-15 do 8.86E-12 A

Table 5: The data on modelling segment 1
Tabela 5: Podatki modeliranju 1. segmenta karakteristike

| The analysis of models	Number of epochs	Training stability belt width ($\cdot 10^{-9}$)
Average	325130	0.55578
Minimum	184900	0.45526
Configuration	2 15 5 5 1	2 20 15 10 1
Maximum	753820	0.67061
Configuration	2 5 20 1	2 20 5 1
Standard deviation	120651.7	0.05773

3 RESULTS AND DISCUSSION – THE COMPARISON OF THE NEURAL-NETWORK CHARACTERISTICS

We are searching for the configuration of the neural network that would give the best results in terms of how fast it is capable of learning the function and, on the other hand, that it is capable of forming the model that produces the narrowest training stability belt (the modelled data is as close as possible to the original). The result of the analysis of the performance of different neural networks modelling one of the ten segments is shown in **Figure 15**. Each point on the graph represents one configuration. On the x axis the average number of epochs needed to train the network is presented, while on the y axis there is the average width of the training stability belt expressed in mbar. For the segment 1, the ratio between the highest and the lowest value of pressure p_{max}/p_{min} is 6.0; the current ratio $I_{max}/I_{min} = 2337.73$. On average, the neural networks needed 325130 epochs to satisfy the training tolerance. The trained models give, on average, a training stability belt width of $5.5 \cdot 10^{-10}$ mbar. The minimum value for the number of epochs is 184900, and it is reached for the configuration 2 15 5 5 1. The lowest value for the training stability belt width is $4.5 \cdot 10^{-10}$ mbar, which is obtained for the configuration 2 20 15 10 1. On the other hand, the worst results were obtained with the configurations 2 5 20 1 (753820 epochs) and 2 20 5 1 (training stability belt width $6.7 \cdot 10^{-10}$ mbar). The
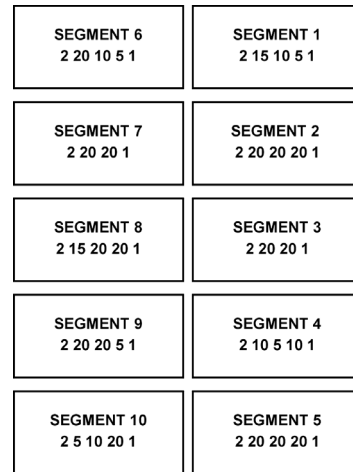
Figure 16: The best configurations to model the segmented characteristic of the CCG
Slika 16: Najugodnejše konfiguracije nevronskih sistemov za posamezne segmente

calculated standard deviation for the number of required epochs and for the segment 1 is 120651.7, while for the training stability belt width it is $5.7 \cdot 10^{-11}$ mbar. The neural-network configurations that show the best results for both the number of required epochs and the training stability belt width for segment 1 are: 2 15 10 5 1; 2 20 10 20 1; 2 20 15 10 1 etc. The red points in **Figure 15** represent the configurations that show the best modelling capabilities, as well as those with the poorest results.

Such assessments were made for all 10 segments. The analysis gives the neural-network configurations that model each separate CCG characteristic segment as well as possible (**Figure 16**).

From the analysis we can conclude that there is no obvious rule that would point to the concrete architecture of the neural network with the narrowest training stability belt and, at the same time, with the fastest learning. The most favourable configuration always depends on the nature of the modelled dependence. **Table 6** summarizes the most important data on the modelling properties of the neural networks for the separate CCG characteristic segments.

The ratio between the highest and the lowest number of required epochs for all the experiments regardless of the configuration was 15.6, and the ratio between the highest and the lowest value for the training stability belt width was 7.1.

For the study of the segmentation strategy during the CCG characteristic modelling, 80 000 models were formed and 9 720 484 000 epochs were used.

4 CONCLUSION

In the presented study neural networks were used as the modelling tool for the nonlinear CCG characteristic. For building up the CCG model a reasonable amount of measured data must be available, which is to be used as

Table 6: The modelling of the CCG characteristic segments – the data analysis
Tabela 6 Modeliranje segmentov karakteristike invertnega magnetrona – analiza poskusov

Segment no.	No. of epochs	Training stability belt width	No. of epochs	NN configuration	No. of epochs	NN configuration	Training stability belt width	NN configuration
	Average	Average	min.		max.		min.	
1	325130	0.55578	184900	2 15 5 5 1	753820	2 5 20 1	0.45526	2 20 15 10 1
2	64178	2.84227	46430	2 5 15 1	146450	2 5 5 1	2.05883	2 20 20 20 1
3	87066	1.71938	56560	2 10 5 1	146420	2 5 5 1	1.27799	2 15 10 5 1
4	352009	1.99775	324390	2 5 5 20 1	482020	2 5 20 1	1.33548	2 15 10 1
5	27128	3.38247	8770	2 10 20 5 1	137350	2 5 20 1	1.54748	2 20 20 20 1
6	286188	0.25606	175580	2 10 5 20 1	726440	2 15 5 1	0.18384	2 20 10 5 1
7	19852	0.88654	14350	2 20 15 1	25330	2 20 5 10 1	0.59725	2 15 15 10 1
8	10571	0.50022	8230	2 10 20 15 1	21660	2 5 5 1	0.33963	2 15 20 20 1
9	36663	0.62073	25930	2 10 20 5 1	71420	2 10 20 1	0.41891	2 20 20 5 1
10	6276	1.31892	4270	2 10 20 15 1	13840	2 5 20 1	0.30653	2 5 15 1

Segment no.	Training stability belt width	NN configuration	No. of epochs	Training stability belt width	max. value of signal	Training stability belt width	Training stability belt width	Favourable Configuration
	max.		St. dev	St. dev		% max. value	% min. value.	
1	0.67061	2 20 5 1	120652	0.05773	6	11.18	7.59	2 15 10 5 1
2	3.69692	2 10 15 1	11231	0.42213	50	7.39	4.12	2 20 20 20 1
3	2.33175	2 5 10 1	16105	0.22013	40	5.83	3.19	2 20 20 1
4	2.88486	2 5 15 5 1	39022	0.32619	40	7.21	3.34	2 10 5 10 1
5	5.61412	2 5 5 1	26164	0.86263	100	5.61	1.55	2 20 20 20 1
6	0.40764	2 20 5 1	172304	0.04225	6	6.79	3.06	2 20 10 5 1
7	1.21092	2 5 20 5 1	2449	0.15081	50	2.42	1.19	2 20 20 1
8	0.67534	2 20 10 1	3097	0.08581	40	1.69	0.85	2 15 20 20 1
9	0.78866	2 20 10 20 1	11317	0.06955	40	1.97	1.05	2 20 20 5 1
10	2.17188	2 10 20 5 1	2074	0.54849	100	2.17	0.31	2 5 10 20 1

the training set for the neural network. The CCG characteristic is split into several segments, where each of them is modelled by its own neural network. The created model is then used as the interface between the measured ion current, the operating voltage, and the actual pressure readout of the CCG.

However, due to the contamination and aging of the CCG it needs to be recalibrated. The process is the same as it is in the case of the first calibration. The presented methodology is now fully developed and ready for use in practical applications. Since neural networks run on computers it is the matter of convenience whether it is realized on a separate computer or a special micro-computer system is developed (for example PIC 32 or similar) and this then becomes an integral part of the CCG device.

5 REFERENCES

[1] B. Erjavec, J. Šetina, L. Irmančnik-Belič, *Mater. tehnol.*, 35 (**2001**) 3/4,143–150 (in Slovene)

[2] B. Erjavec, J. Šetina, L. Irmančnik-Belič, *Mater. tehnol.*, 35 (**2001**) 5, 1–257 (in Slovene)

[3] L. Irmančnik-Belič, I. Belič, B. Erjavec, J. Šetina, *Mater. tehnol.*, 35 (**2001**) 6,15–420 (in Slovene)

[4] L. Irmančnik-Belič, I. Belič, B. Erjavec, J. Šetina, *Mater. tehnol.*, 36 6 (**2002**), 401–405 (in Slovene)

[5] L. Irmančnik-Belič, I. Belič, B. Erjavec, J. Šetina, Vacuum, 71 (**2003**), 505–515

[6] P. J. Bryant, W. W. Longley, C. M. Gosselin, J. Vac. Sci. Technol, 3 (**1965**) 2, 62

[7] R. N. Peacock, N. T. Peacock, D. S. Haucshulz, J. Vac. Sci Tehnol. 3 (**1991**) 1977

[8] L. Cusco, Guide to the Measurement of Pressure and Vacuum. The Institute of Measurement and Control, London (1998)

[9] A. Vesel, M. Mozetič, Vacuum, 67 (**2002**) 3–4, 629–633

[10] A. Vesel, M. Mozetič, A. Zalar, Vacuum, 71 (**2003**) 1–2, 225–228

[11] A. Vesel, M. Mozetič, Vacuum, 73 (**2004**) 2, 281–284

[12] A. Vesel, M. Mozetič, M. Žumer, V. Nemanič, B. Zajc, Vacuum, 78 (**2005**) 1, 13–17

[13] S. Wilfert, N. Schindler, Applied Physics A: Materials Science & Processing, 78 (**2004**) 5, 663–666

[14] S. Wilfert, C. Edelmann, Vacuum 82 (**2008**), 412–419

[15] N. T. Peacock, R. N. Peacock, J. Vac. Sci. Tehnol. 8 (**1990**), 2806

[16] N. T. Peacock, R. N. Peacock, J. Vac. Sci. Tehnol. 3 (**1988**), 1141

[17] B. R. F. Kendall, E. Drubetsky, J Vac Sci Technol, 3 (**1997**), 740

[18] P. A. Redhead,. Vacuum, 38 (**1988**) 8–10, 901

[19] I. Belič, L. Irmančnik-Belič, B. Erjavec, Strojarstvo 48 (**2006**) 1/2, 5–12

[20] I. Belič, Vacuum, 80 (**2006**) 10, 1107–1122

CARNIAN BAUXITES AT MULJAVA IN CENTRAL SLOVENIA

KARNIJSKI BOKSITI NA OBMOČJU MULJAVE V OSREDNJI SLOVENIJI

Stevo Dozet[1], Matjaž Godec[2]

[1]Geological Survey of Slovenia, Dimičeva ulica 14, 1000 Ljubljana, Slovenia
[2]Institute of Metals and Technology, Lepi pot 11, 1000 Ljubljana, Slovenia
matjaz.godec@imt.si

We have investigated the composition of Muljava Carnian bauxites. In the Muljava area in Central Slovenia bauxites of the Karst type have been discovered; these bauxites occur in several 10-m-thick horizon between the underlying Cordevolian and overlying Julian-Tuvalian carbonate rocks. Based on their texture the bauxites are predominantly iron-rich oolitic bauxites. However, they vary considerably in their mineral and chemical compositions in all directions. The main constituent minerals are kaolinite, boehmite, goethite, hematite and quartz. In addition, several particularities of the Muljava bauxite deposits are discussed.

Key-words: Bauxites, composition, textural particularities, EDS, WDS, Carnian, Lower Carniolia, Dinaric Carbonate Platform, Slovenia

Članek obravnava sestavo muljavskih karnijskih boksitov, ki so bili odkriti na območju Muljave v osrednji Sloveniji in so kraškega tipa. Pojavljajo se v več deset metrov debelem horizontu med spodaj ležečimi cordevolskimi in zgoraj ležečimi julsko-tuvalskimi karbonatnimi kamninami. Po strukturi pripadajo večinoma železnatemu oolitnemu boksitu. Mineralna in kemična sestava boksitov se znatno spreminja v vseh smereh. Glavni minerali v njihovi sestavi so kaolinit, boehmit, getit, hematit in kremen. V članku razpravljamo tudi o nekaterih posebnostih muljavskih boksitov.

Ključne besede: boksiti, sestava, struktura, posebnosti, EDS, WDS, karnij, Dolenjska, Dinarska karbonatna platforma, Slovenija

1 INTRODUCTION

Detailed geological investigations in the framework of the systematic regional field mapping for the Geological Map of Slovenia on a scale of 50,000 have been performed in the Muljava area and its wider surroundings. Between Muljava and the hamlet Vrhe a 1.5-kilometre-wide belt of the relatively heterogeneous Middle and Upper Carnian rocks crops out, being important, primarily, because of the iron-rich bauxites in the lowermost part of the Julian-Tuvalian stratigraphic sequence. The bauxite deposits lie unconformably upon the superficially eroded Cordevolian dolomite and under a 350-m-thick variegated Julian-Tuvalian predominantly carbonate stratigraphic sequence passing gradually upwards into the Upper Triassic Principal Dolomite in the Lofer development [1]. A sketch map of the study area is shown in **Figure 1**.

The scope of our work was to explore the Muljava Bauxite Member and to define its lithological, mineralogical and chemical composition, its boundaries, size, stratigraphic position and textural particularities.

Geographically, the investigated area belongs to the Dolenjska District [2] and from the geological and geotectonical points of view to the Dinaric Carbonate Platform and the Dolenjska-Notranjska Mesozoic Blocks, respectively [2,5]. The area has been investigated several times [2–10].

2 EXPERIMENTAL PROCEDURES

The main geological data presented in this work were obtained during the systematic regional and detailed geological mappings in the field for the Geological Map of Slovenia on a scale of 50,000, executed in this part of
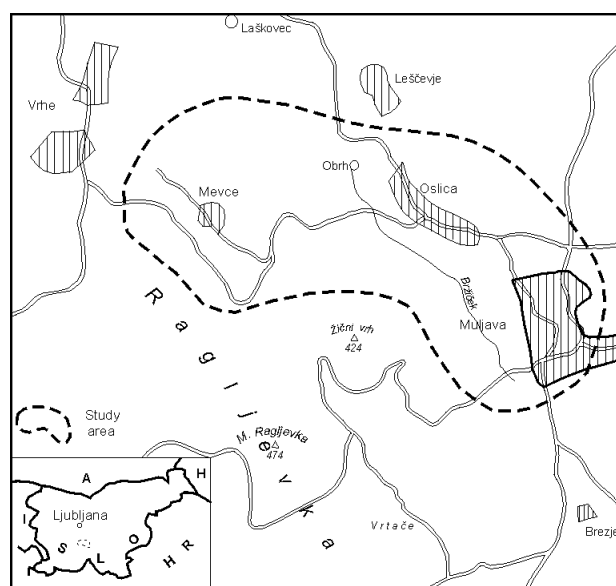
Figure 1: Location sketch map of the investigated area
Slika 1: Lokacijska skica zemljevida področja raziskav

Slovenia by the Geological Survey of Slovenia in the years 2005 to 2007. Detailed stratimetric measurements as well as a sedimentological and facial study of the Carnian sedimentary succession were performed as well. The carbonate rocks are classified according to the practical petrographic classification of limestones [11] and the classification of carbonate rocks according to the depositional texture [12]. The Muljava bauxite deposits are classified according to Valeton's classification of bauxites [13,14].

The microstructure of the bauxites was investigated with field-emission scanning electron microscopy FEG SEM JEOL JSM 6500F operating at a 15-kV accelerating voltage of the primary electron beam. The back-scattered-electron images were taken at 0.1 nA, and on the same spot the X-ray signal was collected from the $Fe_{K\alpha1}$, $O_{K\alpha1}$, $Si_{K\alpha1}$, $Al_{K\alpha1}$, $Ti_{K\alpha1}$, $Mn_{K\alpha1}$ and $K_{K\alpha1}$ transitions to obtain the energy-dispersive spectroscopy (EDS) X-ray mapping. Some structural details were microchemically analyzed with EDS and the EDS analyses were obtained from larger areas and averaged. The chemical compositions were calculated from the EDS measurements by stoichiometric calculation, considering the analysed element oxygen. The samples for electron microscopy were cut from larger pieces and dry ground up to 2400 SiC grinding paper. Additionally, the quantitative microanalyses were carried out using wavelength-dispersive spectroscopy (WDS) measurements (INCA CRYSTAL 400) in order to clarify the larger oxygen content, as this was expected in bauxite minerals. An accelerating voltage of 20 kV was used and a probe current of 10.24 nA was applied. The standard reference material orthoclase ($KAlSi_3O_8$) was considered to be appropriate for these measurements. The measurements were performed on four different surface features over an area of 100 μm × 80 μm and on several smaller features with an appropriately smaller site of interest.

3 RESULTS

3.1 Muljava bauxite deposits

The Muljava oolitic bauxites occur in a wide band extending from Muljava to the hamlet Vrhe. The bauxites are trapped in the Cordevolian carbonate rocks as a wide zone of outcrops striking NW-SE and dipping towards the northeast. The Muljava bauxite deposits are built of two varieties: yellow-orange and brown-red bauxites of different chemical and mineral properties. The stratigraphic position of the Muljava Bauxite is shown in **Figure 2**.

Underlying carbonate rocks – Footwall

The footwall of the Muljava bauxite deposits is built of light grey, very light grey and occasionally white, massive (prevalent) or bedded, more or less coarse-grained (crystallized, sparitic) dolomite with sections of
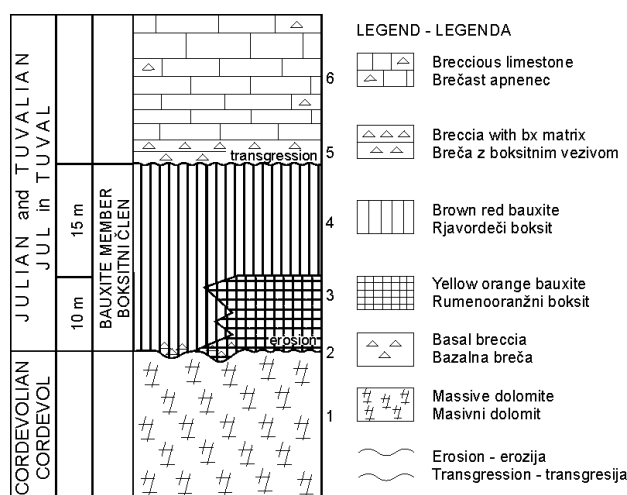
Figure 2: Stratigraphic position of the Muljava Bauxite Member
**Slika 2:** Stratigrafska lega muljavskega boksitnega člena

green algae Dasycladacea, mostly of the genus *Diplopora* and species *Diplopora annulata* Schafhäutl, which occurs in Slovenia in the Cordevolian beds. The upper surface of the Lower Carnian beds is karstified and due to karstification it is fairly irregular. The coarse-grained Cordevolian dolomite originated during the late diagenetic processes from the biostromal, inrasparitic and intrasparuditic *Diplopora* limestones. Intensified epirogenetic movements at the end of the Cordevolian epoch contributed to the shallowing of the sea. Afterwards, Cordevolian carbonate rocks were in spots exposed to karstification, erosion and weathering. These conditions enabled the origin of terra rossa and bauxites, which are, however, in the main part of eolian origin.

Muljava Bauxite Member

The lowermost and basal rock unit in the Carnian (Julian and Tuvalian) Oslica stratigraphic sequence is represented by a 25-m-thick bauxite horizon, the Muljava Bauxite Member respectively, consisting of three parts: 1) the basal calcareous breccia, 2) the yellowish orange oolitic bauxite, and 3) the brown-red iron oolitic bauxite.

Basal calcereous breccia occurs in the form of lenses close above the dolomite paleorelief. The basal breccia consists of angular fragments of light grey coarse-grained Cordevolian dolomite bound with calcitic cement and a limonitic matrix. The thickness of the basal breccia does not exceed one metre.

Yellowish orange bauxites form the up to 10-m-thick lower part of the Muljava bauxites. The upper boundary of these bauxites is flat, and the lower one, representing the contour of the terrain, is fairly irregular and causes a minor variability in the thickness of the bauxite. The yellow-orange bauxites include varieties of yellow, yellowish orange, brownish orange and light brown colour. There are also samples of a gentle rose colour.
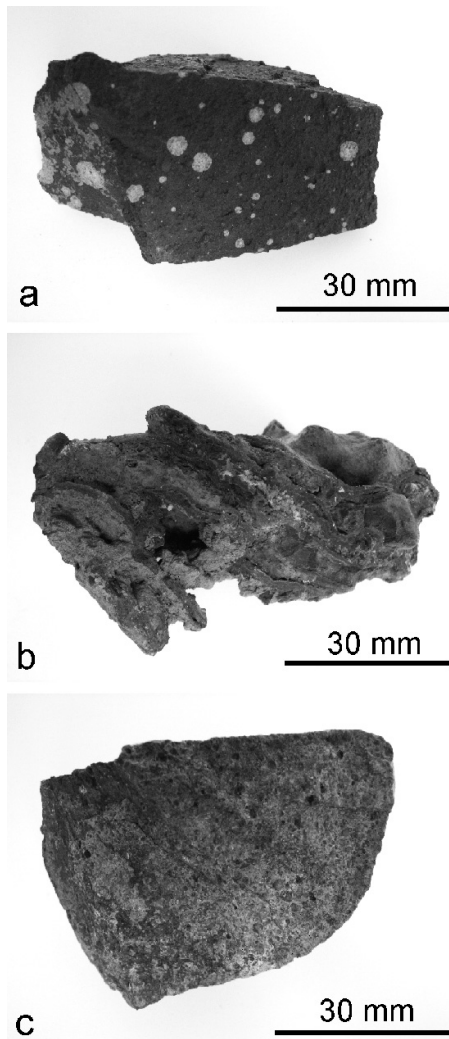
The yellow-orange bauxites are massive and have the pelitic as well as the oolitic texture. The oolitic texture is not quite homogeneous, because ooids are not as numerous as in the overlying brown-red bauxites.

Brown-red bauxites are of reddish brown, brick-red, brownish red and dark red colour varieties, and mostly oolitic and pisolitic bauxites lying in the up to 15-m-thick upper part of the Muljava Bauxite Member. The bauxites are relatively homogeneous and very compact, and without stratified structures. Pisolites and the pisolitic texture are much less frequent than ooides and the oolitic texture. Pisolites form dark red grains in the bauxite of various sizes, from several mill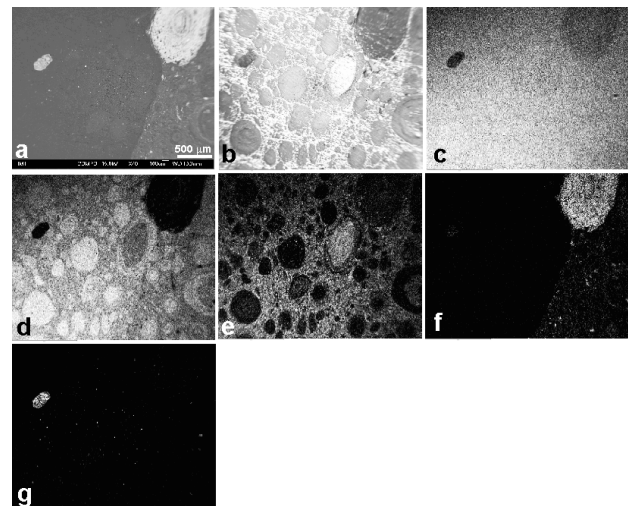imetres to one centimetre and a half. Their arrangement can be different, but chiefly they are randomly scattered in the bauxite mass. Pisolites are of a homogeneous structure or concentrically layered with an increasing content of iron towards the centre of the pisolites.

Source material and the origin of bauxites

The Muljava brown-red oolitic bauxites were formed during weathering of the coarse-grained ("saharoid") poorly bound predominantly massive Lower Carnian (Cordevolian) dolomite and in the eolian way. On the basis of reference data and our investigations it is not possible to estimate the part of autochtonous bauxite material and the rate of matter brought by winds.

Our investigations indicate that Triassic yellow-orange bauxite deposits in the Muljava area consist of clay, bauxitic clays and clayey bauxites. Their source is considered to be the weathered material of adjacent brown-red iron-rich oolitic bauxites. In some places the

Figure 3: Macrograph of bauxite mineral (a) Muljava 3 (b) Muljava 6 and (c) Muljava 8
Slika 3: Makroposnetek boksitnega minerala (a) Muljava 3 (b) Muljava 6 in (c) Muljava 8

Figure 4: Electron micrograph (secondary-electron image) of Muljava 3 sample – fracture surface
Slika 4: Elektronska slika (slika sekundarnih elektronov) vzorca Muljava 3 – prelomna površina

Figure 5: EDS X-ray mapping of Muljava 3 grinded sample (a) backscattered-electron image, (b) secondary-electron image and corresponding X-ray images (c) O $K_{\alpha 1}$ (d) Al $K_{\alpha 1}$ (e) Si $K_{\alpha 1}$ (f) Fe $K_{\alpha 1}$ (g) Ti $K_{\alpha 1}$
Slika 5: Rentgenska EDS ploskovna porazdelitev elementov bruše-nega vzorca Muljava 3 (a) slika odbitih elektronov, (b) slika sekundarnih elektronov in pripadajoče rentgenske slike (c) O $K_{\alpha 1}$ (d) Al $K_{\alpha 1}$ (e) Si $K_{\alpha 1}$ (f) Fe $K_{\alpha 1}$ (g) Ti $K_{\alpha 1}$

x/%	O	Al	Si	Ti	Fe
Spectrum 1	72,03	21,10	6,39	0,27	0,21
Spectrum 2	69,61	21,78	5,59	9,35	2,67
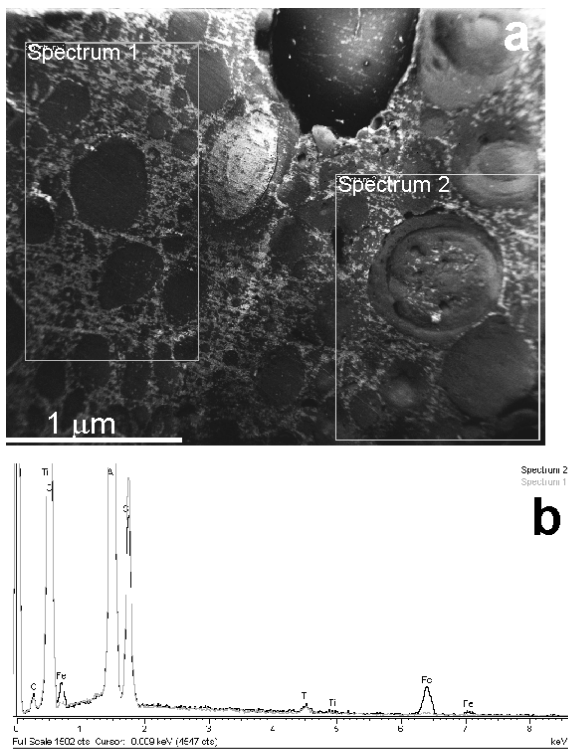
Figure 6: (a) Electron micrograph (secondary-electron image) of Muljava 3 grounded surface with marked areas of EDS analysis, (b) EDS spectra, (c) chemical composition of both analyses in mole fractions (%)

Slika 6: (a) Elektronski posnetek (slika sekundarnih elektronov) brušenega vzorca Muljava 3 z označenimi področji, kjer je bila narejena EDS analiza, (b) EDS spektra, (c) kemična sestava obeh analiz je navedena v molskih deležih (%)

Figure 7: EDS X-ray mapping of Muljava 3 grinded sample (a) backscattered-electron image, (b) secondary-electron image and corresponding X-ray images, (c) O $K_{\alpha 1}$ (d) Al $K_{\alpha 1}$ (e) Si $K_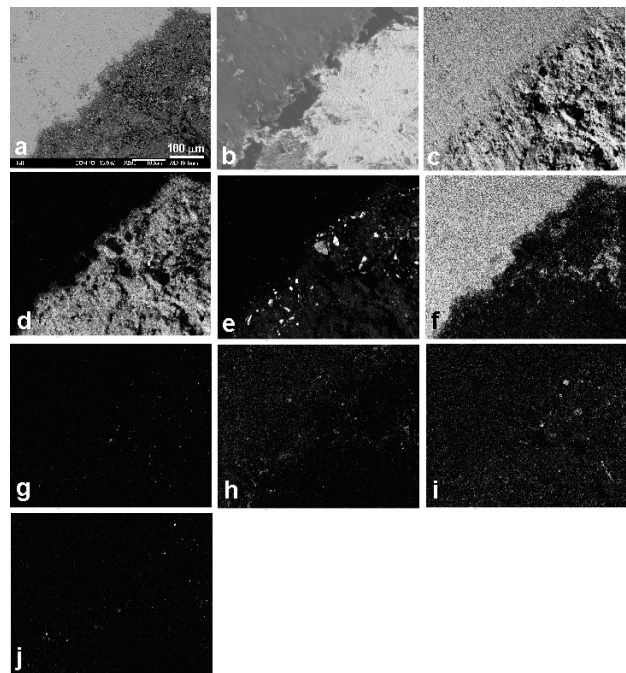{\alpha 1}$ (f) Fe $K_{\alpha 1}$ (g) Ti $K_{\alpha 1}$ (h) Mn $K_{\alpha 1}$ (i) K $K_{\alpha 1}$ (j) Ca $K_{\alpha 1}$

Slika 7: Rentgenska EDS ploskovna porazdelitev elementov brušenega vzorca Muljava 3 (a) slika odbitih elektronov, (b) slika sekundarnih elektronov in pripadajoče rentgenske slike, (c) O $K_{\alpha 1}$ (d) Al $K_{\alpha 1}$ (e) Si $K_{\alpha 1}$ (f) Fe $K_{\alpha 1}$ (g) Ti $K_{\alpha 1}$ (h) Mn $K_{\alpha 1}$ (i) K $K_{\alpha 1}$ (j) Ca $K_{\alpha 1}$

brown-red oolitic bauxites were decomposed, eroded, transported and accumulated (trapped) in adjacent depressions and consolidated into a fairly compact yellow-orange bauxite ore. Occasionally, individual broken layers and irregular patches of brown-red oolitic bauxites are preserved in the yellow-orange oolitic bauxites. Accordingly, the yellow-orange oolitic bauxites are resedimented brown-red oolitic bauxites.
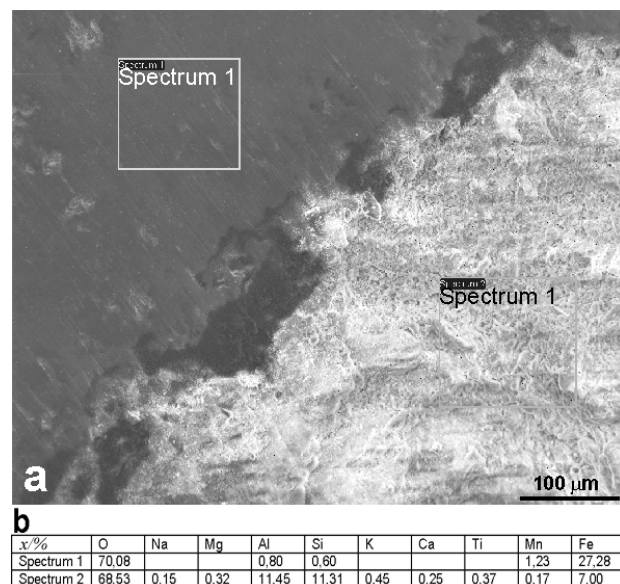
Overlying sediments – Hanging wall

The described Muljava Bauxite Member is transgressively overlain by an about 350-m-thick fairly heterogeneous and gray-coloured sedimentary succession composed of various limestones, dolomites, calcareous breccias, marlstones, and subordinately variegated clastic rocks, that starts with basal calcareous breča with a bauxitic matrix.

Limestone breccia with a bauxitic matrix. The hanging wall sedimentation starts with transgressive limestone breccia with a bauxitic matrix. On the

x/%	O	Na	Mg	Al	Si	K	Ca	Ti	Mn	Fe
Spectrum 1	70,08			0,80	0,60				1,23	27,28
Spectrum 2	68,53	0,15	0,32	11,45	11,31	0,45	0,25	0,37	0,17	7,00

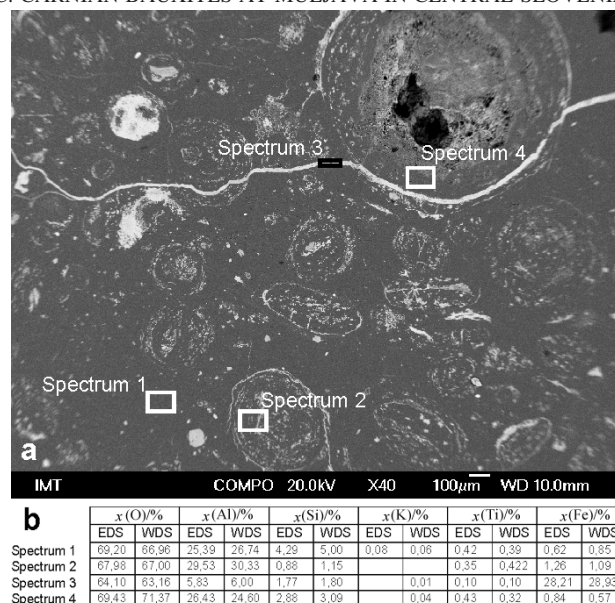**Figure 8:** (a) Electron micrograph (secondary-electron image) of Muljava 6 grounded surface with marked areas of EDS analysis, (b) chemical composition of both analyses in mole fractions (%)

Slika 8: (a) Elektronski posnetek (slika sekundarnih elektronov) brušenega vzorca Muljava 6 z označenimi mesti, kjer je bila izvedena EDS analiza, (b) kemična sestava obeh analiz v molskih deležih (%)

boundary between the bauxite horizon and the Julian thick-bedded limestone occurs an about 1-m-thick lenslike bed of brownish grey medium-grained compact limestone breccia bound with a limonitic and bauxitic matrix. It consists of minor and bigger angular fragments, black and grey micritic and rarely sparitic limestones belonging to the lowermost Julian sedimentary succession.

3.2 Microstructural examination

Muljava bauxites 3, 6 and 8 were chosen for detailed structural and microchemical analyses (**Figure 3**). The compositions of all three bauxites are shown in **Table 1. Table 2** shows the results of the elemental composition converted to oxides. The Muljava 3 sample was fractured and the fracture surface was investigated (**Figure 4**). Small ooids with sizes from 0.1 mm up to 1 mm form the convex fracture surface topography, while larger pisolites of yellow colour are not distinguished in the secondary-electron mode of imaging. The polished Muljava 3 sample surface was investigated with EDS X-ray mapping (**Figure 5**). The left part of the image represents a larger pisolite of light yellow colour with a lower iron concentration. The EDS analyses of the light yellow and dark red-brown regions are shown in **Figure 6**. The spectra of the respective regions as well as the corresponding chemical compositions are also shown. The amount of oxygen, aluminium and silicon is similar, while in the red-brown region the titanium and iron contents are higher. Also, the additional measurements shown were similar results. EDS X-ray mappings were obtained on a polished surface of the sample Muljava 6 (**Figure 7**). The analysis area was chosen to show both bauxite minerals, dark-brown and yellow in the left-top and in the right-bottom part of the EDS map, respectively. The left-top region is rich in iron and fairly uniform concerning other elements' distribution. On the other hand, the right-bottom region has non-uniformly distributed silicon, iron and potassium. The results of the local areas EDS measurements show a much higher iron content in the dark-brown layer and a higher concentra-

	x(O)/%		x(Al)/%		x(Si)/%		x(K)/%		x(Ti)/%		x(Fe)/%	
	EDS	WDS	EDS	WDS	EDS	WDS	EDS	WDS	EDS	WDS	EDS	WDS
Spectrum 1	69,20	66,96	25,39	26,74	4,29	5,00	0,08	0,06	0,42	0,39	0,62	0,85
Spectrum 2	67,98	67,00	29,53	30,33	0,88	1,15			0,35	0,422	1,26	1,09
Spectrum 3	64,10	63,16	5,83	6,00	1,77	1,80		0,01	0,10	0,10	28,21	28,93
Spectrum 4	69,43	71,37	26,43	24,60	2,88	3,09		0,04	0,43	0,32	0,84	0,57

Figure 9: (a) Electron micrograph (secondary-electron image) of Muljava 8 grounded surface with marked areas of EDS and WDS analyses. (b) Chemical composition of four spectra obtained by EDS and WDS in mole fractions (%)
Slika 9: (a) Elektronski posnetek (slika sekundarnih elektronov) brušenega vzorca Muljava 8 z označenimi mesti, kjer je bila izvedena EDS in WDS analiza, (b) kemična sestava v molskih deležih (%), dobljena z EDS- in WDS-analizo

tion of aluminium and silicon in the yellow layer (**Figure 8**). Microchemical analyses using EDS and WDS were performed on exactly the same areas as the sample Muljava 8. The sample seems to be more homogeneous, except for the thin curved iron-rich layer. The results of the oxygen-content measurements obtained with both analyzing techniques are very similar (**Figure 9**). The reliability of the measurements was additionally checked against several standards: $NaAlSi_3O_8$ (albite), Al_2O_3, SiO_2 and $CaSiO_3$ (wollastonite). With reference to these standards none of the two analytical techniques, WDS or EDS, measures the elemental concentrations in mole fraction with an error greater than 1.5 %. The oxygen concentration in mole fraction measured in all three Muljava samples is approximately 20 % too high to match the data-processing software proposed for the

Table 1: Chemical composition of Muljava 3, 6 and 8 bauxite in mole fractions (%)
Tabela 1: Kemična sestava boksitnega vzorca Muljava 3, 6 in 8 v molskih deležih (%)

x/%	O	Mg	Al	Si	K	Ca	Ti	Mn	Fe
Muljava 3	70,82	–	21,44	5,99	–	–	0,27	–	0,21
Muljava 6	68,88	0,12	10,16	4,96	0,16	0,13	0,14	0,19	19,15
Muljava 8	70,07	–	24,15	3,77	–	–	–	–	1,54

Table 2: Chemical composition of of Muljava 3, 6 and 8 bauxite calculated to oxides in mass fractions (%)
Tabela 2: Kemična sestava boksitnega vzorca Muljava 3, 6 in 8 v masnih deležih, preračunano na okside

x/%	Al_2O_3	SiO_2	MnO	TiO_2	MgO	CaO	K_2O	FeO
Muljava 3	68,06	24,05	–	1,60	–	–	–	6,29
Muljava 6	14,07	15,53	4,16	0,54	0,24	0,36	0,38	64,72
Muljava 8	75,73	14,89		2,38	–	–	–	7,00

compounds Al_2O_3, SiO_2 and FeO. Our previous X-ray diffraction (XRD) measurements showed [to be published] that Si and Al create kaolinite rather than quartz and alumina oxide and the Fe might be incorporated into hematite, goethite or limonite. Having this in mind, the calculation is far more correct and only a little excess oxygen is obtained, which can be explained by surface oxygen contamination.

4 CONCLUSIONS

Muljava with the wider surroundings is built of Triassic rocks belonging to three formations: Cordevolian dolomite, Middle and Upper Carnian Oslica Beds as well as Upper Triassic Principal Dolomite.

The bauxite deposits of the considered part of Dolenjska are arranged along the Cordevolian/Julian contact.

The bauxites of Muljava and the wider neighbourhood belong to the Karst or "terra rossa" type of bauxites, being of sedimentary origin. They are denoted as "Muljava Bauxite Member".

The Muljava bauxites lie discordantly upon the Cordevolian dolomite and they are transgressively overlain by a predominantly carbonate Julian-Tuvalian sedimentary succession. The about 25-m-thick Muljava Bauxite Member involves three parts (from bottom to top): 1) basal dolomite breccia, 2) yellow-orange bauxites and 3) brown-red bauxites.

Basal dolomite breccia consists of Cordevolian dolomite fragments bound with calcitic cement and limonitic matrix.

In the lower part of the Muljava Member ***yellow-orange bauxites*** predominate with pelitic and oolitic textures.

The upper part of the Muljava Member includes ***brown-red*** fairly commonly silicious and ferrous ***bauxites***, which are unsuitable for the production of alumina due to their high contents of iron and silica.

The Muljava brown-red oolitic bauxites originated during weathering of the Lower Carnian (Cordevolian) dolomite and in the eolian way. On the basis of the collected data it is not possible to estimate the part of autochthonous bauxite material and the rate of the alochtonous substance brought by winds. The yellow-orange bauxites are resedimented brown-red bauxites.

Microchemical analyses performed in a FEG SEM based on the EDS and WDS techniques have shown that Muljava bauxites consist of larger pisolites and small ooids from yellow to a dark red-brown colour, depending on the iron content. A higher iron concentration gives a darker red-brown colour to the bauxite mineral, while areas with less iron usually have higher aluminium and silicon concentrations. Ooids have an onion-like structure, where layers rich in aluminium and silicon follow each other. We also observed ooids consisting mostly of either silicon oxide or aluminium oxide.

5 REFERENCES

[1] Fischer, A. G. The Lofer cyclothems of the Alpine Triassic. In: Merriam, D. F. (ed.) – *Kansas Geol. Surv. Bull.*, 169 (**1964**), 107–149

[2] Melik, A. *Posavska Slovenija,* II/3. – Slovenska matica, Ljubljana, 1959, 595 pp.

[3] Buser, S. Osnovna geološka karta SFRJ 1:100 000, list Ribnica. – *Zvezni geološki zavod*, Beograd (1969)

[4] Buser, S. Tolmač lista Ribnica. Osnovna geološka karta SFRJ 1:100 000. – *Zvezni geološki zavod*, Beograd, 1974, 60 pp.

[5] Buser, S. Development of the Dinaric and the Julian carbonate Platforms and of the intermediate basin (NW Yugoslavia). – *Mem. Soc. Geol. It.*, Trst, 40 (**1989**), 313–320

[6] Buser, S. & Lukacs, E. The results of recent geological bauxite exploring in Slovenia. – *Ref. 6. savet. geol. FLRJ*, Ohrid, 2 (**1966**), 292–304

[7] Buser, S. & Lukacs, E. Bauxite in Slowenien. – *Ann. Inst. Geol. Publ. Hungarici*, Budapest, 54 (**1973**) 3, 209–220

[8] Berce, B. Pregled železnih nahajališč SR Slovenije. – *Prvi jugosl. geol. kongres*, Ljubljana, 1 (**1956**), 235–239

[9] Dozet, S. Stratigrafski razvoj julske in tuvalske podstopnje na območju Oslice pri Muljavi. – *Geologija*, Ljubljana, 45 (**2002**) 2, 353–358

[10] Dozet, S. O. karnijskem oolitnem železnatem boksitu Kopitovega griča ter o plasteh v njegovi talnini in krovnini. – *RMZ Mater. Geoenvir.*, Ljubljana, 51 (**2004**) 4, 2191–2208

[11] Folk, R. I. Practical petrographic classification of limestones. – *Amer. Ass. Petrol. Geol. Bull.*, Tulsa, 43 (**1959**) 4, 1–38

[12] Dunham, R. J. Classification of carbonate rocks according to depositional texture. In Ham, W. E. (ed.): Classification of carbonate rocks. – *AAPG Memoir*, Tulsa (**1962**), 108–121

[13] Valeton, I. *Bauxites,* Elsevier, Amsterdam 1972, 213 pp.

[14] Valeton, I. Consideration for the description and nomenclature of bauxites. – *Travaux ICSOBA*, 9 (**1973**), 105–110

AN INVESTIGATION OF THE ECONOMICS OF USING WELDED LAYERS FOR SOME PARTS OF WORM PRESSES FOR THE EXTRACTION OF OIL FROM SUNFLOWER SEEDS

RAZISKAVE UPORABNOSTI NAVARJENIH PLASTI ZA DELE VIJAČNIH STISKALNIC ZA EKSTRAKCIJO OLJA SONČNIC

Vlatko Marušić[1], Milan Kljajin[1], Sanja Marušić[2]

[1]Mechanical Engineering Faculty in Slavonski Brod, University Josip Juraj Strossmayer of Osijek, Croatia
[2]Industrial-tradesman's School, Slavonski Brod, Croatia
vlatko.marusic@sfsb.hr

The working parts of worm presses from different manufacturers were collected from oil mills in Croatia, Vojvodina and Bosnia and Herzegovina. The chemical composition, microstructure and hardness were determined, and the wear was examined for the original (imported) and the substituted (domestic) parts. The direct costs of tribological origin are larger for the substitute parts than for the original parts and they depend on the protective surface layer. The indirect tribological losses are a few tens of times greater than the direct tribological losses. The wear resistance of the welded layers was tested experimentally on extraction cage knives and the results are compared to carburised knives (the substitution solution) commonly used in oil mills. It was found that the wear resistance of the welded layers does not depend only on the surface hardness, but more so on the microhardness and the distribution of the carbide particles in the tough matrix. Based on recordings in oil mills and on the results of our investigation, we concluded that the use of welded layers instead of carburised layers could extend the lifecycle of the parts of the presses. In this way, the efficiency of the oil extraction could be increased and the economics of operating oil mills could be improved.

Key words: worm-presses, sunflower, welded layers, wear, economics

Zbrani so bili deli različnih proizvajalcev za stiskalnice za sončnično olje iz oljarn na Hrvaškem, v Vojvodini in v Bosni in Hercegovini. Analizirana je bila kemična sestava, izmerjena trdota, pregledana mikrostruktura in analizirana obraba izvirnih (uvoženih) in nadomestnih (domačih) delov. Neposredni stroški tribološkega izvora so za nadomestne dele večji kot za izvirne in so odvisni od površinske (varovalne) plasti. Indirektni tribološki stroški so nekaj desetkrat večji od direktnih. Obrabno obstojnost navarjenih slojev smo eksperimentalno preverili na nožih iz ekstrakcijske kletke, rezultate pa smo primerjali s cementiranimi noži (nadomestna rešitev), ki se večinoma uporabljajo v oljarnah. Ugotovili smo, da obrabna obstojnost navarjenih plasti ni odvisna samo od trdote površine, ampak bolj od mikrotrdote in od porazdelitve karbidnih zrn v žilavi matici. Na podlagi podatkov iz oljarn in rezultatov raziskave sklepamo, da lahko uporaba navarjenih plasti namesto cementiranih podaljša trajnostno dobo delov stiskalnic. Tako se poveča učinkovitost ekstrakcije olja in izboljša gospodarnost oljarn.

Ključne besede: vijačna stiskalnica, sončnično seme, navarjena plast, obraba, gospodarnost

1 INTRODUCTION

The working parts – worm segments and extraction cage knives – of worm presses for extracting oil are a striking example of a tribological system where wear is unavoidable. Operating with worn out worm segments increases the residual oil content in the cake. In oil mills with pre-pressing only, a too high residual oil content in the cake increases the consumption of hexane [1] and slows down the operation of the extraction plant, thereby decreasing its capacity. For oil mills with pre-pressing and final pressing the increased amount of oil residue in the cake increases the oil loss, could cause problems with correct storage and affects the quality of the cattle food prepared from the cake. Operating with worn out extraction cage knives also increases the number of tiny particles of metal in the extracted oil and as a result of this more frequent choking and damage to the filters during cleaning occurs [2]. The increasing amount of metal

in the oil also decreases the installed capacity of the pressing plant.

Although in oil mills due attention is given to the removal of metal from the oil because of its pro-oxidative effect, the increasing severity of regulations regarding the ecological quality of food means it will require even more attention in the future.

In spite of the numerous technological factors influencing the efficiency of oil extraction [3], e.g., the technological ripeness of the seeds, adjustments to the hulling machine, the character of the hulling and the conditioning parameters, the total oil extraction (depending upon the hybrid it is in most cases about 45 % to 50 % of the oil in the sunflower) depends not only on the type of worm press and the adjustment of the working parts (worm-screw pitch and the distances between the knives along the working fields) but also on a correctly defined criterion for the end of their functional working time, i.e., on the allowed dimensional

wear before failure or replacement (the so-called wear-reserve) [4].

The need for stronger regional connections was the reason for the systematization of earlier recorded results on the work of worm presses in two oil mills in Voj-vodina ("Mladost" in Šid and "Dijamant" in Zrenjanin – English and Russian equipment), in one oil mill in Bosnia and Herzegovina ("Bimal" in Brčko – German equipment), and in two Croatian oil mills ("Zvijezda" in Zagreb and "T.U. Čepin" in Čepin – English and German equipment). The data from interviewing and polling on the quantities of sunflower seeds processed before the replacement of the worm presses' spare parts, either original imported or domestic substitutes, were collected. The data were used for the calculation of the cost of worm-press parts per ton of processed sunflower seeds. It was found that the costs of the working parts of presses per ton of processed sunflower ranged from about € 0.35/t for original parts to about € 0.45/t for domestic substituted knives, and from about € 0.45/t for original parts to about € 0.90/t for domestic substitution segments.

On the basis of the data it was decided to investigate the possibility of applying our solution of welded layers to extend the lifecycle of the parts of presses and also to investigate the influence of protective layers on the working efficiency of the pressing plant and the operation of the entire oil mill.

2 MATERIAL AND METHODS

The parts of the worm presses of different manu-facturers were collected over several years for the purpose of establishing the protection procedures applied so far.

The readiness of the maintenance staff in the mentioned oil mills allowed us to collect imported parts (original and substitute) and the parts made in domestic factories as substitutes. The worm press is shown in **Figure 1**.

The characteristic wear traces on the surfaces of the used knives and worm segments are shown in **Figure 2**.

The abrasive ($SiO_2 \cdot H_2O$) [5,6] contained in the hulls of the sunflower seeds (the most common high-oil seeds produced in our region) is the main cause of the wear to worm-press components and the extraction cage knives. Its hardness (about 6 by Mohs, i.e., more than $HV = 1000$) directly affects the wear mechanism of the working surfaces of worm-press parts and for this reason, the type of applied protective layer affects the life time of these parts. It was found that the dominant wear mechanism was a selective abrasion, characterized by furrows in the direction of the relative movements of the meal – the working surface. Pores and small pits were observed at the places where the carbide particles were removed from the matrix and protrusions were observed where these hard particles, a constituent of the

alloy microstructure, stuck out from the surrounding softer matrix. It was found that carbides on the welded layer Stellit 6 are the result of high-pressure pressing into a resisting Co matrix and so produce a creased matrix (**Figure 2c**).

The hardness distribution $HV1$ from the surface towards the core of the worn worm segments and the extraction cage knives was determined on parts protected by thermal-chemical processing, because they provided fairly homogenous depths of the layer on all the surfaces [7]. Unequal wear on the working surface parts was found and the following was established:

- The wear of the worm segments is the greatest on the frontal part of the top worm screw, less wear occurs on the top of the top worm screw and even less on the front side of the worm screw, while the body of the segment and the backside of the worm screw are only slightly worn out.

- The wear of the extraction cage knives is the greatest on the leading edge, somewhat less on the back edge, even less on the upper working surface and only slight on the lateral sides.
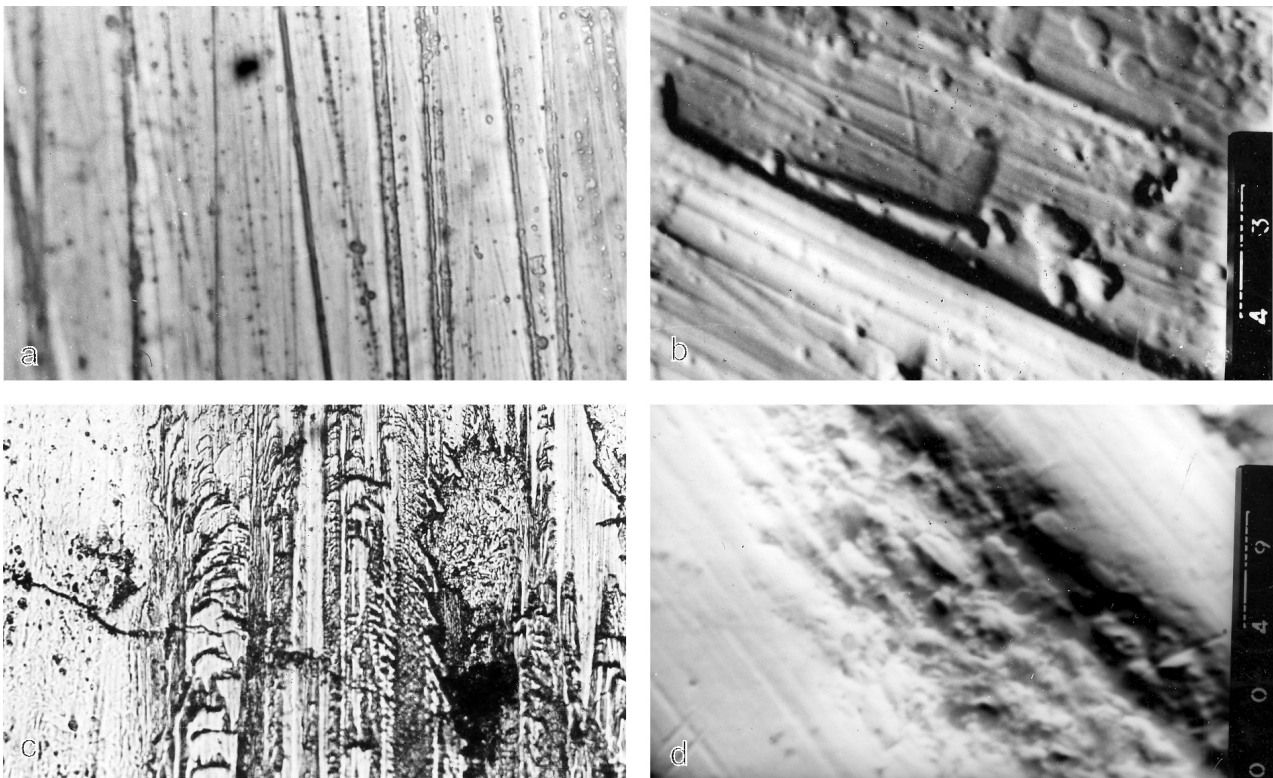
In the investigation of the wear resistance of different protective layers and with monitoring of the performance
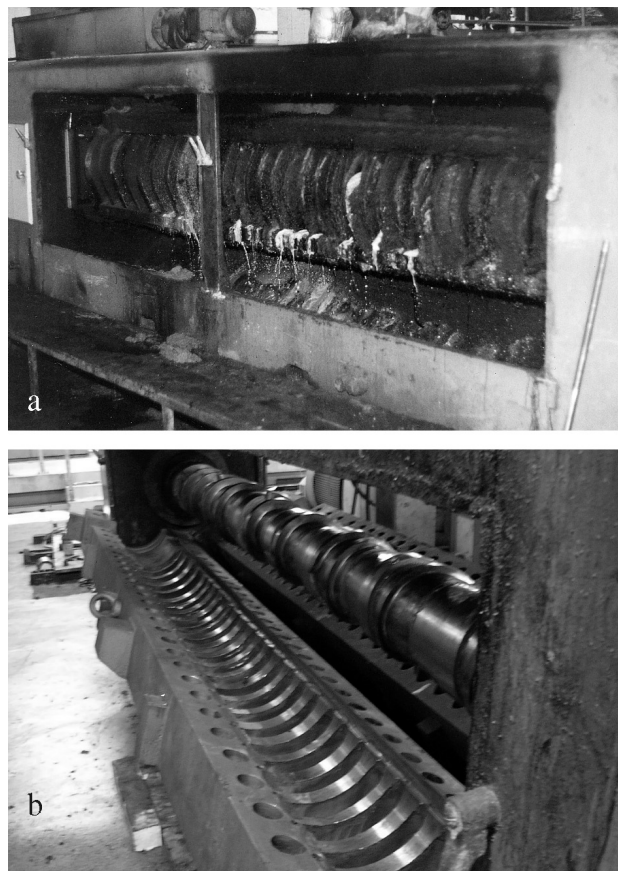
Figure 1: Worm press for oil extraction (a – in operation and b – opened with new cage knives)
Slika 1: Vijačna stiskalnica za ekstrakcijo olja (a – med delom, b – odprta z novimi noži kletke)

Figure 2: Characteristic wear traces of different protective layers on the parts of the presses: a – Carburised layer, optical microscope, mag. x200; b – Carbonitrided layer, SEM, mag. x700; c – Welded layer Stellite 6, optical microscope, mag. x200; d – High-grade steel for cold work, SEM (TOPO), mag. x700

Slika 2: Značilni sledovi obrabe na različnih varovalnih plasteh na delih stiskalnic; a – cementirana plast, optični mikroskop, pov. 200-kratna; b – karbonitrirana plast, SEM pov. 700-kratna; c – navarjena plast Stellit 6, optični mikroskop, pov. 200-kratna; d – orodno jeklo za delo v hladnem, SEM, pov. 700-kratna

during oil extraction, the uneven wear of the parts of the working surfaces, the uneven wear of the worm nut segments and of the extraction cage knives along the working surfaces from the meal intake to the cake discharge were established. The conclusions were as follows:

- The wear of the extraction cage knives is greater in the working fields where the oil extraction is most intensive.
- The wear of the worm segments is the strongest in the discharge working fields.

The differences can be related to the change of the radial and axial components of the pressure upon the meal by the working fields along the worm screw during its movement from the meal intake to the cake discharge [8].

3 PRE-EXPERIMENTAL INVESTIGATIONS OF THE PROTECTIVE LAYERS AND SELECTION OF THE OPTIMAL VARIANT

A lot of information about wear protection for the parts of oil presses during oil extraction is not available, as it known to the manufacturers of worm presses. Based on accessible references, the results of our on-site collection and the investigation of the original and spare parts the following conclusions were drawn:

- The original parts of the presses most often have a protective layer obtained by depositing additional material. Russian presses (one oil mill) had carbonitrited working surfaces, while the German presses (older solutions) had carburised surfaces.
- The thickness of the protective layer on the worm screw ranged from 4 mm to 5 mm, on the body of the worm assembly parts it was about 2 mm, and the same on the upper working surface of the extraction cage knives.
- The effective depth of the carbonitrided layers (according to the criterion Edc HV1 = 550) on both the worm assembly parts and the extraction cage knives of the Russian presses was about 1.8 mm, while the effective depth of the carburised layers was in the range from 0.6 mm to 1.8 mm.
- With domestic substitution solutions, in addition to the welded layers with similar depths to the original parts, two approaches were noted. The first was the carburising to an effective depth of 0.6 mm to 1.2 mm (depending on the part supplier) and the second was the surface quenching of tool steel for cold work (and subsequent tempering) with a quenched layer depth of 2 mm to 3 mm.

Table 1: Oil content in the meal and the average mass loss of the knives per working field for carburised knives
Tabela 1: Vsebnost olja v gneteni masi in povprečna izguba mase na delovno polje za cementirane plasti

Working fields	I	II	III	IV	V	VI	VII
Average mass loss, m/g	12.34	16.29	19.57	24.45	13.61	11.07	12.15
Oil portion in meal, w/%	49.61	47.43	41.26	30.05	21.64	16.03	12.39

The extraction cage knives were chosen for the investigation with regard to the fact that in every working field, depending on the press type, from fifty to sixty knives are built in. This gives us the possibility of installing experimental knives into oil presses in addition to the knives owned by the oil mill. In this way the same conditions of testing (e.g., the pressure, the quantity of abrasive and oil, the temperatures, the relative speeds of meal movement along the working-examination surface of sample knives etc.) were achieved for all the knives.

The tests of wear resistance on the working parts of the presses during oil extraction were carried out in the oil mill with presses for pre-pressing and final pressing (without oil flat cake extraction). These presses have seven working fields, defined by the size of the knives' gaps acting as the oil extraction. The opening width of these gaps is 0.75 mm in the first working field (at the entrance of the meal in the press) and decreases to 0.15 mm in the seventh working field, before the exit of the oil cake from the press.

Considering that the presses were newly designed (since being put into operation in 2002), the preliminary testing was carried out to define the working fields with the most exposed wear of the knives. For this purpose, 21 knives were randomly selected from a complete, new replacement set. A laboratory investigation showed that the complete set had a carburised layer with an effective depth of 1.2 mm, and a surface hardness of HRC 56 to 58. Selected knives were marked and weighed (with an accuracy of 0.01 g). The mass of one knife (dimensions 11 mm x 25 mm x 300 mm) was 620 g. During the replacement of worn original marked knives three experimental knives were built into each working field of the final pressing.

After 3500 tons of processed sunflower meal, all the knives were taken out for replacement. From the weight of the marked knives the loss of mass for each knife per working field was calculated (**Table 1**). Data on oil extraction from the meal per working field are also given in **Table 1** (the samples of meal were taken after the meal had been overdone in the press). The oil content in the meal was determined according to ISO 659 [9].

From the results of the weight loss it is clear that the wear is increased in working fields III and IV, and that the weight loss decreases in the output working fields. This is logical because in these fields the oil extraction was the most intensive, as shown by the oil residue in the meal.

4 RESULTS OF EXPERIMENTAL INVESTIGATIONS

As the welded layers were found to be most often applied in the most worn parts of the presses, three types of additional material for the welding of the surface layers were chosen for the experimental investigations of wear resistance in the contact with sunflower seeds as an abrasive medium in the routine operation of the worm presses. The carburised layer was chosen as a reference protective layer because this is used in most cases as a substitution solution for the worn original parts of the press.

The case of hardening steel 16MnCr5 (Č4320) was selected as the basic material for all the samples.

The same manufacturer supplied all three additional materials for the welded layers of knives, which varied in production costs and chemical composition (see **Table 2**).

Table 2: Prices and nominal chemical compositions of the additional materials
Tabela 2: Cene in nazivna kemična sestava dodajnih materialov

| Ordinal number	Internal mark	Chemical composition, w/% [1]	Price, kn/kg [1]
1	A	0.6 % C, 7 % Cr, 0.4 % Mo	80.00
2	B	2 % C, 31 % Cr, 11 % W, rest Co	560.00
3	C	3 % C, 40 % Fe, rest W carbide	675.00
[1] Approximate value			

The box carburising of previously ground samples (Ra = 0.8 μm) was performed for 10 h at 950 °C. The carburised knives were air cooled, quenched from v_k = 850 °C and tempered at v_p = 200 °C. When measuring the hardness profile $HV1$, the effective depth of the layer was found to be Edc = 1.2 mm, and the surface hardness was HRC 59.

The welded material was deposited (by REL) in two layers using a Ø 3.25 mm electrode. The knives were then machined with grinding to Ra = 0.8 μm. The hardness of the welded knives was as follows: welded layer A HRC 60; welded layer B HRC 57; welded layer C HRC 62. The hardness $HV1$ measurements from the surface of the welded layer to the core of the knives showed that the thickness of the layer with a hardness above $HV1$ 550 ranged from 1.9 mm to 2.3 mm.

Characteristic microstructures of the surface zones of the experimental protective layers are shown in **Figure 3**.
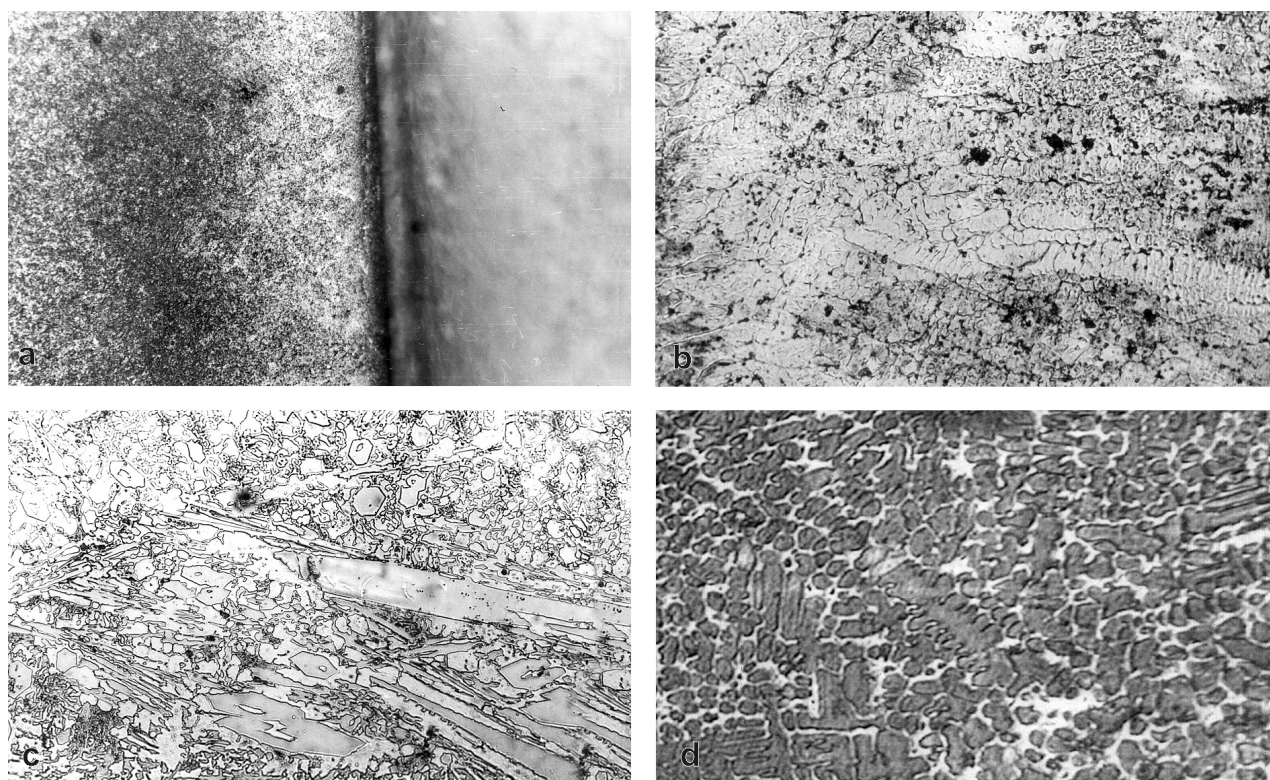
Figure 3: Characteristic microstructures of the surfaces of the experimental protective layers (mag. 200)) (a – carburised, etched by nital 3 %; b – welded layer A, etched electrolytically; c – welded layer B, Adler etching; d – welded layer C, Adler etching)
Slika 3: Značilne mikrostrukture ob površinskih eksperimentalnih varovalnih plasti (pov. 200-kratna) (a – cementirana plast, jedkano z nitalom, b – navarjena plast A, elektrolitsko jedkano; c – navarjena plast B, jedkanje Adler, d – navarjena plast C, jedkanje Adler

The microstructure of the carburised layers consisted of martensite, bainite and residual austenite. The microstructure of the welded layer A was similar, with dendrites in the direction of the heat flow. In the cobalt matrix of the welded layer B microstructure tungsten and chromium carbide particles were observed. Tungsten carbide particles were also present in the martensitic matrix of the welded layer C.

From each type of protective layer six knives for the extraction cage were machined with geometrical and dimensional characteristics defined in the technical documentation of the worm-press for final extraction. Three knives were built into the working fields III and IV, along with the carburised knives owned by the oil producers. These working fields were selected because

Table 3: Average loss of weight for the knives in the working fields III and IV of the worm-press for final extraction
Tabela 3: Povprečna izguba mase v delovnih poljih III in IV vijačnih stiskalnic za končno ekstrakcijo

Working field	Average loss of knives mass, m_k/%			
	Protective layer			
	Carburized	Welded layer A	Welded layer B	Welded layer C
III	16.41	14.83	6.53	9.38
IV	18.58	17.90	8.75	12.11

previous examinations showed that they were the zones with the greatest wear.

The knives were removed from the press when the monitoring of the level of the fine particles of meal in the extracted oil required a periodic overhaul. The mass of the knives was controlled within 0.01 g, as before the installation. The measured loss of weight for the knives along the working fields, after processing about 40,00 t of partly decorticated sunflower, are given in **Table 3**.

5 DISCUSSION AND CONCLUSION

An experimental examination of the knives in the extraction cage showed that the knives with Cr and W carbide particles in the cobalt matrix (welded layer B) provide the highest wear resistance. The wear resistance of the knives with W carbide particles in the martensite matrix (welded layer C) is smaller, although for surface layers consisting of martensite (welded layer A) it was only slightly greater than for the carburised layers. These results have to be related to the determined dominant wear mechanism of the parts of the press. As hard "abrasive" ($SiO_2 \cdot nH_2O$), is found mostly in the sunflower hulls, its hardness is from HV 1000 to 1100, carbides with higher hardness (Cr and W carbides) provide the best wear resistance [10].

The complete examination of different protective layers applied to the parts of presses in oil mills was used to estimate the production costs of the parts as compared to the recorded quantities of the processed raw materials until the breakdown or replacement of the worn parts.

Possible savings by manufacturing and using worm-press parts with more wear-resistant protective layers can result in a decrease of the indirect tribological losses. The parts breakdown dimensional criterion also affects the selection of the protective layer type through a so-called "wear reserve", which should be higher than the maximum designed wear. For this reason, the constituents of the microstructure responsible for wear resistance (carbides or carbonitrides) should be harder than the abrasive contained in the oil seeds and as regularly distributed as possible in the matrix, which is as tough as possible, to prevent them from falling out in the dynamic stressing and wear in the worm-presses during oil extraction.

The mentioned possible savings are particularly large for the full operation of the oil mill. From the economic viewpoint for business efficiency this means:

- approximately 280 working days per year, including a month for overhaul and a month for collective holidays,
- operation of all the plants with a declared or roughly equivalent capacity: hulling, preparation, pressing, extraction and refinement without unplanned outages.

In conditions of processing of sunflower for commercial purposes during the receiving, warehousing and drying of the unavoidably mixed hybrids, the oil mills that also deal with subcontracting sowing areas for their own needs should pay attention to other parameters and not only to the oiliness of the "contracted" sunflower hybrids, as confirmed by the results of investigations conducted into hybrids selected in climatic conditions similar to those in Slavonia and Baranja [11,12]. From the tribological point of view, the technical and techno-logical characteristics of the seeds can contribute to a change of the pressing plant's installed capacity utilization level and to direct and much higher indirect costs (losses due to breakdowns). Some improvements might be achieved with a multidisciplinary approach to the tribo-system of worm-presses. Such an approach requires an interconnection of the whole chain: selection and choice of the hybrid in terms of the corresponding (micro) regional preconditions, soil preparation for sowing, conditions of cultivation and harvest, ware-housing, preparation for pressing, percolation, refine-ment, and the quality of oil, i.e., the crushed oil seed for stock-cattle feed preparation. The contribution of scientists could be made through a meaningful and organized research activity along with the systematic acquisition and interconnection of collected data.

6 LITERATURE

[1] Mašić, Ž., Bogdan, V., Đurđev, S. Uljarstvo, 20 (**1983**), 49–44

[2] Marušić, V., Štrucelj, D., Ivandić, Ž. Povećanje učinkovitosti pro-cesa prerade sjemena suncokreta primjenom novih postupaka zaštite za smanjenje intenziteta trošenja dijelova pužnih preša, Kemija u industriji, 53 (**2004**) 9, 393–400

[3] Turkulov, J., Dimić, E. Technical-technological characteristic of domestics sunflower hybrids, Uljarstvo, 1 (**1983**), 19–24

[4] Marušić, V. Uljara kao poligon za djelovanje tribologa, Zbornik savjetovanja Tribologija u agroindustrijskom kompleksu, Osijek, 1993, 13–21

[5] Singer, M. Seifen-Ole-Fette-Wachse, 16 (**1976**) 462–463

[6] Schneider, F. H., Khoo, D. Fette-Seifen-Anstrichmittel, 9 (**1986**), 329–340

[7] Marušić, V., Krumes, D. Verschleißprüfung der Pflanzenschecken-pressen, Olaj, Szappan, Kozmetika, 3 (**1995**) jul.-sep., 113–116

[8] Buhr, N. Mechanical pressing, World Conference Proceedings Edible Fats and Oils Processing, Champaign Ilinois USA 1990, 43–48

[9] ISO 659:1998. International Standard Oilseeds-Determination of Oil Contents (Reference method)

[10] Marušić, V., Kljajin, M., Penava, A. Posibility of tribological loss reduction by applying welded layers to the working parts of worm-presses in oil Mills, Tehnički vjesnik/ Technical Gazette, 12 (**2005**) 3/4, 11–16

[11] Aždajić, V., Marušić, V., Dimić, E., Romanić, R. Tehničko-tehno-loške i mehaničke karakteristike hibrida suncokreta s oglednog polja, 47. savetovanje Proizvodnja i prerada uljarica, Zbornik radova, Herceg Novi, 2006, 105–110

[12] Marušić, V., Ivandić, Ž., Štrucelj, D. Tribološki gubici u uljari u ovisnosti o zaštiti dijelova presa od trošenja i čvrstoći sjemena nekih hibrida suncokreta, Uljarstvo, 3 (**2004**) 1–2, 25–30

SLOVENSKO DRUŠTVO ZA MATERIALE (SDM) POPULARIZIRA ŠTUDIJ IN RAZISKAVE MATERIALOV

SLOVENIAN SOCIETY FOR MATERIALS (SDM) ENCOURAGING YOUNGS FOR STUDY AND RESEARCH OF MATERIALS

Slovensko društvo za materiale (SDM) je organiziralo 3. decembra 2008 v Ljubljani **Promocijo študija in raziskav materialov**, namenjeno srednješolcem. Prireditve, ki jo je z donacijo podprla SIJ – Slovenska industrija jekla, se je udeležilo 91 dijakov.

V devetih predavanjih so bili predstavljeni študij materialov in metalurgije, ki je organiziran po novem bolonjskem programu, možnosti za vključevanje študentov materialov v raziskovalno delo, prikazan je bil pomen kovinskih materialov v vsakodnevnem inženirstvu, predstavljene so bile tudi tehnologija centrifugalnega ulivanja valjev, ki omogoča izdelavo valjev s trdo skorjo in mehkejšo sredico, možnosti elektronske mikroskopije kot pogled v nanomateriale, raziskave vzrokov poškodb na kovinskih materialih, lastnosti in uporaba mehkomagnetnih materialov, materialov za senzorje in metode njihove sinteze, predstavljen je bil tudi postopek izdelovanja polimerov iz utekočinjenega lesa in prikazana priprava ter možnost uporabe poroznih polimernih materialov.

Namen delavnice je bil informirati dijake o študiju materialov in o raziskovalnem delu na področju materialov, vzbuditi njihovo zanimanje za ta študij in jim dati osnovne informacije o vsebini in trajanju študija.

Matjaž Torkar

Slovensko društvo za materiale
Lepi pot 11, 1000 Ljubljana
Tel: 01 4701 980
Fax: 01 4701 939
E-pošta: matjaz.torkar@imt.si

Predsednik SDM, Franc Vodopivec med uvodnim nagovorom
Introduction speech of the president of SDM Franc Vodopivec

Pogled na udeležence promocije
The view on the audience